FIRST OBSERVATION OF DIJET EVENTS WITH AN ANTIPROTON TAG AT $\sqrt{s} = 1.96$ TEV USING THE DØ FORWARD PROTON DETECTOR

by

MICHAEL ALLEN STRANG

Presented to the Faculty of the Graduate School of

The University of Texas at Arlington in Partial Fulfillment

of the Requirements

for the Degree of

DOCTOR OF PHILOSOPHY

THE UNIVERSITY OF TEXAS AT ARLINGTON

August 2005

Copyright © by MICHAEL ALLEN STRANG 2005

All Rights Reserved

To my mother Raydeen and my father Larry. Thank you for giving me the encouragement and help to become who I am today.

ACKNOWLEDGEMENTS

First, I would like to thank all of the wonderful people of the DØ Collaboration at Fermilab. Without their hard work in designing, building, and running this experiment, it would have been impossible to complete this analysis. Especially, I would like to thank the people in the FPD and QCD groups and everyone else that directly assisted me in understanding the detector and analyzing the data.

I would like to thank my adviser, Andrew Brandt, for helping me on this project; for giving me the chance to work on something from construction, through commissioning to analysis; for passing on his knowledge and for patiently answering my questions.

I would also like to thank the Physics Department at the University of Texas at Arlington for providing an environment that is open to professor/student interaction and provides a well rounded program.

Finally, I would like to thank my wife, Tonya, for being supportive and understanding through all the years as I've striven to achieve the dreams of my youth.

July 8, 2005

ABSTRACT

FIRST OBSERVATION OF DIJET EVENTS WITH AN
ANTIPROTON TAG AT $\sqrt{s} = 1.96$ TEV USING
THE DØ FORWARD PROTON DETECTOR

Publication No. _____

MICHAEL ALLEN STRANG, Ph.D.
The University of Texas at Arlington, 2005

Supervising Professor: Andrew Brandt

The Forward Proton Detector (FPD) is a new sub-system of the DØ detector, a 5000 ton particle physics detector located at the Fermilab Tevatron proton-antiproton collider. The FPD was implemented for the Tevatron Run II and gives access to a wide range of diffractive scattering processes, where one or both of the beam particles remain intact. The analysis described in this thesis makes use of the dipole spectrometer of the FPD to tag outgoing antiprotons in events that have a dijet signature in the central DØ calorimeter. Properties of jets with a diffractive tag signature are compared to jets without such a signature yielding the first observation of tagged diffractive dijets at a 1.96 TeV center-of-mass energy.

TABLE OF CONTENTS

ACKNOWLEDGEMENTS iv

ABSTRACT v

LIST OF FIGURES x

LIST OF TABLES xviii

Chapter

1. INTRODUCTION 1

1.1 Note on Units 2

2. THEORETICAL OVERVIEW 4

2.1 Scattering and Kinematics 4

2.1.1 Cross Sections 6

2.2 Diffractive Processes at the Tevatron 7

2.2.1 Regge Theory and the the Pomeron 9

2.3 Standard Model 13

2.3.1 QCD 16

2.3.1.1 Jets 18

2.3.1.2 Parton Evolution 18

2.4 Hard Diffraction 20

2.4.1 Ingelman-Schlein Model 20

2.4.2 Hard Pomeron 23

2.4.3 Soft Color 24

3. THE DØ DETECTOR AT THE TEVATRON 26

3.1 Fermi National Accelerator Laboratory 26

3.1.1 Accelerator Complex 27

3.1.1.1 Proton Source 27
3.1.1.2 Booster 29
3.1.1.3 Main Injector 29
3.1.1.4 Antiproton Source 29
3.1.1.5 Tevatron 31
3.2 The DØ Detector 32
3.2.1 Coordinate System and Variables 32
3.2.2 Magnets 35
3.2.3 Silicon Microstrip Tracker 35
3.2.4 Central Fiber Tracker and Preshower Detectors 38
3.2.5 Calorimeter 40
3.2.5.1 Central Calorimeter 43
3.2.5.2 End-cap Calorimeter 44
3.2.5.3 Intercryostat Detector 45
3.2.5.4 Calorimeter Readout 46
3.2.6 Luminosity Monitor 46
3.2.7 Muon System 47
3.2.8 Trigger and Data Acquisition System 49
4. THE DØ FORWARD PROTON DETECTOR 52
4.1 Forward Proton Detector Layout 52
4.2 FPD Position Detectors 55
4.3 FPD Operations 59
5. OBJECT IDENTIFICATION 64
5.1 Jet Identification 64
5.1.1 Improved Legacy Cone Algorithm 67
5.1.2 Jet Energy Scale 70

5.2 Proton Identification 72
5.2.1 Hit Reconstruction 74
5.2.2 Proton Tracking 80
5.2.2.1 Tevatron Lattice Propagation 80
5.2.2.2 Track Reconstruction Algorithm 83
6. DATA SELECTION OF DIJET SAMPLE 87
6.1 Run Selection 87
6.2 Data Merging 88
6.3 Trigger Selection 88
6.4 Event Cuts 89
6.4.1 Vertex 90
6.4.2 Missing E_T 92
6.5 Jet Cuts 94
6.5.1 Electromagnetic Fraction 95
6.5.2 Coarse Hadronic Fraction 96
6.5.3 Hot Fraction 97
6.5.4 n90 Variable 98
6.5.5 L1 Scalar E_T 100
6.5.6 Corrected Jet Energy 101
6.5.7 Dijet Event 101
6.6 Event Summary 101
7. ANALYSIS 103
7.1 FPD Performance 103
7.2 Effect of Quality Cuts on Gaps and Tags 110
7.3 Diffractive Dijets 113
8. CONCLUSION 124

Appendix

A. CONSTRUCTION OF THE FORWARD PROTON DETECTOR 126

B. OPERATION OF THE FORWARD PROTON DETECTOR 145

REFERENCES 151

BIOGRAPHICAL STATEMENT 157

LIST OF FIGURES

Figure Page

2.1 Diagram of generic two-body scattering process 4

2.2 Generic diagram for (a) s-channel resonance and (b) t-channel exchange processes 6

2.3 Generic diagrams for (a) elastic and (b) single diffraction in proton-antiproton collision 8

2.4 Generic diagrams for (a) hard single, (b) central resonant, and (c) hard double diffraction; the colored/dashed circles represent jets of particles (or other hard objects) 9

2.5 Chew-Frautschi plot of spin $J - m^2$ of a particle showing degenerate Reggeon, pion, and Pomeron trajectories 10

2.6 Total cross section for pp and $p\overline{p}$ collisions 11

2.7 Differential cross-section in $p\overline{p}$ collisions at different energies (10^{-2} factor between successive curves omitted) 12

2.8 Schematic diagram of Ingelman-Schlein Regge factorization 21

2.9 The contribution of a gluonic ladder with n rungs to the Pomeron exchange. The reggeized gluon propagators are represented by thick, vertical gluon lines 24

2.10 Schematic diagram of Soft Color Interaction for (a) non-diffractive, (b) hard diffractive, and (c) double Pomeron topologies 24

3.1 Schematic view of the Fermilab accelerator complex 28

3.2 Schematic diagram of the central DØ Run II detector showing (a) $y - z$ slice out to the muon detectors and (b) $r - z$ slice of the tracking system 33

3.3 Schematic drawing of the SMT detector 36

3.4 Schematic view of the DØ Liquid Argon / Uranium Calorimeter 41

3.5 Schematic view of the calorimeter cell structure 42

3.6 Quadrant cross sectional view of DØ pseudo-projective towers 43

3.7 The DØ 3-level trigger scheme and typical trigger rates 50

4.1 Schematic layout of the FPD system 53

4.2 Diagram of an FPD castle 54

4.3 Schematic diagram of FPD position detectors and MAPMT 56

4.4 Picture of splicing machine used in production of FPD fibers 57

4.5 Picture of (a) cookie and (b) cartridge base used in the FPD detector 58

4.6 Picture of (a) MAPMT and (b) cartridge top used in the FPD detector 58

4.7 Picture of fully installed dipole spectrometer. The detector cartridges are the cylindrical structures (indicated by arrows) and the blue racks above them house the pot motion electronics and amplifiers 60

5.1 Schematic illustration of different levels of a jet 65

5.2 Illustration of infrared sensitivity of cone algorithm with: (a) two jets in final state with well separated partons, (b) one jet in final state if additional soft gluon emitted between partons with transverse energy above threshold 70

5.3 JES corrections for $R = 0.7$ jets for (a) central jets as a function of E_{uncorr} and (b) associated errors, (c) 50 GeV jets as a function of η and (d) associated errors 73

5.4 Examples of two types of FPD segments: (a) single fiber, (b) two fiber 75

5.5 Example of a segment combination giving an FPD hit. The two coordinate systems used are also displayed 76

5.6 Hit resolution of an FPD detector by comparing x_d-coordinate from u- and v-segments to x_d-coordinate from x-segment (from data) 77

5.7 Hit comparison between detectors in the dipole spectrometer with (a) schematic layout of the detectors showing particle trajectories, (b) comparison of x_d between detectors, (c) comparison of y_d between detectors showing different trajectories for diffracted $\overline{p}$ and halo particles 78

5.8 FPD reconstruction resolutions determined from MC for (a) ξ and (b) t for the dipole detector 86

5.9 Geometric acceptance of the dipole spectrometer with flat t dependence and detectors at $8\sigma_x$ positions 86

6.1 Schematic illustration of data merging 88

6.2 Distributions of number of tracks associated with primary vertex in bins of η and p_T of the leading jet. From left to right, the columns correspond to central ($|\eta| < 0.8$), intermediate ($0.8 < |\eta| < 1.5$), and forward ($|\eta| > 1.5$). From top to bottom, the rows correspond to low-p_T ($20 < p_T < 100$ GeV), medium-p_T ($100 < p_T < 180$ GeV), and high-p_T ($p_T > 180$ GeV) 90

6.3 Distributions of number of tracks associated with primary vertex split out by trigger 91

6.4 Distributions of z position of primary vertex in bins of η and p_T of the leading jet for events that pass the N_{trk} cut. From left to right, the columns correspond to central ($|\eta| < 0.8$), intermediate ($0.8 < |\eta| < 1.5$), and forward ($|\eta| > 1.5$). From top to bottom, the rows correspond to low-p_T ($20 < p_T < 100$ GeV), medium-p_T ($100 < p_T < 180$ GeV), and high-p_T ($p_T > 180$ GeV) 92

6.5 Distributions of METC / $p_T^{leading}$ in bins of η and p_T of the leading jet. From left to right, the columns correspond to central ($|\eta| < 0.8$), intermediate ($0.8 < |\eta| < 1.5$), and forward ($|\eta| > 1.5$). From top to bottom, the rows correspond to low-p_T ($20 < p_T < 100$ GeV), medium-p_T ($100 < p_T < 180$ GeV), and high-p_T ($p_T > 180$ GeV) 93

6.6 Distributions of METC / $p_T^{leading}$ split out by trigger 94

6.7 Distributions of EMF in bins of η and p_T. The solid black line is the leading jet distribution and the dashed blue line is the second jet distribution. All distributions are normalized to unit area. From left to right, the columns correspond to central ($|\eta| < 0.8$), intermediate ($0.8 < |\eta| < 1.5$), and forward ($|\eta| > 1.5$). From top to bottom, the rows correspond to low-p_T ($20 < p_T < 100$ GeV), medium-p_T ($100 < p_T < 180$ GeV), and high-p_T ($p_T > 180$ GeV) 95

6.8 Distributions of CHF with a logarithmic scale in bins of η and p_T. The solid black line is the leading jet distribution and the dashed blue line is the second jet distribution. All distributions are normalized to unit area. From left to right, the columns correspond to central ($|\eta| < 0.8$), intermediate ($0.8 < |\eta| < 1.5$), and forward ($|\eta| > 1.5$). From top to bottom, the rows correspond to low-p_T ($20 < p_T < 100$ GeV), medium-p_T ($100 < p_T < 180$ GeV), and high-p_T ($p_T > 180$ GeV) 97

6.9 Distributions of HotF with a logarithmic scale in bins of η and p_T. The solid black line is the leading jet distribution and the dashed blue line is the second jet distribution. All distributions are normalized to unit area. From left to right, the columns correspond to central ($|\eta| < 0.8$), intermediate ($0.8 < |\eta| < 1.5$), and forward ($|\eta| > 1.5$). From top to bottom, the rows correspond to low-p_T ($20 < p_T < 100$ GeV), medium-p_T ($100 < p_T < 180$ GeV), and high-p_T ($p_T > 180$ GeV) 98

6.10 Distributions of n90 in bins of η and p_T. The solid black line is the leading jet distribution and the dashed blue line is the second jet distribution. All distributions are normalized to unit area. From left to right, the columns correspond to central ($|\eta| < 0.8$), intermediate ($0.8 < |\eta| < 1.5$), and forward ($|\eta| > 1.5$). From top to bottom, the rows correspond to low-p_T ($20 < p_T < 100$ GeV), medium-p_T ($100 < p_T < 180$ GeV), and high-p_T ($p_T > 180$ GeV) 99

6.11 Distributions of L1SET / p_T(1-CHF) in bins of η and p_T. The solid black line is the leading jet distribution and the dashed blue line is the second jet distribution. All distributions are normalized to unit area. From left to right, the columns correspond to central ($|\eta| < 0.8$), intermediate ($0.8 < |\eta| < 1.5$), and forward ($|\eta| > 1.5$). From top to bottom, the rows correspond to low-p_T ($20 < p_T < 100$ GeV), medium-p_T ($100 < p_T < 180$ GeV), and high-p_T ($p_T > 180$ GeV) 100

7.1 ADC distributions of representative fibers normalized to unit area. The left column corresponds to D1I and the right to D2I. The black solid line corresponds to the raw ADC distribution, the blue dashed line corresponds to the distribution of events with a prototrack 104

7.2 Fiber correlations between layers as a function of plane for the dipole spectrometer. The left column corresponds to D1I and the right to D2I. The top row shows the u plane, the middle corresponds to the x plane, and the bottom to the v plane 105

7.3 Fiber occupancies for each layer in the dipole spectrometer normalized to unit area. The left column corresponds to D1I and the right to D2I. From top to bottom, the rows correspond to the u, u', x, x', v, and v' layers respectively. The solid lines correspond to all events (including halo) while the blue dashed lines correspond to events with a prototrack 106

7.4 Hit resolution for each detector of the dipole spectrometer with mapping correction applied overlaid with the Gaussian fit. The left column corresponds to D1I and the right to D2I 107

7.5 Hit maps for each detector of the dipole spectrometer. The left column corresponds to D1I and the right to D2I. The top row corresponds to events with one validated hit in each detector in the same event, the middle row corresponds to events with a validated hits in the detector, independent of the state of the other detector, and the bottom row corresponds to all hits as determined by any two segments 108

7.6 Hit correlation between detectors in the dipole spectrometer for different triggers: (a) JT_25TT_NG, (b) JT_25TT_GapS, (c) JT_25TT_GapN, and (d) JT_45TT 109

7.7 N_{trk} distribution for non-diffractive, gap and tag samples normalized to unit area. Plot (a) corresponds to trigger JT_25TT_NG, (b) to JT_25TT_GapN, (c) to JT_25TT_GapSN, and (d) JT_45TT. The black histogram corresponds to events with no gaps or tags, the blue dashed histogram corresponds to a GapN or a GapSN with or without a tag, and the red dotted histogram corresponds to tags (with or without a gap in the case of (a) and (d)) 111

7.8 $METC/p_T^{leading}$ distribution for non-diffractive, gap and tag samples normalized to unit area. Plot (a) corresponds to trigger JT_25TT_NG, (b) to JT_25TT_GapN, (c) to JT_25TT_GapSN, and (d) JT_45TT. The black histogram corresponds to events with no gaps or tags, the blue dashed histogram corresponds to a GapN or a GapSN with or without a tag, and the red dotted histogram corresponds to tags (with or without a gap in the case of (a) and (d)) 112

7.9 Number of jets for non-diffractive, gap and tag samples normalized to unit area. Plot (a) corresponds to trigger JT_25TT_NG, (b) to JT_25TT_GapN, (c) to JT_25TT_GapSN, and (d) JT_45TT. The black histogram corresponds to events with no gaps or tags, the blue dashed histogram corresponds to a GapN or a GapSN with or without a tag, and the red dotted histogram corresponds to tags (with or without a gap in the case of (a) and (d)) 113

7.10 η distribution for non-diffractive, gap and tag samples normalized to unit area. Plot (a) corresponds to trigger JT_25TT_NG, (b) to JT_25TT_GapN, (c) to JT_25TT_GapSN, and (d) JT_45TT. The black histogram corresponds to events with no gaps or tags, the blue dashed histogram corresponds to a GapN or a GapSN with or without a tag, and the red dotted histogram corresponds to tags (with or without a gap in the case of (a) and (d)) 114

7.11 η distribution of leading and second jets 115

7.12 ϕ distribution for non-diffractive, gap and tag samples normalized to unit area. Plot (a) corresponds to trigger JT_25TT_NG, (b) to JT_25TT_GapN, (c) to JT_25TT_GapSN, and (d) JT_45TT. The black histogram corresponds to events with no gaps or tags, the blue dashed histogram corresponds to a GapN or a GapSN with or without a tag, and the red dotted histogram corresponds to tags (with or without a gap in the case of (a) and (d)). Errors are statistical only 116

7.13 $\Delta\phi$ distribution for non-diffractive, gap and tag samples normalized to unit area. Plot (a) corresponds to trigger JT_25TT_NG, (b) to JT_25TT_GapN, (c) to JT_25TT_GapSN, and (d) JT_45TT. The black histogram corresponds to events with no gaps or tags, the blue dashed histogram corresponds to a GapN or a GapSN with or without a tag, and the red dotted histogram corresponds to tags (with or without a gap in the case of (a) and (d)) 117

7.14 Ratio of $\Delta\phi$ distributions for non-diffractive, gap and tag samples. Plot (a) corresponds to trigger JT_25TT_NG, (b) to JT_25TT_GapN, (c) to JT_25TT_GapSN, and (d) JT_45TT. The blue points correspond to the ratio of gap to non-gap samples for (a) and (d), the red points correspond to the ratio of tags to non-gap for (a) and (d), and the ratio of tags to gaps for (b) and (c). Errors are statistical only 118

7.15 p_T spectrum for non-diffractive, gap and tag samples normalized to unit area. Plot (a) corresponds to trigger JT_25TT_NG, (b) to JT_25TT_GapN, (c) to JT_25TT_GapSN, and (d) JT_45TT. The black histogram corresponds to events with no gaps or tags, the blue dashed histogram corresponds to a GapN or a GapSN with or without a tag, and the red dotted histogram corresponds to tags (with or without a gap in the case of (a) and (d)) 119

7.16 Ratio of p_T spectrum for non-diffractive, gap and tag samples in the region of reasonable statistics. Plot (a) corresponds to trigger JT_25TT_NG, (b) to JT_25TT_GapN, (c) to JT_25TT_GapSN, and (d) JT_45TT. The blue points correspond to the ratio of gap to non-gap sample for triggers (a) and (d), the red points correspond to the ratio of tags to non-gap samples for (a) and (d), and the ratio of tags to gaps for (b) and (c). Errors are statistical only 120

7.17 Jet width distribution for non-diffractive, gap and tag samples normalized to unit area. Plot (a) corresponds to trigger JT_25TT_NG, (b) to JT_25TT_GapN, (c) to JT_25TT_GapSN, and (d) JT_45TT. The black histogram corresponds to events with no gaps or tags, the blue dashed histogram corresponds to a GapN or a GapSN with or without a tag, and the red dotted histogram corresponds to tags (with or without a gap in the case of (a) and (d)) 121

7.18 Distribution of (a) ξ and (b) t for the tag sample 122

7.19 ξ vs. t for tag sample 123

LIST OF TABLES

Table Page

2.1 Summary of matter particles (fermions) in the Standard Model 14

2.2 Summary of forces and gauge vector bosons 15

3.1 Summary of SMT sub-detector and sensors 37

6.1 Summary of triggers used in analysis 89

6.2 Summary of number of events after quality cuts 102

7.1 Summary of number of gaps and tags after quality cuts 110

CHAPTER 1

INTRODUCTION

The drive to understand the nature of the universe has led to the establishment of the Standard Model in an attempt to describe the matter and forces around us. Through the use of accelerator experiments, it has become possible to probe the smallest particles of matter in the continuing quest to complete our understanding.

Of particular interest in this dissertation is the study of the strong force, the force that holds quarks and gluons within the hadron as well as holding hadrons together in a nucleus (described by Quantum ChromoDynamics or QCD [1]). A particular class of strong interactions are the diffractive interactions in which two hadrons interact with each other, yet instead of breaking up as in a typical hard scattering interaction, one or both particles survive intact.

These processes are studied through scattering interactions, providing a set of kinematic variables that make it possible to theoretically predict cross-sections for these types of events that can then be compared against experimental observations.

Regge Theory [2] (a theory to explain forward scattering in strong interactions) predates QCD and provides a fairly accurate model for so-called soft diffractive events. Since the strong force is currently described by QCD, it is necessary to also find a way to explain these types of events within the QCD framework as they are a result of strong interactions.

Studies of this kind require massive detectors and energetic accelerators to achieve the energies necessary to probe the partonic structure of the proton. These complex

detectors capture and measure the passage of particles resulting from collisions. In the past, a mix of hard interactions with regions of the detector devoid of activity (rapidity gap) were used to probe diffractive events (*e.g.* see [3]).

Additional ways of making these measurements involve measuring the proton or antiproton that survives a hard collision intact (tag). This required the construction, installation, commissioning, and operation of an entirely new detector subsystem at DØ (the Forward Proton Detector or FPD), that provides access to the full kinematics of the event and provides better measurements of the diffractive processes.

The majority of the effort leading to this dissertation has been involved in these aspects of the FPD as well as in the developing of algorithms for analyzing the data and establishing the operations of the detector.

Through making such measurements of diffractive events, it will become possible to understand the areas of QCD that are not currently well understood by the theory, allowing us to better understand the strong force.

In this dissertation, a first analysis is performed to show that the dipole spectrometer of the Forward Proton System is working and that it will be possible to make such measurements in the future. A preliminary analysis of dijet events, with and without tags as well as with or without gaps is presented as verification that the dipole spectrometer is working as designed and is ready to be used in further diffractive analyses.

1.1 Note on Units

The basic unit used in high-energy particle physics to express energy, momentum and mass is the electron volt (eV), where one electron volt is equal to the energy gained by one electron crossing a potential of one volt (*i.e.* 1.602×10^{-19} J). Instead of expressing energy as eV, momentum as eV/c and mass as eV/c^2, all are expressed simply in terms of eV through the use of natural units (rationalized Heaviside-Lorentz system see [4] for

more details). This means that the speed of light in the vacuum, c, and the reduced Planck's constant, $\hbar$, are expressed as unity ($c = \hbar = 1$).

CHAPTER 2

THEORETICAL OVERVIEW

The search for a fundamental explanation of matter and forces has been long and varied. Towards the end of the 20th Century, the current understanding was combined in a compact form known as the Standard Model (SM). While providing a good explanation for many processes, there are still some areas that are poorly understood. Among these is the subset on which this dissertation will focus: diffractive physics in the studies of the strong force. In this chapter, the underlying theory is presented roughly as it was developed.

2.1 Scattering and Kinematics

Interactions can often be represented by two-body ($1 + 2 \rightarrow 3 + 4$) scattering amplitudes as shown in Fig. 2.1. In such an interaction, particle 1 interacts with particle 2 resulting in states 3 and 4 (either new p articles or the same particles with new four-vectors).

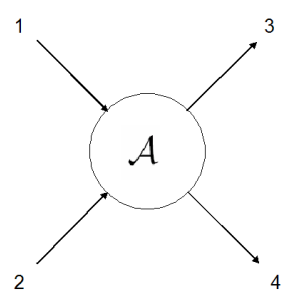

Figure 2.1 Diagram of generic two-body scattering process.

A useful set of Lorentz-invariant variables used in calculations are the Mandelstam variables s, t, and u [5]. The first of these variables is defined in terms of the four-momenta P_1^μ and P_2^μ of the two incoming particles:

$$s = (P_1^\mu + P_2^\mu)^2 = E_{cm}^2, \tag{2.1}$$

and is equal to the square of the center-of-mass energy (E_{cm}) of the interaction. The second variable is the negative square of the four-momentum transfer (Q),

$$t = (P_1^\mu - P_3^\mu)^2 = -Q^2, \tag{2.2}$$

where P_3^μ is the four-momentum of particle 3. The third variable is defined as:

$$u = (P_1^\mu - P_4^\mu)^2. \tag{2.3}$$

Two of these three variables is sufficient to define the kinematics of the interaction due to the relationship,

$$s + t + u = \sum_{i=1}^{4} m_i^2, \tag{2.4}$$

where m_i is the mass of the ith particle.

An s-channel process is one in which particles 1 and 2 annihilate each other to produce a resonance which then decays into the final state particles 3 and 4 as shown in Fig. 2.2(a). A t-channel process is one where a mediator is exchanged between particles 1 and 2 resulting in particles 3 and 4 in the final state (see Fig. 2.2(b)).

To calculate a scattering amplitude, all possible diagrams that can contribute to the interaction must be considered. Once the amplitude $\mathcal{A}(s,t)$ is calculated for the

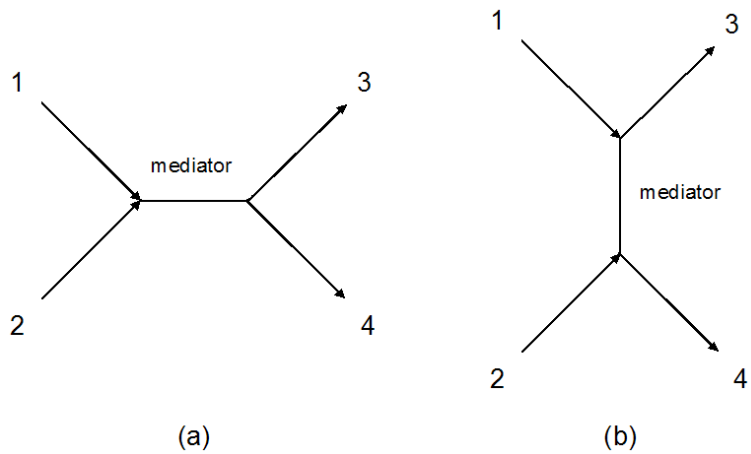

Figure 2.2 Generic diagram for (a) s-channel resonance and (b) t-channel exchange processes.

s-channel $(1+2 \rightarrow 3+4)$ process, the amplitude for the corresponding t-channel process can be obtained via "crossing" symmetries[1] (interchanging s and t in the expression).

2.1.1 Cross Sections

The cross-section of an interaction is related to the probability of that interaction occurring and can typically be measured experimentally as well as predicted theoretically. The *optical theorem* provides a relationship between the total cross-section of a process and the imaginary part of the forward $(t = 0)$ scattering amplitude:

$$\sigma_{tot} = \frac{4\pi}{s} \Im\mathrm{m}\mathcal{A}(s, 0), \tag{2.5}$$

The rise of the total cross-section with increasing s, however, is limited to be less than the limit given by the Froissart-Martin bound [6, 7]:

$$\sigma_{tot} < \frac{\pi}{m_\pi^2} (\ln s)^2 (s \rightarrow \infty), \tag{2.6}$$

[1] An incoming particle with momentum p in a diagram is the same as the associated outgoing anti-particle with momentum $-p$.

where m_π is the mass of the pion. This limit is necessary because otherwise individual probabilities would not sum to unity (Unitarity condition). The differential cross-section ($d\sigma/dt$) is expressed in terms of the full scattering amplitude as:

$$\frac{d\sigma}{dt} = \frac{\pi}{s^2}|\mathcal{A}(s,t)|^2. \tag{2.7}$$

2.2 Diffractive Processes at the Tevatron

Diffractive processes contribute around 40% of the total cross-section as observed at the Tevatron [8]. Therefore, it is necessary to understand these types of processes to have a complete theory. Much of the information on diffraction in this chapter is drawn from references [9, 10, 11, 12].

The largest component of diffraction (component with the largest cross-sections) is *soft diffraction*. Of this class of events, elastic scattering is predominant (see Fig. 2.3(a)). For such an event:

$$p + \overline{p} \rightarrow p + \overline{p}, \tag{2.8}$$

some momentum is transferred from one beam particle to the other through a mediator that carries the quantum numbers of the vacuum (*i.e.* no charge, isospin, baryon number or color) often called the Pomeron ($I\!P$). Both initial particles survive intact, and the hadrons act like solid composite objects (exhibit no internal structure). There are no further particles produced in such an interaction. There is a region devoid of particle production (*rapidity gap*) between the scattered proton and antiproton (see Section 3.2.1 for descriptions of the applicable variables η and ϕ). In addition to elastic scattering, there is also single diffraction,

$$p + \overline{p} \rightarrow (p \text{ or } \overline{p}) + X, \tag{2.9}$$

where either the p or $\overline{p}$ is excited and produces a system X on one side of the interaction (see Fig. 2.3(b)). There is a rapidity gap in the region of the intact scattered hadron.

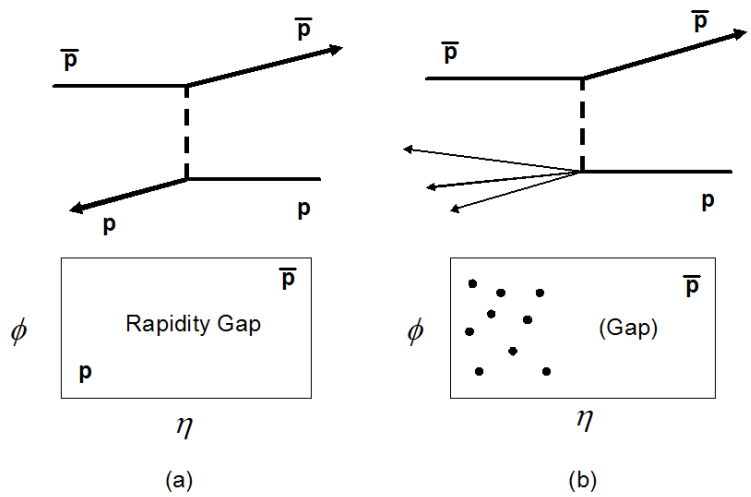

Figure 2.3 Generic diagrams for (a) elastic and (b) single diffraction in proton-antiproton collision.

In addition to soft diffraction, there is *hard diffraction*. In such an event, the particle that breaks up can leave high energy or high mass particles in the central detector (*e.g.* jets, W/Z bosons, heavy quarks). This dissertation studies events with the single diffractive dijet production process,

$$p + \overline{p} \rightarrow \overline{p} + jj, \tag{2.10}$$

as shown in Fig. 2.4(a). Additional types of diffraction include central resonant (double Pomeron) production where both the p and $\overline{p}$ survive intact,

$$p + \overline{p} \rightarrow p + jj + \overline{p}, \tag{2.11}$$

as shown in Fig. 2.4(b) and double diffraction (color singlet exchange) where they both dissociate but leave a gap between them,

$$p + \overline{p} \rightarrow jj + \text{gap} + X, \tag{2.12}$$

as shown in Fig. 2.4(c).

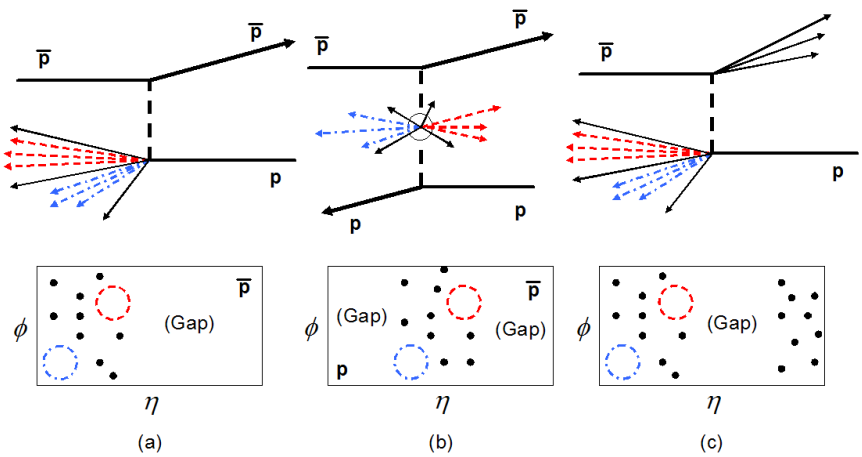

Figure 2.4 Generic diagrams for (a) hard single, (b) central resonant, and (c) hard double diffraction; the colored/dashed circles represent jets of particles (or other hard objects).

2.2.1 Regge Theory and the the Pomeron

Soft diffraction is well explained by a theory predating QCD known as Regge Theory (see reference [2] for a good overview). Regge theory interprets strong interactions as proceeding via the exchange of particles falling along trajectories, $\alpha(t)$, where $\alpha(t)$ is a complex function of angular momentum. Particles are organized in sequences with

increasing mass (m_i) and spin (J_i) represented by resonances in the amplitude of the exchange in the t-channel which is proportional to,

$$\frac{1}{l - \alpha(t)}, \tag{2.13}$$

where l is the angular momentum. Places where $l = \Re e\alpha(t)$ form Regge poles corresponding to the exchange of particles where $\alpha(m_i) = J_i$. These resonances can be plotted on a projection from the complex angular momentum space onto the $J - m^2$ plane (Chew-Frautschi [13] plot shown in Fig. 2.5) showing that the trajectories appear to have a linear representation $\alpha(t) = \alpha(0) + \alpha^{'}t$ where $\alpha(0)$ is the intercept and $\alpha^{'}$ is the slope of the trajectory. For example, the pion has a trajectory in this scheme of $\alpha_\pi(t) \cong 0.9t$ and a generic Reggeon has the trajectory $\alpha_R(t) \cong 0.5 + t$.

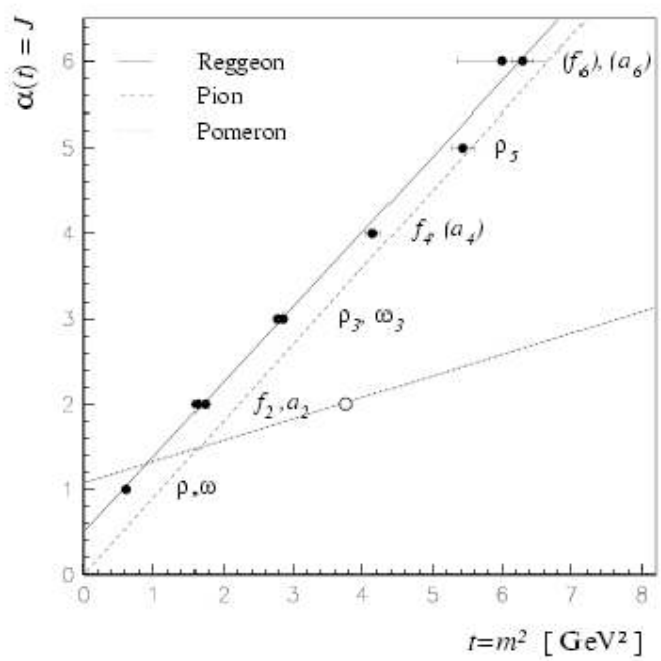

Figure 2.5 Chew-Frautschi plot of spin $J - m^2$ of a particle showing degenerate Reggeon, Pion, and Pomeron trajectories [14].

The theory predicts that in the limit $s \gg t$ the scattering amplitude for the exchange of a single trajectory has the form $\mathcal{A} \sim s^{\alpha(0)}$ such that the total cross-sections consist of terms of the form,

$$\sigma_{tot} \propto s^{\alpha(0)-1}. \tag{2.14}$$

Figure 2.6 shows the total cross-section (σ) for elastic pp and $p\overline{p}$ collisions as a function of center-of-mass energy $\sqrt{s}$. It is clear that a trajectory with an intercept $\alpha(0) \gtrsim 1$ is necessary to account for a rise in the cross-section with increasing s. This trajectory was named after I.Y. Pomeranchuk – who explained the quantum numbers that the trajectory would have to have [15] (as exhibited in the two cross-sections reaching the same values as $s \to \infty$).

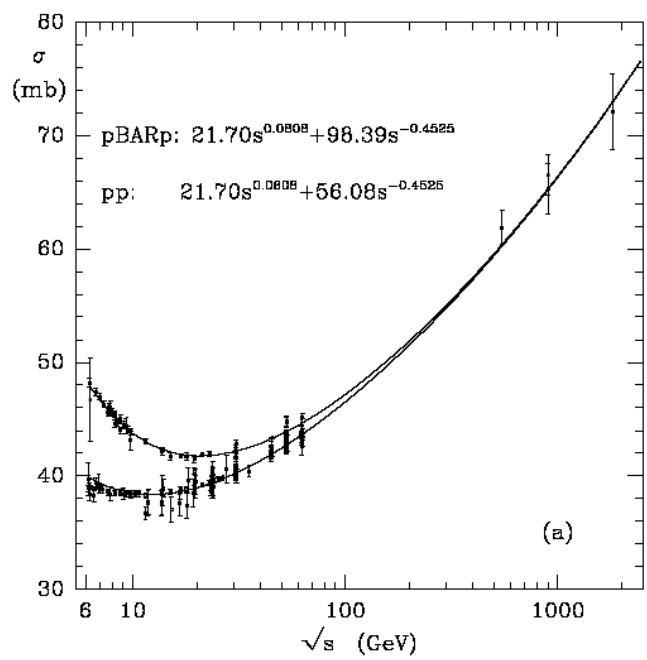

Figure 2.6 Total cross section for pp and $p\overline{p}$ collisions [16].

Donnachie and Landshoff parameterized these total cross-sections as being made up of two contributions,

$$\sigma_{tot} = X s^{\alpha(0)_{I\!P}-1} + Y s^{\alpha(0)_R-1}. \tag{2.15}$$

In a fit to these two cross-sections, the first term (parameterizing the rise of the cross-section) was the same for both pp and $p\overline{p}$. The fitted intercept of this trajectory was found to be $\alpha_{I\!P} = 1.08$ [16]. The second term is a so-called Reggeon contribution and describes the fall of the cross-section. The slope of the "Pomeron" trajectory was determined by fitting the differential cross-section $d\sigma/dt$ in different energy intervals (as shown in Fig. 2.7) to be $\alpha'_{I\!P} = 0.25$ GeV^{-2} [17]. The resulting trajectory $\alpha_{I\!P}(t) = 1.08 + 0.25t$ is referred to as the "soft" Pomeron trajectory and can phenomenologically describe a large number of soft diffractive physics processes.

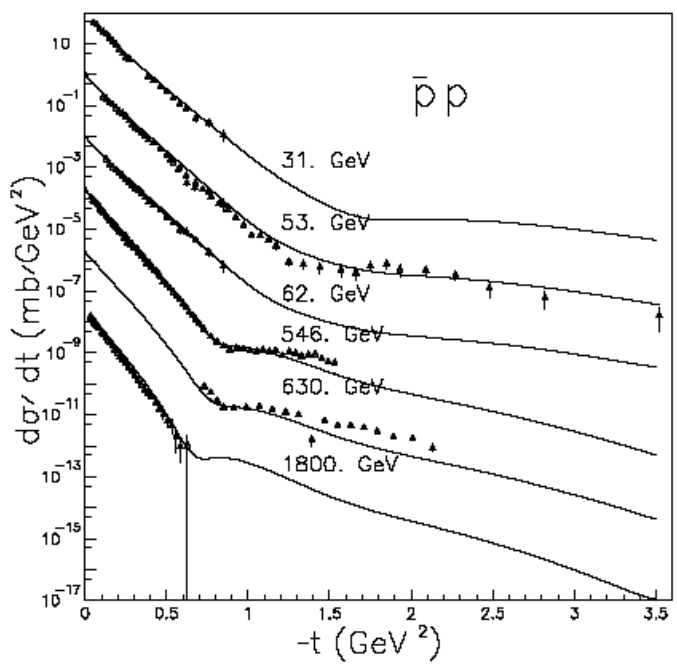

Figure 2.7 Differential cross-section in $p\overline{p}$ collisions at different energies (10^{-2} factor between successive curves omitted) [18].

Note that the slow rise of the total cross-sections would ultimately violate Unitarity at energies approaching the Planck scale. The rise, however, could be reduced at larger $\sqrt{s}$ (*e.g.* through multiple Pomeron exchange) since as more Pomerons are exchanged in the interaction, they are expected to contribute with alternating signs and growing amplitude, thus restoring Unitarity. At $\sqrt{s} = 1.8$ TeV, such multiple exchanges contribute about 10% to the total cross-section [19].

The form of the differential cross-section at small-t, as shown in Fig. 2.7, helps motivate the use of the term diffraction to describe this class of interactions. The exponential behavior at small-t,

$$\frac{d\sigma/dt}{(d\sigma/dt)_{t=0}} = e^{-bt} \cong 1 - b(p\theta)^2, \tag{2.16}$$

where p is the incoming momentum, can be interpreted in analogy to light diffractively scattering from a small disk,

$$\frac{I}{I_0} = \frac{[2J_1(x)]^2}{x} \cong 1 - r^2(k\theta)^2, \tag{2.17}$$

where I is the intensity, $J_1(x)$ is a Bessel function of the first king, k is the wave-number of the photons, r is the radius of the disk and $x = kr\sin\theta \cong kr\theta$. From this comparison, the radius of interaction is related to the slope of the cross-section $b = r^2/4$ and therefore reflects the size of the scattered object. As a function of $\sqrt{s}$ and t, the slope varies from a value of $b \approx 17$ GeV^{-2} at $\sqrt{s} = 1.8$ TeV for elastic interactions [20, 21] to a value of $b \approx 7$ GeV^{-2} for single diffraction.

2.3 Standard Model

The Standard Model provides a description of the fundamental building-blocks of nature as it is currently understood (see References [22, 23, 24] for a detailed treatment).

In the theory, the fundamental particles of matter are represented by *fermions*[2]. Table 2.1 shows these particles, along with some of their properties (every particle also has an associated anti-particle which is not shown).

Table 2.1 Summary of matter particles (fermions) in the Standard Model

Leptons					
		mass	**charge**		
generation	**flavor**	**(GeV)**	**electric**[a]	**weak**[b]	**color**[b]
1	ν_e (e neutrino)	$< 3 \times 10^{-9}$	0	yes	no
	e (electron)	0.000511	-1	yes	no
2	ν_μ (μ neutrino)	< 0.0002	0	yes	no
	μ (muon)	0.106	-1	yes	no
3	ν_τ (τ neutrino)	< 0.018	0	yes	no
	τ (tau)	1.777	-1	yes	no
Quarks					
1	u (up)	$0.002 - 0.004$	$2/3$	yes	yes
	d (down)	$0.004 - 0.008$	$-1/3$	yes	yes
2	c (charm)	$1.15 - 1.35$	$2/3$	yes	yes
	s (strange)	$0.08 - 0.13$	$-1/3$	yes	yes
3	t (top)	174	$2/3$	yes	yes
	b (bottom)	$4.1 - 4.4$	$-1/3$	yes	yes

[a] Charge is expressed as a fraction of proton charge.

[b] Yes indicates particles can participate in that type of force interaction. No indicates it does not.

While the leptons can be directly observed, because of the nature of quarks (see Section 2.3.1) they always combine into *Hadrons*. Hadrons are classified as *mesons* or *baryons*. Mesons consist of a quark/anti-quark pair (*e.g.* the pion). Because they contain quark/anti-quark pairs, mesons are *bosons*[3]. Baryons, on the other hand, are fermions that consist of three quarks. Examples of baryons are the nucleons (the proton and the neutron).

[2]Spin 1/2 particles represented by *leptons* (l) and *quarks* (q) that obey the Pauli exclusion principle.

[3]Integral spin particles that do not obey the exclusion principle.

Atoms are composed of nucleons and leptons. Interestingly, all of the regularly existing matter is made up only of the fundamental particles in the first generation. The other particles are extremely short-lived and require accelerators or cosmic ray detectors to study them.

The Standard Model includes three of the fundamental forces: electromagnetism, weak force and strong force. Gravity is currently not included in the SM. Each force is mediated by a gauge vector boson, emitted (or absorbed) by a particle carrying the appropriate charge. The forces and bosons are summarized in Table 2.2.

Table 2.2 Summary of forces and gauge vector bosons

force	**mediator**	**mass (GeV)**	**spin**	**electric charge**	**range (m)**	**strength**
strong	gluon (g)	0	1	0	10^{-15}	0.1[a]
electromagnetic	photon (γ)	0	1	0	infinite	1/137
weak	$W^{\pm}$	80.4	1	± 1	10^{-18}	10^{-6}
	Z^0	91.2	1	0	10^{-18}	10^{-6}
gravity[b]	graviton (G)	0	2	0	infinite	6×10^{-39}
	Higgs[c](H°)	> 114	0	0		

[a] The strength drops to zero as particles get closer together (asymptotic freedom). The value given here is for the energy scale near the mass of the Z^0 boson.

[b] The graviton is currently unobserved and the force is not expressed as a quantum field theory. It is included since gravity is a fundamental force.

[c] The Higgs boson is not a mediator but rather a consequence of the Higgs mechanism. It is currently unobserved but necessary to explain the spontaneous symmetry breaking that allows electroweak unification as well as providing a mechanism by which all other particles attain mass. The coupling constant of this field varies with the mass of the particle with which it interacts.

The full theory is expressed as quantum field gauge theories for each of the forces. The elementary particles are represented as spinors. Requiring the Lagrangian of the quantum fields be invariant under gauge transformations of several symmetry groups leads to a description of the particles and their interactions. In total, the standard model

is invariant for the $\mathrm{SU}(3) \times \mathrm{SU}(2)_L \times \mathrm{U}(1)$ groups. In addition, various quantum number are required to be conserved across interactions (*e.g.* lepton and baryon number).

The first quantum field theory was *quantum electrodynamics* (QED). It remodeled the electromagnetic force as an exchange force arising from the exchange of *virtual*[4] photons expressed as a U(1) gauge theory conserving charge and spin. As the first quantum field theory, it has been used as the basis for all following theories in terms of the tools used to express them (*e.g.* renormalization). It accounts for all electromagnetic phenomena, including those with no classical component and has been extremely predictive.

QED was merged with the weak field to form the *electroweak* theory. This combined theory is an $\mathrm{SU}(2)_L \times \mathrm{U}(1)$ gauge theory conserving weak isospin (I) and weak hypercharge (Y). It accounts for nuclear decay phenomena and is the only way that neutrinos interact. It is modeled as an exchange force of three massive virtual bosons $W^{\pm}$ ("charge current") and Z^0 ("neutral current") between particles with weak charge, as well as photons for particles with electric charge. The *Higgs mechanism* has been proposed as a method through which, at sufficient energy, there is a spontaneous symmetry breaking allowing these three bosons to take on mass while the photon remains massless. The same mechanism can also be used to provide masses for the other particles in the Standard Model through coupling with the Higgs field mediated by the Higgs boson. This boson is yet to be observed, but the Higgs search is a very active area of study.

2.3.1 QCD

Quantum ChromoDynamics (QCD) is the SU(3) gauge theory used to explain strong force interaction. It is modeled as the exchange of virtual gluons between objects carrying color charge. It conserves strong isospin and strong hypercharge. There

[4]A virtual particle is one that exists only as a result of the Heisenberg Uncertainty Principle and cannot be directly observed.

are three color charges: red, blue, and green. No isolated color charges are observable, only color neutral (or white) combinations are allowed in the theory.

When a quark emits or absorbs a gluon, its color changes. Since a quark carries color or anti-color, there are eight possible color combinations for gluons, each carrying a combination of color and anti-color. Since gluons themselves carry color, they are able to interact with each other leading to a "sea" of gluons and quarks. This gluon self-coupling provides an anti-screening effect leading to a "running" coupling constant that is a function of Q^2. It can be expressed as:

$$\alpha_s(|Q^2|) = \frac{12\pi}{(11n_c - 2n_f)\ln|Q^2|/\Lambda^2}, \tag{2.18}$$

where $n_f = 6$ (number of flavors), $n_c = 3$ (number of colors) and Λ is the scale factor of the renormalization scheme. The running coupling constant leads to two important aspects of QCD: "asymptotic freedom" and "confinement".

Asymptotic freedom is the regime where the color charges are very close to each other. Small distance is equivalent to high-Q^2 (a region where calculation becomes possible in QCD known as the perturbative region), so in effect the coupling constant goes to zero and the particles behave as if they were free particles within the composite particle. Divergences in the calculation initially caused difficulties for the theory, but these have been resolved: ultraviolet (UV) divergences (integrations over large momenta) are removed through renormalization; infrared divergences (integrations over small momenta, collinear final states) cancel out if all physically indistinguishable initial and final states are taken into account. Probes of sufficient energy have the ability to resolve the constituent partons (quarks or gluons) within the composite particles and, using structure functions and factorization, it is possible to model the momentum fraction that the various partons carry within the composite particle.

Confinement, the second novel feature of QCD, is the property that as the particles get further away from each other (lower Q^2) the coupling strength grows. As a parton moves further away from its neighbors, the color "string" of gluons connecting it gains sufficient energy that it is easier to break the long string into two short strings between $q\overline{q}$ pairs. This leads to *hadronization*.

2.3.1.1 Jets

When a hadron participates in an interaction such that a parton is ejected with significant transverse momentum, it will undergo hadronization (due to confinement) and the $q\overline{q}$ pairs will combine into a collimated spray of particles in the direction of the scattered parton. The spray associated with an ejected parton is called a *jet*. The hadronization process cannot be completely calculated in QCD, however the measurable jet is assumed to have essentially the same four-vector as the final state parton, which can be treated perturbatively.

2.3.1.2 Parton Evolution

In the calculation of cross-sections, especially those involving hadrons, some additional tools are useful. First, since hadrons are composite particles, the momenta of the partons are often expressed in terms of *structure functions* which are in turn expressed as *Parton Distribution Functions* (PDFs). These PDFs are semi-empirical probability density functions of finding a parton within a hadron at a particular momentum fraction and renormalization scale. The momentum fraction is expressed in terms of the scaling variable Bjorken-x (represented by x) and the renormalization scale, represented by μ, (a measure of the mass scale at which a particular renormalization scheme is no longer applicable).

Invoking the principle of *factorization*, long- and short-distance dependence in the cross section can be split into a commutation of a perturbatively calculable part (*e.g.* Matrix elements or Feynman diagrams) and a semi-empirical part (the structure functions). Once factorization is applied, an additional scale dependence is introduced called the factorization scale (μ_f) which serves to define the separation of the short- and long-distance effects. Such a calculation takes place at a fixed-Q^2, however, so the concept of *evolution* is used to see how the PDFs change from μ to μ_f. At high scales, the phase space available rapidly expands leading to ill-behaved results in the renormalization. Because of this, resummation of the leading-log (LL) behavior to all orders helps reorder terms into a more rapidly converging series. Evolution is accomplished through the application of linked differential equations applied to the PDFs.

The most commonly used evolution scheme is DGLAP (Dokshitzer-Gribov-Lipatov-Altarelli-Parisi) [25, 26, 27, 28] evolution. DGLAP equations provide for evolution in Q^2 and is also known as collinear factorization. This scheme is very effective for high-Q^2 and high-x processes, so $1/x$ terms in the expansion are neglected. It provides a parton cascade that is strongly ordered in transverse momentum ($k_\perp$).

Diffractive events dominate in small-x situations where the $1/x$ terms of any evolution become important. As discussed in Section 2.1.1, the DGLAP evolution equations neglect such contributions and therefore are expected to break down in diffractive events. A different evolution scheme known as BFKL (Balitsky-Fadin-Kuraev-Lipatov) [29, 30, 31] evolution is strongly ordered in fractional momentum x, hence $1/x$ terms in the LL resummation are kept.

There is an additional evolution scheme called CCFM (Catani-Ciafaloni-Fiorani-Marchesini) [32, 33, 34, 35] evolution that attempts to unite BFKL and DGLAP evolution by introducing angular ordering and color coherence effects. At small-x it is equivalent to BFKL and as Q^2 increases approaches the DGLAP answer. This evolution scheme

is further modified into the Linked Dipole Chain Model (LDC) [36, 37] which is CCFM reformulated to have an explicit left-right symmetry.

2.4 Hard Diffraction

While the soft Pomeron model works well as a phenomenological description of soft diffraction, there is still some question as to whether or not actual particle(s) lie on the Pomeron trajectory. In an attempt to take the successful Regge phenomenology and combine it with perturbative QCD, Ingelman and Schlein [38] presented a simple model that allows the tools of Deep Inelastic Scattering (DIS) (as presented in Section 2.3.1.2) to be applied to hard diffractive events as a probe of the Pomeron structure in a way parallel to the probing of the internal proton structure.

2.4.1 Ingelman-Schlein Model

The Ingelman-Schlein model starts by positing Regge factorization (akin to the factorization described in Section 2.3.1.2). Under this factorization model a hadron emits a soft Pomeron (Fig. 2.8(a)) which carries a fraction of the initial nucleon momentum given by,

$$\xi = 1 - x_F = 1 - \frac{p_f}{p_i}, \tag{2.19}$$

where x_F is a scaling variable called Feynman-x, p_f is the final momentum of the particle emitting the Pomeron, and p_i is the initial momentum. The Pomeron then proceeds to interact with the other hadron in an inelastic manner, coupling through some internal structure (Fig. 2.8(b)). Diffraction dominates for $\xi < 0.05$ and the total mass accessible to the resultant central system is given by $M_x = \sqrt{\xi s}$ ($\xi = 0$ corresponds to elastic scattering).

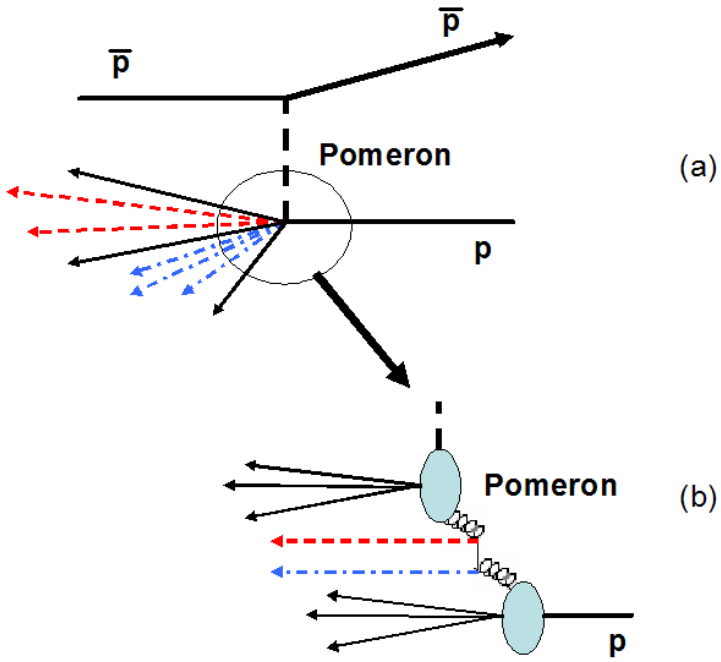

Figure 2.8 Schematic diagram of Ingelman-Schlein Regge factorization.

In this system, the hard differential cross-section can be written as,

$$\frac{d^2\sigma(p+\overline{p}\rightarrow\overline{p}+X)}{d\xi dt} = F_{I\!P/\overline{p}}(\xi,t)\sigma(I\!P+p\rightarrow X), \tag{2.20}$$

Where the term $F_{I\!P/\overline{p}}(\xi,t)$ is the Pomeron flux factor, or the probability that the $\overline{p}$ will emit a Pomeron with the values ξ and t, and the term $\sigma(I\!P+p\rightarrow X)$ is the cross section of a parton in the Pomeron interacting with a parton in the proton to give the final state X. The flux factor was found from a global fit by Donnachie and Landshoff [39] to be,

$$F_{I\!P/\overline{p}}(\xi,t) = \frac{9\beta_0^2}{4\pi^2}\xi^{1-2\alpha_{I\!P}(t)}\left[\frac{4m^2-2.8t}{(4m^2-t)(1-t/0.71)^2}\right]^2, \tag{2.21}$$

where $\beta_0^2 \approx 3.5$ GeV^{-2} and m is the nucleon mass. The remaining cross-section can be found from standard factorization processes to be,

$$\sigma(I\!P + p \rightarrow X) = \sum_{a,b} \int d\beta dx_b f_{a/I\!P}(\beta) \times f_{b/p}(x_b) \hat{\sigma}(a + b \rightarrow X), \tag{2.22}$$

where the only unknown is the structure function of parton a with momentum fraction β in the Pomeron ($f_{a/I\!P}(\beta)$). So, through measuring the differential cross-section, the Pomeron's internal structure can be probed. Following along with standard perturbative-QCD, the structure functions are evolved using the DGLAP evolution equations.

Building on an early suggestion of the simplest QCD Pomeron as consisting of two gluons, first proposed by Low and Nussinov [40, 41], Ingelman and Schlein suggested that hard diffractive jet events would be a good probe of the gluon component of the Pomeron structure, imposing the momentum-sum rule on the momentum fractions $\int_0^1 \beta f(\beta) d\beta = 1$ carried by the gluons (which is not necessarily true since the Pomeron is only a virtually exchanged particle). They proposed both a hard gluonic structure (one gluon carries most of the momentum) and a soft gluonic structure modeled after the gluonic structure of the proton. Shortly after, Donnachie and Landshoff proposed their own model [42] for the structure of the Pomeron consisting of two quarks.

The UA8 [43] collaboration at CERN discovered hard diffraction by observing jets in diffractive events [44], and later inferred a hard Pomeron structure [45]. ZEUS [46] and H1 [47] at HERA also found a substantial fraction of the Pomeron had a hard gluon structure [48, 49] and H1 also showed a hard quark component [49]. In light of these results, it is clear that the structure of the Pomeron is not simple, and therefore Bruni and Ingelman proposed [50] the study of diffractively produced W and Z^0 bosons to probe the quark structure of the Pomeron.

In addition, various measurements of diffractive events at the Tevatron have been made (*e.g.* CDF [51] results [52, 53] and DØ [54] results [3, 55]). In the HERA data, approximately 10% of inelastic events are diffractive [56]. Applying HERA diffractive PDFs to the theory at Tevatron energies results in cross-section predictions that are about a factor of 10 too high when compared to the actual measurement (*e.g.* [57]). Since multiple Pomeron exchange (which is $\sqrt{s}$ dependent) tends to spoil any rapidity gap or tag, this is expected, implying different diffractive PDFs need to be applied at Tevatron energies. Others propose modifying the flux factor (*e.g.* [58]), in order to maintain the universality of the diffractive PDFs.

All of these results seem to imply that hard diffractive probes might not actually be looking at the Regge soft Pomeron at all. Instead, there is the possibility of a "hard" Pomeron.

2.4.2 Hard Pomeron

Using BFKL evolution and starting with two gluons and adding higher order terms (virtual radiative gluons), we arrive at a reggeized gluon ladder with effective vertices as shown in Fig. 2.9. Further, by introducing an additional dependence in $k_\perp$, the resummed amplitude has a cut in the complex angular momentum plane that could play the role of the hard Pomeron. This $k_\perp$ dependence causes a different jet topology than the Ingelman-Schlein model allowing the theory to be probed in a collider situation.

Results from HERA show that $\alpha_{I\!P}(0)$ has an s dependence, meaning that there are at least two Pomeron trajectories in the Regge formalization. The trajectory for this BFKL hard Pomeron could best be described by an $\alpha_{I\!P}(0) = 1.4$ according to Donnachie and Landshoff [60].

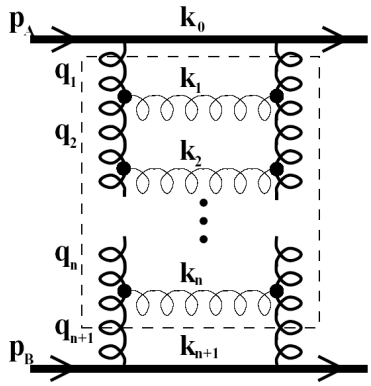

Figure 2.9 The contribution of a gluonic ladder with n rungs to the Pomeron exchange. The reggeized gluon propagators are represented by thick, vertical gluon lines [59].

2.4.3 Soft Color

The final explanation for diffractive events presented in this dissertation, does not require the use of a Pomeron at all. In the Soft Color Interaction (SCI) [61, 62] model, the underlying hard interaction is the same for diffractive and non-diffractive events. This model postulates that color, but not momentum, is transferred between the participating particles; color strings are simply rearranged and gaps form when there is no color connection between neighboring protons (shown in Fig. 2.10).

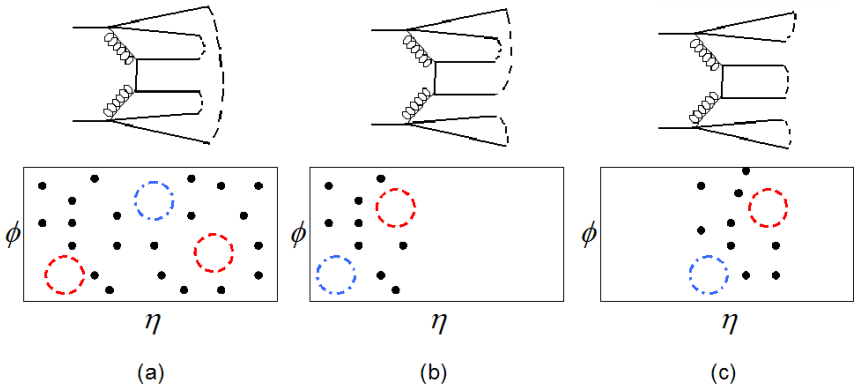

Figure 2.10 Schematic diagram of Soft Color Interaction for (a) non-diffractive, (b) hard diffractive, and (c) double Pomeron topologies.

This theory has only one free parameter (the probability of rearrangement occurring) and is non-perturbative. It has the same t-dependence as the Ingelman-Schlein model due to the primordial $k_\perp$ of the partons but predicts that the formation rate of gaps in gluon-gluon sub-processes is less than or equal to the formation rate in quark-quark sub-processes due to the relative difficulty in canceling the color in gluonic processes. A modification to the theory called the Generalized Area Law (GAL) [63] introduces an exponential suppression to color strings spanning a large area in $E - p$ space.

CHAPTER 3

THE DØ DETECTOR AT THE TEVATRON

Ironically, the current study of the smallest known particles in nature requires the use of mankind's largest machines. From the large accelerators that are capable of producing the energetic beams required, to the massive, sophisticated detectors necessary to contain and record the results of the high energy interactions, even the simplest analysis requires the collaboration of hundreds of individuals.

3.1 Fermi National Accelerator Laboratory

The Fermi National Accelerator Laboratory (FNAL) was commissioned by the US Atomic Energy Commission in 1967 and is located on a 6,800-acre site located about 40 miles west of Chicago in the town of Batavia, Illinois. Originally named the National Accelerator Laboratory, it was renamed in honor of Enrico Fermi in 1974 [64].

Fermilab is the home of the Tevatron, currently the world's highest energy superconducting accelerator [65]. Two collider experiments, CDF (Collider Detector at Fermilab) [51] and DØ (named after its location along the Tevatron ring) [54] study the products of interactions of the colliding beams. In addition, Fermilab is the home to several accelerator-based neutrino experiments [66, 67].

Two major discoveries in support of the Standard Model were performed at Fermilab. Evidence that could only be accounted for in the model by including new quarks was obtained for the bottom quark in 1977 [68] and the top quark in 1995 [69, 70]. The

first direct observation of CP violation was performed there in 1999 [71] and the first direct observation of the tau neutrino in 2001 [72].

3.1.1 Accelerator Complex

Originally known as the Energy Doubler, the Tevatron at Fermilab started operations in 1983 with a 512 GeV proton beam. In 1984, it first attained 800 GeV beams. The first $p\overline{p}$ collisions were observed at CDF with a $\sqrt{s} = 1.6$ TeV center-of-mass energy in 1985. The lab first attained $\sqrt{s} = 1.8$ TeV collisions in 1986. Collider Run I, which included the DØ detector, began in 1992 and in its 4 years of collisions delivered luminosities of approximately 130 pb^{-1} to each collider detector. The accelerator and detectors underwent upgrades after the end of Run I and in March 2001, Collider Run II began with a center-of-mass energy of $\sqrt{s} = 1.96$ TeV [73].

The accelerator complex is a chain of particle accelerators at increasing energies and as shown in Fig. 3.1. It is made up of 8 individual (linear and circular) accelerators with a total length in excess of 9000 meters and consuming energy at a rate of 30 MW. The individual accelerators comprising the complex include:

- Proton Source (Pre-accelerator, Linear Accelerator);
- Booster;
- Main Injector;
- Antiproton Source (Debuncher, Accumulator and Recycler);
- Tevatron.

The information that follows is drawn primarily from references [74, 75, 76].

3.1.1.1 Proton Source

First in the chain is the *Cockcroft-Walton pre-accelerator* [77] where hydrogen gas is ionized to create H^- ions. These ions are accelerated by a positive voltage to 750 keV

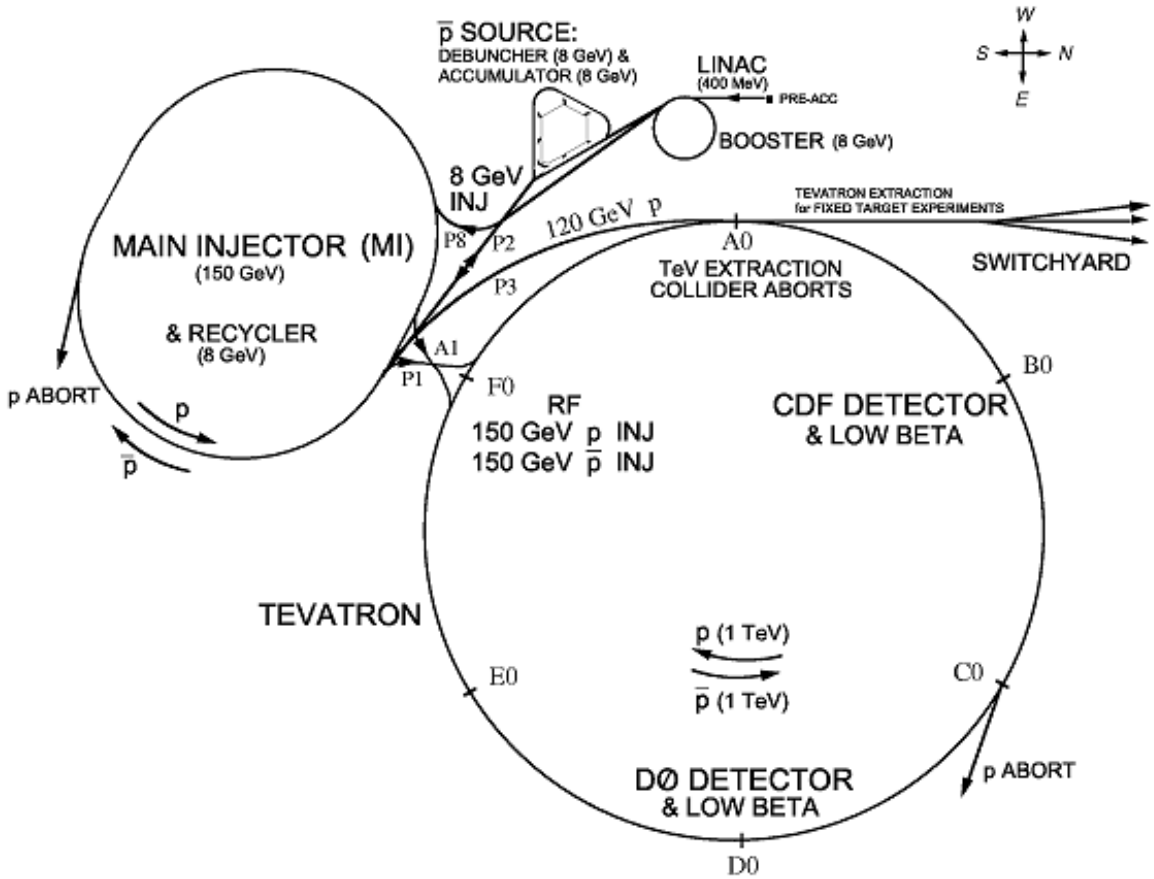

Figure 3.1 Schematic view of the Fermilab accelerator complex.

in a continuous stream. From here they are led into an approximately 130 meter long *linear accelerator* (LINAC). In the LINAC, the ions are accelerated to 400 MeV through the use of radio frequency (RF) oscillating electrical fields inside of copper cavity drift tubes. As the particles pass down the LINAC, the size of the cavities and the spacing between them increases leading to a bunching of the particles. At the end of the LINAC, the bunches are passed through a carbon foil which strips both electrons from the ions leaving bunches of bare protons.

3.1.1.2 Booster

The proton bunches are then steered into the *Booster*, which is a 475 meter circumference fast-cycling synchrotron located 20 feet below ground. In the Booster, a series of magnets carrying both quadrupole and dipole fields is used to focus and bend the bunches around the ring in a closed circular orbit. They are accelerated to an energy of 8 GeV via a set of 18 interspersed RF cavities in a period of 0.033 seconds. Through the principle of phase stability, the RF frequency and magnetic field strength are balanced to keep the particles in the ring. The RF frequency also keeps the particles in a bunch centered in an RF bucket. The bunches are then sent on to the Main Injector.

3.1.1.3 Main Injector

The *Main Injector* (MI), completed in 1999, is a long synchrotron ring, 3 kilometers in circumference, composed of 18 RF cavities and separate quadrupole and dipole magnets. It is used:

- to accelerate proton bunches from the Booster to 150 GeV in preparation for injection into the Tevatron;
- to accelerate proton bunches from the Booster to 120 GeV which are then used for simultaneous antiproton production and fixed target/neutrino production;
- to receive antiproton bunches from the Accumulator or the Recycler and increase their energy to 150 GeV in preparation for injection into the Tevatron;
- to inject the proton and anti-proton bunches into the Tevatron.

3.1.1.4 Antiproton Source

To produce antiprotons, proton bunches accelerated to 120 GeV are extracted from the MI every 1.5 seconds and collided with a nickel target at the *Target Station*

in the Antiproton Source. Protons in the bunches interact with protons in the nickel to produce a proton - antiproton pair, in addition to an abundance of secondary particles. The bunched particles come out at relativistic energies in all directions. A lithium target acts as a lens to focus the resultant particle bunch into a linear beam that is passed through a pulsed magnet which acts as a mass-charge spectrometer tuned to gather 8 GeV antiprotons. This is an inefficient process, with approximately 20 antiprotons produced for every 1 million protons hitting the target.

Because of the messy nature of this collision process, there is a large spread in the momentum of the resulting antiprotons (as the particles are sprayed in various directions). These antiprotons are focused and collected into the *Debuncher* where large energy fluctuations with a small time spread are transformed into a small energy fluctuations with a large time spread (through the use of RF cavities over the period of 100 milliseconds). In the remaining time before the next bunch from the MI, the antiprotons are further "cooled" through Stochastic cooling[1]. Before the next bunch from the MI, the cooled antiprotons are passed on to the *Accumulator* storage ring where they are stored using a technique referred to as momentum stacking where they wait to be returned to the MI while undergoing continued RF and stochastic cooling to keep them at the desired momentum and beam size. Antiprotons in the Accumulator or those returning from the Tevatron can be inserted into the *Recycler* for longer term storage before being injected. The Recycler, which shares the same tunnel as the MI, can increase the number of antiprotons produced and available for collisions since the production efficiency for antiprotons decreases as the number being stored in the Accumulator increases. In

[1]Particles leaving the target have a wide range of energies, positions and angles. This randomness is equivalent to thermodynamic temperature so we say the beam is "hot". In order to intensify the beam and allow it to pass through the beam apertures, it needs to be "cooled". Stochastic cooling is a technique used to remove this randomness on a particle by particle basis through the use of feedback systems [78].

addition, antiprotons surviving from a previous store can be circulated in the Recycler and reused in future stores, increasing the number of particles available for collisions.

3.1.1.5 Tevatron

Bunched protons and antiprotons are inserted into the 4 mile circumference *Tevatron* ring from the MI and accelerated to 980 GeV through the use of RF cavities over the course of 85 seconds. The beams are focused and steered around the ring using almost 1000 separate superconducting magnets operating at a temperature of 4.3 K with a field strength of 4.2 T. Once the bunches are accelerated, the two beams are brought to collision at a center-of-mass energy of $\sqrt{s} = 1.96$ TeV at two pre-determined points around the ring at which the CDF and DØ detectors are located.

As stated previously, the beam provided to the experiments comes in bunches, and the resulting time structure in the delivery of collisions is used in the triggering selection of data. This time structure is the Tevatron Clock. Both protons and antiprotons are propagated in 36 bunches divided evenly between 3 superbunches. The bunch spacing between neighboring bunches within a superbunch is 396 nanoseconds with a separation of about 2 microseconds between adjacent superbunches. A typical proton bunch carries about 2×10^{11} particles while a typical antiproton bunch carries about 2×10^{10} particles. This provides approximately 1.5 interactions per beam crossing with a typical instantaneous luminosity of about 1×10^{32} cm^{-2}s^{-1} at the beginning of each *store* (period of prolonged collisions). The delivered integrated luminosity is therefore about 18 pb^{-1}/week. By increasing the numbers of particles (primarily antiprotons) the delivered luminosity it expected to increase as Run II progresses [79].

3.2 The DØ Detector

The DØ Experiment consists of about 680 physicists from over 83 institutions in 19 countries [80]. The primary purpose of the experiment is to perform research in the fundamental nature of matter with an emphasis on high mass and large p_T phenomena. For Run II, this also includes vigorous B physics and diffractive physics programs.

The experiment makes use of a massive detector consisting of many subsystems. For Run II, the DØ Detector [81, 82] is an essentially new detector redesigned to handle higher luminosities. There are also several new subsystems. The Run II central DØ detector is shown in Fig. 3.2. The configuration (from the center of the detector outwards) is:

- Silicon Microstrip Tracker;
- Central Fiber Tracker, Solenoid and Preshowers;
- Luminosity Monitor;
- Calorimeter System;
- Muon System;
- Forward Proton Detector (not shown in Fig. 3.2 and described in more detail in Chapter 4).

The Data Acquisition System (DAQ) takes the signals from all of the subsystems and combines them into 128 triggers. These are used to select interesting data events. Triggered events are written to tape for later analysis. In this dissertation, emphasis will be placed on those subsystems most relevant to this analysis. In addition, to those listed previously in this Chapter, information in the following sections is drawn from references [83, 84, 85].

3.2.1 Coordinate System and Variables

DØ uses a right-handed Cartesian coordinate system. In this coordinate system, $+z$ is in the direction of the proton beam around the ring, $+y$ is vertically upwards, and

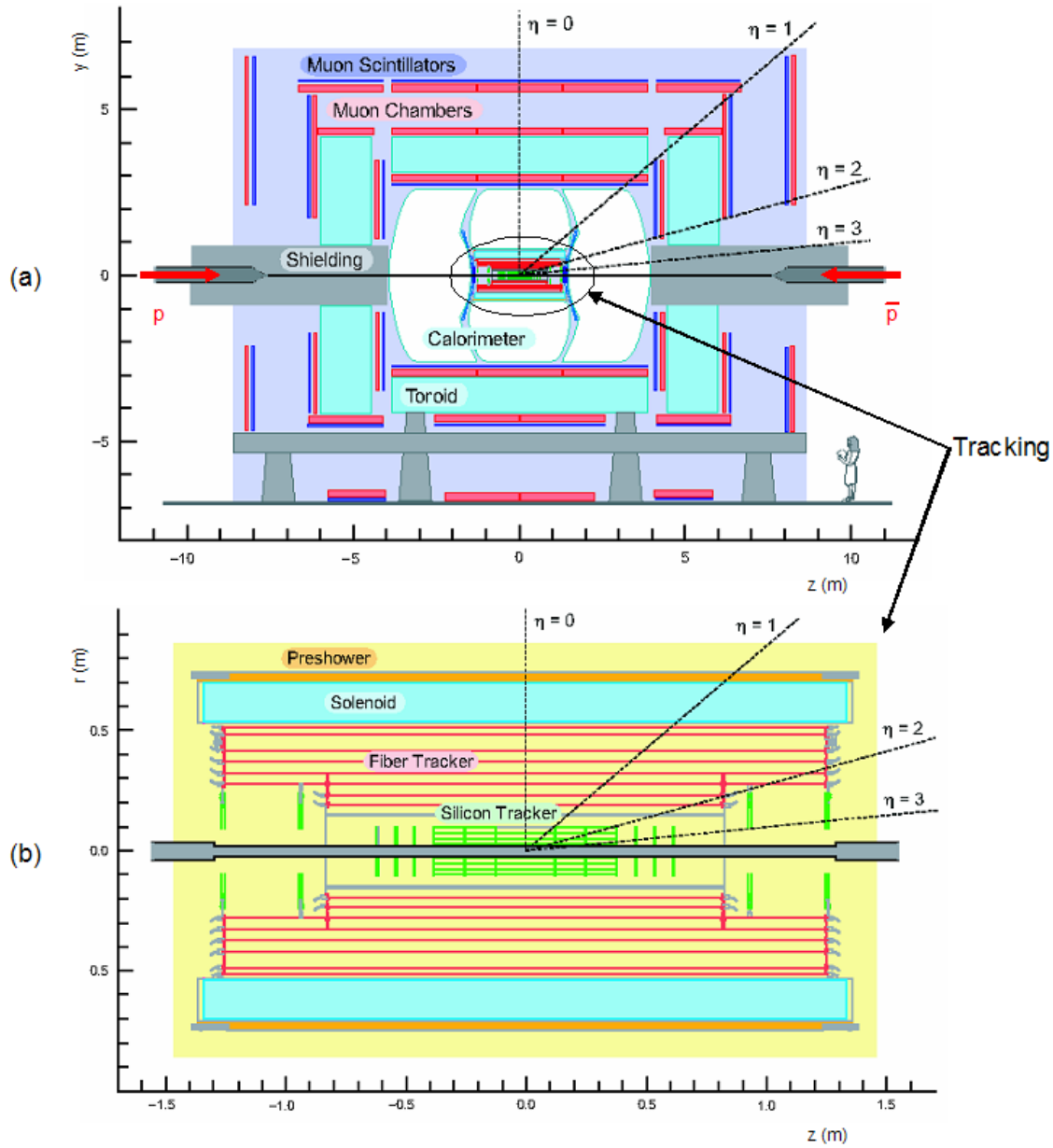

Figure 3.2 Schematic diagram of the central DØ Run II detector showing (a) $y - z$ slice out to the muon detectors and (b) $r - z$ slice of the tracking system.

$+x$ is perpendicular to y away from the center of the ring. For the DØ detector, the origin of this coordinate system is the nominal center of the detector [76, 79].

Due to the cylindrical nature of the calorimeter, the cylindrical polar coordinate system is also used where r is the radial distance from the z-axis (related to the Cartesian system through $r = \sqrt{x^2 + y^2}$); ϕ is the azimuthal angle (related through $\phi = \tan^{-1}(y/x)$ with $\phi = 0$ along the $+x$-axis); and θ is the polar angle (angle with respect to the z-axis) with $\theta = 0$ in the positive z direction.

The actual Interaction Point (IP) or Primary Vertex (PV) can be reconstructed within these coordinate systems via various methods and all variables are then recalculated relative to this IP (physics coordinate system). Unless otherwise noted, the physics coordinate system is used in expressing any variables in this dissertation. If the detector coordinates are being used, the subscript *det* will be applied to the variable.

Because the particles at a hadron accelerator are ultra-relativistic, and the initial momentum transfer between partons within the interacting $p\overline{p}$ collision is not known, it is useful to work with variables that are not sensitive to boosts along the z-axis (longitudinal direction). Therefore, most coordinates are parameterized as Lorentz-vectors in functions of the total energy E, the transverse energy $E_T = E \sin\theta$ (or the transverse momentum $p_T = \sqrt{p_x^2 + p_y^2}$), ϕ and rapidity, y, where y is defined as:

$$y = \frac{1}{2} \log \left(\frac{E + p_z}{E - p_z} \right). \tag{3.1}$$

In the limit that $m/E \to 0$ (mass become negligible in comparison to particle energy), the rapidity y reduces to "pseudorapidity",

$$\eta = -\ln \left(\tan \left(\frac{\theta}{2} \right) \right), \tag{3.2}$$

which is a useful function of the polar angle θ.

It is often useful to look at the distance (ΔR), between objects in (η, ϕ) space. This is defined as,

$$\Delta R = \sqrt{(\Delta\phi)^2 + (\Delta\eta)^2}, \tag{3.3}$$

where $\Delta\phi$ and $\Delta\eta$ are the distances between two objects in the (η, ϕ) frame.

3.2.2 Magnets

To measure charged particle momenta, the curvature of the track in the presence of a magnetic (B) field is used. A magnetic field $B = 2$ Tesla (changed to 1.92 Tesla after the Fall 2004 shutdown) is provided in the region of the central tracking system by a superconducting solenoid magnet which is a two layer coil that is 2.75 m long, 0.32 m thick, and has a radius of 60 cm. This magnet was designed to introduce only a small amount of material before the calorimeter to minimize conversion of photons into e^+e^- pairs and multiple Coulomb interactions.

The Run I toroidal magnet is used to provide the B-field in the muon system for Run II. This toroidal field has field lines perpendicular to the beam axis with a strength of 1.8 T. The iron of the toroid magnet is also the return yoke for the central solenoid. The local values of the B fields within the tracking volume and the muon system are maintained in a field map for use in track reconstruction.

3.2.3 Silicon Microstrip Tracker

The Silicon Microstrip Tracker (SMT) [86] is part of the DØ tracking system located within the solenoid field (see Fig. 3.2(b)). The SMT is a high resolution system and the first set of detectors which particles pass through when emerging from the collision. The SMT gives a more precise measurement of the position of the vertex of the collision as well as a better separation and measurement of any secondary vertices (crucial for certain

heavy flavor analyses). The use of a silicon semiconductor tracking device was motivated by the following properties of silicon:

- Low ionization energy (good detectable signal);
- Long mean free path (good charge collection efficiency);
- High mobility (fast charge collection);
- Low-Z (low atomic number means fewer multiple scatterings);
- Well-developed technology.

The SMT is designed as a hybrid system consisting of *barrel detectors* measuring $r-\phi$ and *disk detectors* measuring $r-z$ as well as $r-\phi$ as shown in Fig. 3.3. This design was motivated by the fact that the z distribution of the IP is approximately Gaussian with $\sigma_z = 28$ cm due to the structure of the $p\overline{p}$ bunches. Because of this, it is difficult to design a detector such that tracks are basically perpendicular to the detector surfaces at all η. The hybrid design provides a solution to this problem. With this system, tracks for high η particles are reconstructed primarily by the disks while small η particles are reconstructed by the barrels. The central SMT has an outer radius of 16 cm (26 cm for the H-disks) with an η coverage of $|\eta_{det}| < 3$. There are almost 800,000 channels for the entire SMT system.

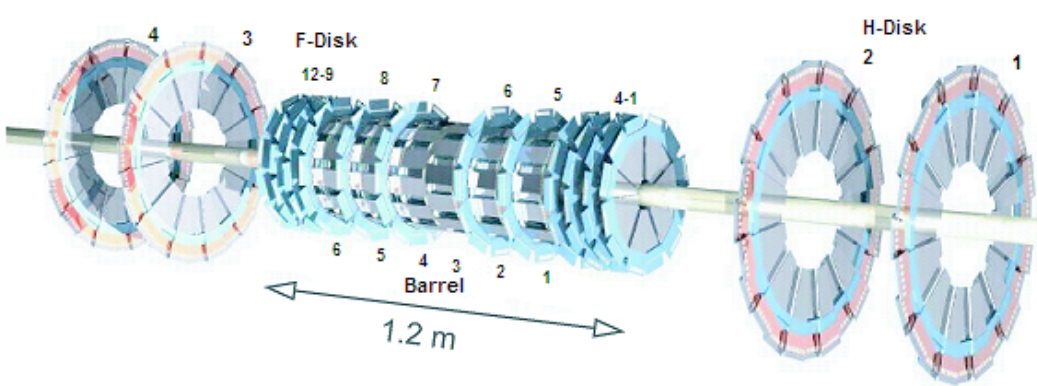

Figure 3.3 Schematic drawing of the SMT detector.

Conceptually, the barrels and disks have the same structure. For a barrel detector, the basic unit is called a *ladder* while for the disk detector it is called a *wedge*. These ladders and wedges are constructed of single and double-sided microstrip detectors, with the latter measuring the position by means of a stereo angle (*i.e.* relative angle of alignment) between strips. The composition of the various types of detectors is listed in Table 3.1. The SMT contains six barrel detectors of 4 layers. Layers 1 and 2 have 12 ladders each while layers 3 and 4 have 24 ladders each. There are 12 F-disk detectors placed between and outside of the barrels consisting of 12 wedge detectors each and 4 H-disk detectors further out. The H-disk detectors are constructed of 24 full wedges constructed of two single-sided half-wedges glued back-to-back.

Table 3.1 Summary of SMT sub-detector and sensors [79]

	channels	**sensor type**	**stereo angle**	**# chips**	**strip pitch**
barrels 2-5	276.5k	double-sided	90°	6	50/153 μm
(High Occup.)		double-sided	2°	9	50/67 μm
barrels 1 and 6	111.0k	single-sided	-	3	50 μm
(Low Occup.)		double-sided	2°	9	50/67 μm
F-disk	258k	double-sided	±15°	14	63 μm
H-disk	107k	single-sided	±7.5°	6 x 2	80 μm

An individual micro-strip detector consists of silicon *sensors*. Each sensor is a one-sided n-type silicon wafer (300 μm thick) with variable strip pitch depending on location. As a charged particle of sufficient energy passes through the silicon, it will produce electron–hole pairs in the detector material. This current is drawn to the strips by a high electric field. The strips are connected to SVXII*e* (Silicon VerteX) chips which are able to measure the deposited charge per strip using ADC (Analog to Digital Converter) pipeline technology. Each chip has 128 readout channels. The number of chips used for a particular micro-strip detector varies by detector type, but all chips are accessed via a readout hybrid called the High Density Interconnect (HDI).

The ladders and wedges are mounted on bulkheads made out of beryllium. In addition to providing mechanical support, it also serves as an enclosure for the water and glycol coolant system which maintains the detectors at $-7°$ C to optimize the performance of the silicon. The system is able to measure the tracks of particles with a resolution of ~ 10 μm.

3.2.4 Central Fiber Tracker and Preshower Detectors

The Central Fiber Tracker (CFT) is a scintillating fiber tracker that surrounds the silicon detector and lies within the solenoid magnetic field (see Fig. 3.2(b)). It is used to perform track reconstruction and momentum measurement for charged particles and overlaps with the SMT within the range $|\eta_{det}| < 2$. Combining the hit information from the two tracking systems allows improved overall tracking quality. The CFT, however, provides faster track triggering (in the range $|\eta_{det}| < 1.6$) because its signals are processed faster than the SMT.

A total of about 76,800 scintillating fibers are mounted on eight concentric carbon-fiber support cylinders, positioned with an accuracy of 25 μm. Each cylinder supports a doublet layer of fibers oriented in the axial direction, parallel to the beam, and a doublet layer of fibers that is oriented with a $\pm 3.0°$ stereo angle allowing measurement of the z coordinate. Stereo layers alternate between plus and minus stereo angle orientation. This layout provides a hit resolution of 100 μm in r, ϕ.

The detection unit of the system is the multi-clad scintillating fiber. The inner polystyrene core with index of refraction $n = 1.59$ is doped with paraterphenyl and a wave-shifting dye and is surrounded by two layers of cladding (acrylic with $n = 1.49$ and fluoro-acrylic with $n = 1.42$). The fiber diameter is 835 μm and each cladding is 15 μm thick. The fiber scintillates in the yellow-green part of the visible spectrum with a peak emission wavelength near 530 nm.

A minimum ionizing particle produces only a few photons by scintillation. These photons propagate through the fiber via total internal reflection. The scintillating fibers are mated to clear waveguides by plastic, diamond-polished optical connectors. These waveguides conduct the scintillation light to Visible Light Photon Counters (VLPC), which are variants of solid-state avalanche photodiodes, operating at ~ 9 K. These devices have a high quantum efficiency ($\sim$80%) and a high signal gain of over three orders of magnitude.

The signals from the VLPCs are handled by custom Analog Front End (AFE) boards. The AFE boards contain charge-sensitive amplifiers to handle the small signals from the VLPC. The AFEs are part of the readout as well as the fast trigger decision. Each board has 8 Multichip Modules (MCM). Each MCM consists of four SIFT (ScIntillator Fiber Tracker) chips and the same type of SVXII*e* chips used for the silicon tracker as described in Section 3.2.3. The SIFT chip takes the signal from the VLPC and after amplification splits the signal and sends it along two paths: one to the SVX for later digitization and readout and the other to a discriminator used in triggering.

The Central Preshower (CPS) and Forward Preshower (FPS) detectors were designed for the Run II upgrade to enhance electron and photon identification as well as to correct the electromagnetic energy measured in the calorimeter for the effects of the uninstrumented solenoid material.

Both the CPS and FPS make use of triangular scintillator strips with embedded wavelength shifting fibers and make use of the same VLPC and AFE readout as mentioned for the CFT in Section 3.2.4. The preshower detectors are described in more detail elsewhere [87].

3.2.5 Calorimeter

The primary purpose of the calorimeter is to provide energy measurement. It also provides limited particle identification and course tracking of particles back to a vertex. In addition, it is used to improve the measurement of muon momenta.

At DØ the calorimeter is constructed of an *absorber material* (depleted uranium, copper or steel) that induces electromagnetic and hadronic showering from energetic particles and absorbs sufficiently low energy outgoing particles, combined with an *active medium* (liquid argon) that samples the ionization energy produced by particles showering through the detector. Liquid argon has the disadvantage that an intricate cryogenic system is necessary to operate the calorimeter at low temperatures of approximately 80 K. However, once installed, the calorimeter is radiation-hard and easy to maintain. The calorimeter is designed to maximize the amount of showering energy that is captured within its confines. Weakly interacting neutrinos and high energy muons escape. Escaping muons can be detected in the muon system behind the calorimeter while neutrinos produced in an event leave behind an overall imbalance in the event transverse energy (missing Et).

The layout of the calorimeter can be seen in Fig. 3.4. Since the tracking and solenoid are within the cavity of the central calorimeter, there needs to be a method to access this area. To allow this access, the calorimeter is designed in three modules: the *central cryostat* (CC) weighing about 330 tons and two *end-cap cryostat* (EC) weighing about 240 tons. Each boundary between the CC and the ECs was chosen to be perpendicular to the beam direction in order to reduce degradation in the missing transverse energy measurement. Each cryostat is further divided longitudinally into three sections of varying layers: the *electromagnetic* (EM), consisting of depleted uranium absorbers; the *fine hadronic* (FH), consisting of uranium-niobium (2%) absorbers; and the *coarse hadronic* (CH), consisting of copper absorbers in the CC and steel absorbers in the EC.

Each layer is further divided into *cells*. Cells in successive layers are offset from each other to reduce the possibility of particles passing through the calorimeter without any showering.

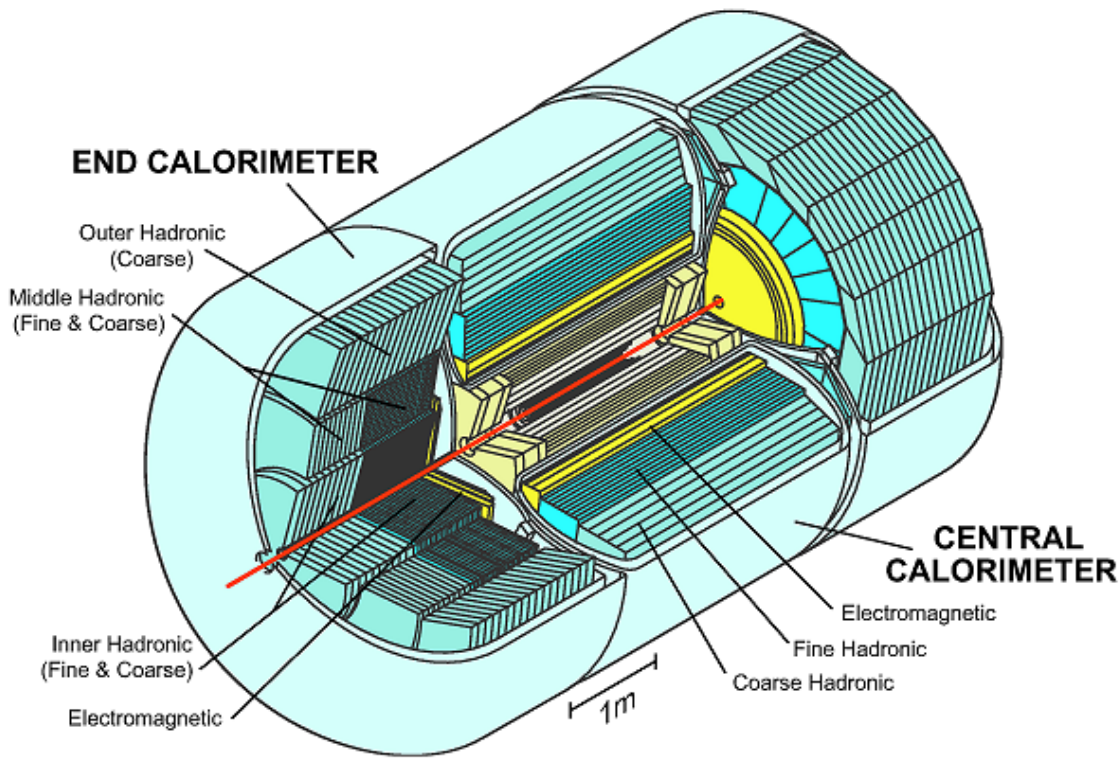

Figure 3.4 Schematic view of the DØ Liquid Argon / Uranium Calorimeter.

A calorimeter *unit cell*, displayed in Fig. 3.5, is the basic unit from which the signal is collected. It consists of an absorber plate followed by a 2.3 mm gap filled with liquid argon, readout electronics, and a final gap. Electron-ion pairs produced via ionization in the liquid argon are collected by electrodes in a strong electric field. The absorbers form the ground electrodes (cathodes) while the readout boards are placed at $2.0 - 2.5$ kV to serve as anodes. Each readout board consists of copper readout pads sandwiched between 0.5 mm G10 plastic plates covered with a resistive epoxy coating. The high voltage is

applied to the resistive coat, and charge collected at this coat induces a charge on the copper pads via capacitive coupling. In all, the calorimeter has about 50,000 of these unit cells.

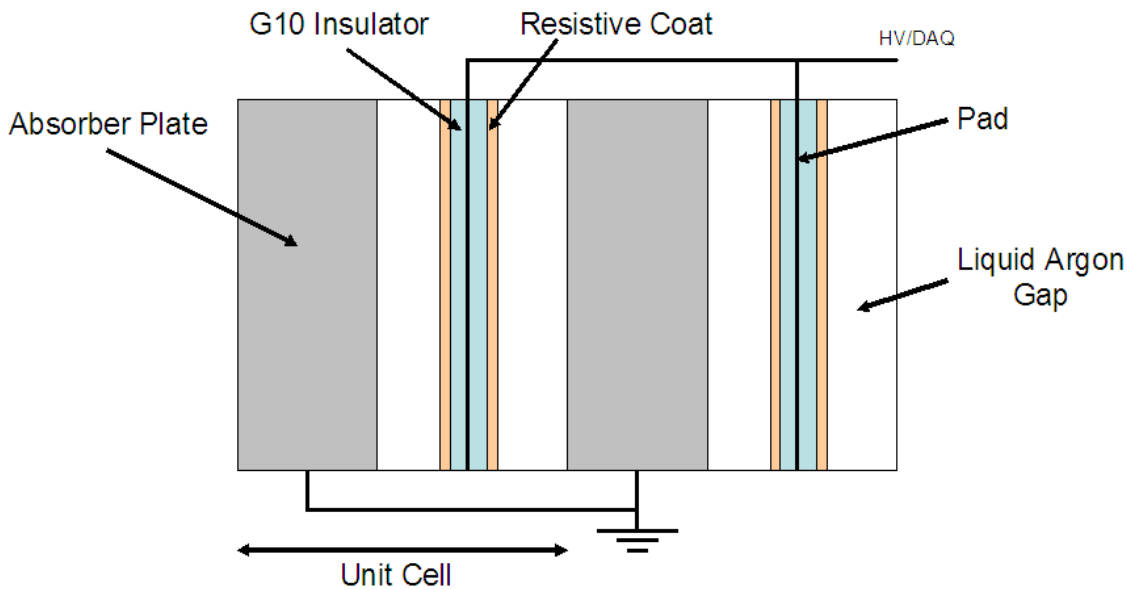

Figure 3.5 Schematic view of the calorimeter cell structure.

A *readout cell* is a combination of several adjacent unit cells in order to increase the measured current. Its typical size is $\Delta\phi_{det} \times \Delta\eta_{det} = 0.1 \times 0.1$. A set of cells (one from each layer) that is aligned in the outward direction (approximate direction of shower development) from the interaction point is called a *tower*. The calorimeter tower geometry is shown schematically in a quadrant cross sectional view in Fig. 3.6. This geometry is pseudo-projective, meaning that the cell centers in the tower lie on a ray originating from the geometrical center of the detector, while the cell boundaries are aligned perpendicular to the absorber plate. This leads to the "staircase" shape seen in the figure.

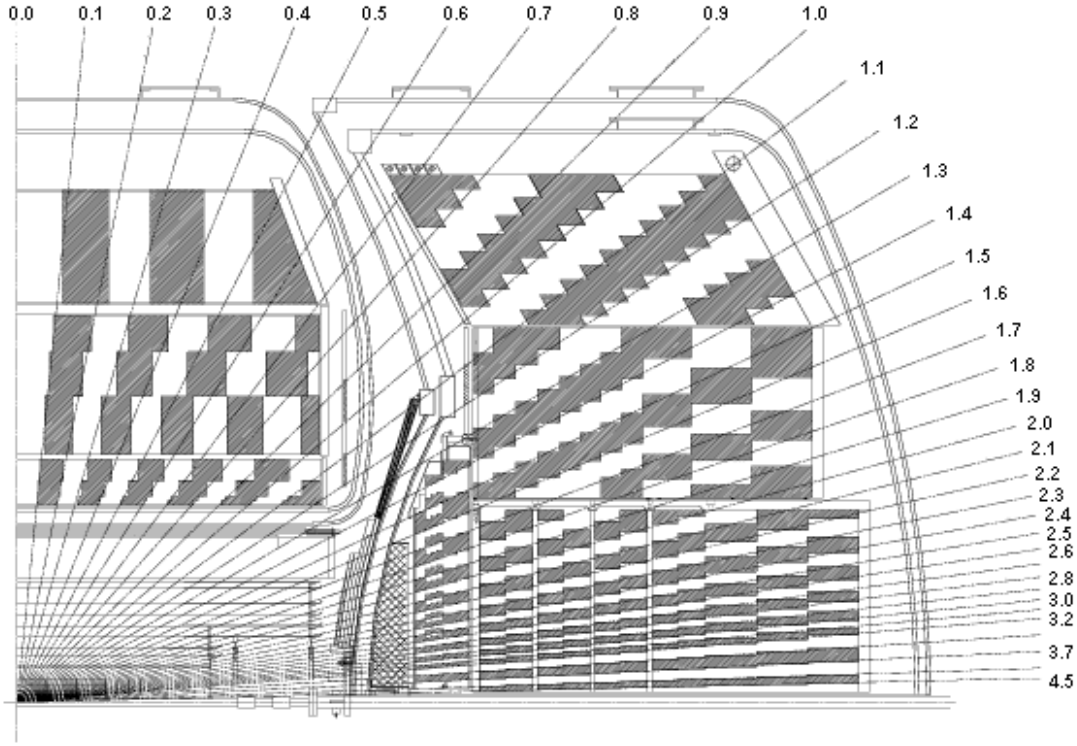

Figure 3.6 Quadrant cross sectional view of DØ pseudo-projective towers.

As designed, the DØ calorimeter is a *compensating calorimeter*. This means that the response to electromagnetic objects is the same as for hadronic ones. At DØ the measured ratio of e/π energy is less that 1.05 for energies above 30 GeV (however, the hadronic and electromagnetic part of a calorimeter energy shower can significantly fluctuate on a jet by jet basis – see Section /refsec:jet).

3.2.5.1 Central Calorimeter

The central cryostat covers the region up to $|\eta_{det}| \lesssim 1$ but the boundary of the last pseudo-projective tower for which all EM, FH and CH layers are contained in the CC corresponds to $|\eta_{det}| = 0.7$. Towers at larger pseudorapidity extend to the end caps.

The electromagnetic part has four layers (EM1, EM2, EM3 and EM4) aligned radially with respect to the beam. Their thicknesses in terms of radiation length[2] (X_0), is approximately 2.0, 2.0, 6.8 and 9.8 respectively. The first two layers sample the early stages of the electromagnetic shower where photons and π^0s differ statistically. Electromagnetic objects deposit most of their energy (typically 65%) in the third layer, motivating a reduction in the cell size by a factor of two to allow for more precise location of EM shower centroids. The full EM module comprises $20.6X_0$.

The hadronic part consists of three layers in the fine hadronic section (FH1, FH2 and FH3) and one layer in the coarse hadronic section (CH1). The corresponding depths in terms of nuclear interaction length[3] (λ_A), are 1.3, 1.0, 0.76 and 3.2 respectively. The total thickness of the calorimeter is $7.2\lambda_A$, including the EM part. This is large enough to absorb almost all of the energy released by incident particles from the interaction and their resultant showers. According to a Run I study [88], based on a measurement of the energy loss of charged pions as a function of λ_A [89] by the NuTeV collaboration [90] and also from Monte Carlo simulations of the calorimeter response, less than 0.5% of the energy for $E_T \sim 400$ GeV jets is expected to escape ("punch-through") the central hadronic calorimeter.

3.2.5.2 End-cap Calorimeter

Two end-cap cryostats are attached to the north and south ends of the central cryostat. The electromagnetic layers provide coverage in the region $1.3 < |\eta_{det}| < 4.1$. The hadronic layers provide coverage in the region $0.7 < |\eta_{det}| < 5.2$ Because of the location of the end-caps, their construction differs from the central cryostat. For cells beyond $|\eta_{det}| > 3.4$, the segmentation becomes twice as course as in order to avoid very

[2] A scaling variable for the probability of bremsstrahlung pair production within a given medium.

[3] A scaling variable for the mean free path of a particle before undergoing an interaction that is neither elastic nor diffractive within a given medium.

small physical cell sizes. The electromagnetic part of the EC has four layers (EM1, EM2, EM3, EM4), aligned in the z-direction, with thicknesses 0.3, 2.6, 7.9 and $9.3X_0$ respectively. The hadronic part consists of three separate modules (see Fig. 3.6). The inner hadronic (IH) module, located just behind the EM module, comprises four fine hadronic layers (each $1.1\lambda_A$ deep) and one course hadronic layer ($4.1\lambda_A$ deep). The middle hadronic (MH) module has a ring shape and surrounds the IH module. It contains four fine hadronic layers (each $0.9\lambda_A$ deep) and one coarse hadronic layer ($4.4\lambda_A$ deep). Furthest from the beam is the outer hadronic (OH) module. The layers are inclined at an angle of about 60° with respect to the beam axis. The maximum thickness is $6.0\lambda_A$.

3.2.5.3 Intercryostat Detector

A significant amount of dead material is located in the gaps between the central and end-cap cryostats. This dead area is primarily made up of cryostat walls, calorimeter support and readout cabling. These gaps cover a region $0.8 \leq |\eta_{det}| \leq 1.4$. A correction for the energy losses deposited in the uninstrumented material can be applied using the *InterCryostat Detector* (ICD). This scintillator-based detector was designed and built at UTA and covers the region $1.1 < |\eta_{det}| < 1.4$. These counters help reconstruct EM showers. The ICD arrays are mounted on the EC calorimeters, facing the gap. The size and position of the tiles corresponds to the calorimeter towers with a total of 376 scintillator tiles. The ICD is supplemented by a single-cell structures called the *massless gaps* (calorimeter readout cells before the first layer of uranium). The "massless gap" cells are installed both on the CC and the EC. Together, the ICD and massless gaps provide correction to the standard DØ sampling of hadronic showers to account for dead regions of the calorimeter.

3.2.5.4 Calorimeter Readout

While the bulk material of the calorimeter is the same as used during Run I, completely new readout electronics were installed for Run II. This was required due to the new beam structure and timing.

The charge collected by a readout cell is proportional to the energy deposited by the shower in the active media. This collected charge is integrated and transformed into proportional voltage pulses. These pulses are then sent along two paths, one leading to the fast trigger while the other leads to BaseLine Subtraction (BLS) boards. The BLS boards perform cell signal sampling just before and after a beam crossing and determine the difference between the two. This is done to separate the signal coming from an event from noise (an average signal in the cell when no beam is present) and previous collision remnants (necessary because the pulse decay of the signal is longer than the bunch timing of the beam). Only cells with a final value bigger than a certain multiple of the cell noise width are readout (zero suppression readout).

3.2.6 Luminosity Monitor

At DØ, luminosity is measured using information from the Luminosity Monitor (LM). The LM consists of two hodoscopes of scintillation counters mounted on the inside face of each end cryostat near the beam pipe. Each hodoscope is made up of 24 wedges and both are located at $|z| \approx 140$ cm. They each have a pseudorapidity coverage of $2.7 < |\eta_{det}| < 4.4$ and are within the magnetic field of the central solenoid. This system provides a time of flight resolution of approximately 200 ps. The scintillation light is read out using photomultiplier tubes.

These counters are primarily designed to measure the rate of inelastic collisions by detecting the resulting showers of particles that are produced in both directions along

the beam axis. The luminosity ($\mathcal{L}$) is determined from the average number of inelastic collisions per bunch crossing and is corrected for the acceptance and efficiency of the LM detectors. Since the interaction rate can differ for each bunch crossing, a database is maintained to record the different luminosities per bunch. The luminosity can be measured to an accuracy of 6.5% due to cross-section measurement uncertainty which takes into account the acceptance and efficiency of the LM detector.

In addition, by using the relative timing of the North and South monitors when there is activity on both sides of the interaction, it is possible to make either a vertex position measurement (fast z), or a measurement of proton or antiproton halo rates and to detect multiple $p\overline{p}$ interactions. Of particular interest in this analysis is the absence of luminosity monitor activity on either one or both sides of an event but with significant energy deposited elsewhere in the main detector. This is used to trigger on events with a possible forward rapidity gap[4]. This is one of the possible signatures of a diffractive event.

The signals from the LM system are split along two paths. The analog sum of the signals along one path is formed for each of the two arrays and these are then timed using a Time to Digital Converter (TDC) for selecting $p\overline{p}$ collisions. On the other path, the signals are processed by custom VME (Versa Module Eurocard) boards. A LM-TDC board is used to digitize the time and charge for each signal. This information is then fed to a LM-VTX (VerTeX) board that provides trigger terms to the Level 1 trigger as described in Section 3.2.8.

3.2.7 Muon System

The muon system is the outermost detector of the central DØ detector system. Because muons have a mass much higher than electrons, muons with an energy above

[4]A gap is a region of pseudorapidity where no particles are detected above a minimal threshold energy.

approximately $3.5 - 4.0$ GeV pass through the inner DØ detectors with minimal energy loss. Because of this, the muon detector surrounds the calorimeter and is well protected from the debris of electronic and hadronic showers by the calorimeter material. Timing in the muon system is useful in detecting cosmic rays passing through the detector.

The muon detector consists of three major components:

- Wide Angle MUon Spectrometer (WAMUS) with coverage $|\eta_{det}| < 1$;
- Forward Angle MUon Spectrometers (FAMUS) with coverage $1 < |\eta_{det}| < 2$;
- Solid-iron toroidal magnet.

The *WAMUS* consists of two types of detectors: proportional drift tubes (PDTs) for tracking (also used during Run I) and scintillator tiles for triggering and timing (introduced for Run II). There are three multi-layers (A, B and C, with A closest to the interaction region). Both the B and C multi-layers have three layers of PDTs, whereas the A multi-layer has four. There are scintillators in the A and C multi-layers. There is a region devoid of tracking in the WAMUS A multi-layer for $225° < \phi < 310°$ due to the calorimeter support structure.

The *FAMUS* (completely new for Run II) and has a similar structure consisting of mini drift tubes (MDTs) and scintillation pixels. The reason the FAMUS uses a different tracking technology is because of the higher rate of particles produced in the forward region. It is also arranged in three layers, with both MDTs and pixels in all layers. Because of the large size of the muon system, it is necessarily of course granularity in all layers.

The *toroid* magnet is described in more detail in Section 3.2.2 and provides a field sufficient to bend the trajectory of a muon through the system for momentum measurement.

3.2.8 Trigger and Data Acquisition System

In a $p\overline{p}$ colliding-beam experiment, only a few events in the millions of collisions per second are selected. As the total collision rate by far exceeds the rate at which events can be recorded (because of dead-time in the electronics) and processed (because of constraints on the cost of storage media and ability to analyze the data), most of the events are discarded. For the events that are recorded, a balance is maintained between different physics processes based on the research priorities of the collaboration.

This task of selecting the desired events is accomplished through the use of triggers. A trigger looks at the coarse detector information of one or several subsystems in an event and quickly decides whether to keep or reject it according to a specified criteria. The DØ trigger framework is organized into three main levels (L1, L2 and L3) of increasingly sophisticated event selection and therefore decreasing output rate (the rate is reduced from 1.7 MHz at the beginning down to a rate of 50 Hz for storage to tape). To reduce the rate further, a *prescale* factor can be applied to triggers. The prescale allows a set fraction of events that pass a trigger decision to propagate through the data acquisition chain. Prescale values may be changed during the course of a store based on instantaneous luminosity. Figure 3.7 shows a schematic diagram of the trigger and data acquisition system.

The *L1 trigger* is a hardware based system using simple algorithms implemented in Field Programmable Gate Arrays (FPGAs) operating on the raw data from a detector. Each individual trigger decision is sent to a so-called Level 1 "AND-OR" term. In total, there can be up to a maximum of 256 such terms which can be combined into 128 triggers. All of the data is processed in parallel. Since the rate of data acquisition exceeds the processing speed, events are stored in a buffer system. If an event fulfills a trigger criteria a L1 Accept decision is send out (on the order of 3.3 μs) at which point the event is either discarded or passed onto the L2 trigger. At level 1 there are typical dead-times of around

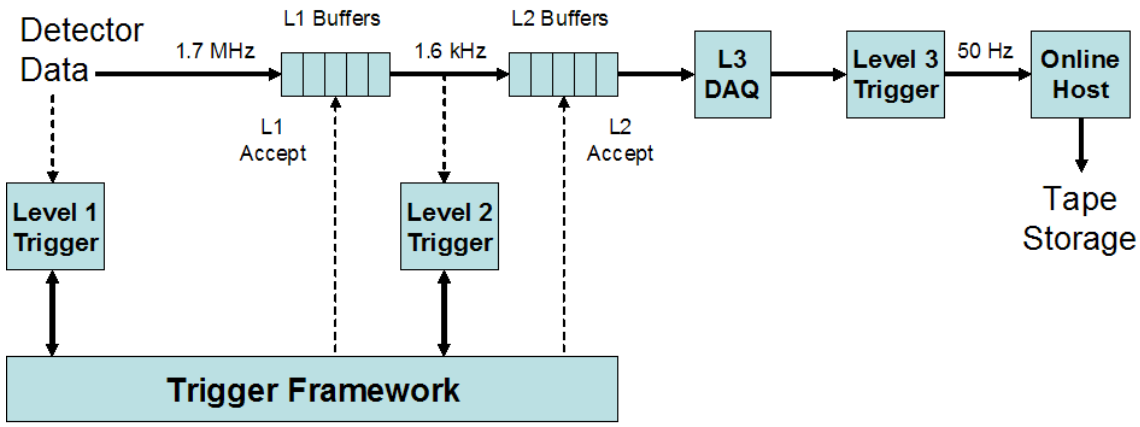

Figure 3.7 The DØ 3-level trigger scheme and typical trigger rates.

$1-5\%$ of the total running time while the entire detector is being read out. At L1, the rate is reduced from 1.7 MHz to about 1.6 kHz.

The *L2 trigger* can be used to apply further selection criteria and improve filtering and in its final stages can also combine the information from different subdetectors. It makes use of hardware logic-based cards as well as microprocessors in VME crates (500 MHz Alpha processors running Linux, VME bus and a custom-built "Magic Bus" interface for 320 MB/s data handling). The rate passed to level 2 from L1 still exceeds the processing speed, so L2 also makes use of a buffer system while the decision to accept or reject an event is made (occurs on the order of 100 μs). It an event is accepted by level 2, it is passed onto the L3/Data Acquisition System (*L3DAQ*). The rate is reduced from 1.6 kHz to about 800 Hz by level 2.

For the L3DAQ, data flows in parallel out of 63 VME readout crates, each corresponding to a section of a subdetector system or the trigger framework. Each crate is read out by a Single Board Computer (SBC). An SBC is powered by a 933 MHz Pentium-III processor with 128 MB of RAM. the information in one crate occupies about $1-20$ kB with a total event size of around 250 kB, and the L3DAQ system has a bandwidth of 250 MB/s. That data are moved out of the SBCs over an Ethernet network which trans-

fers them over the main switch via a 1 Gb/s optical fiber to the L3 farm. There are devices in place to ensure coordination of the L3DAQ components both functionally and in terms of time synchronization for the L3 farm.

At the *L3 farm*, the trigger combines and partially reconstructs the full data for each event that has passed the L1 and L2 decisions. The L3 farm contains software based triggers that run on a farm of Linux PCs. Each event passing L2 is analyzed by a different process which runs an independent instance of the L3 filtering software. Typically events take less than 100 ms to process. The farm nodes receive data fragments through the main switch. A farm node builds a complete event, reconstructs it and performs physics selection. Events that pass the final physics criteria are sent via the network to a collector machine where they are eventually written to tape for offline analysis at the rate of about 50 Hz.

CHAPTER 4

THE DØ FORWARD PROTON DETECTOR

The Forward Proton Detector (FPD) [91] is a new detector subsystem for DØ Run II. It can reconstruct protons and antiprotons that are scattered at small angles (on the order of 1 mrad) with respect to the beam and that escape detection by the central DØ detector because they pass down the beam pipe. A second experimental signature for selecting diffractive events is to reconstruct the scattered beam protons and antiprotons necessary if one wants to have direct access to the full kinematics of the event.

4.1 Forward Proton Detector Layout

The FPD consists of a series of nine momentum *spectrometers* that make use of existing accelerator magnets in conjunction with scintillating fiber *position detectors*. These are located along the beamline, $20 - 60$ m from the central DØ detector. In addition, to reject events with narrow jets passing down the beampipe, there are *veto counters* installed on either side of the DØ interaction point at roughly ± 6 m corresponding to the region $5.2 < |\eta_{det}| < 5.9$. They are used like the LM detectors in the determination of forward gaps in an event for the trigger. The position detectors operate a few millimeters away from the beam and need to be moved transversely away during injection of the beam into the accelerator and at the end of a store. Special stainless steel containers, known as *Roman pots* (RP), house the position detectors. This allows the detectors to operate close to the beam, but outside of the accelerator's ultra-high vacuum (UHV) of 10^{-10} Torr. The scattered p or $\overline{p}$ traverses a 200 μm thick steel window at the entrance

and exit of each pot. The motion of the pots is controlled remotely, and they are moved back close to the beam after stable beam is achieved.

The Roman pots are housed in stainless steel structures called *castles*. The full FPD consists of 18 Roman pots arranged in six castles as shown in Fig. 4.1. The castles are located at various distances relative to the DØ interaction point at locations that do not interfere with accelerator operations. Two castles are located downstream of the low-beta quadrupole magnets on the **outgoing** proton side (P1 and P2) and two castles are located upstream of the low-beta quadrupole magnets on the **outgoing** antiproton side (A1 and A2). Each so-called *quadrupole castle* has four arms, each housing a Roman pot arranged to cover most of the area around the beam. Each pot is labeled as Up (U), Down (D), In (I) or Out (O) based on its position relative to the center of the beam pipe. In addition, two castles (D1 and D2) are located on the outgoing antiproton side upstream of the dipole magnets. Each of the *dipole castles* contain only one Roman pot on the inside arc of the Tevatron beam line (side closest to the center of the Tevatron ring).

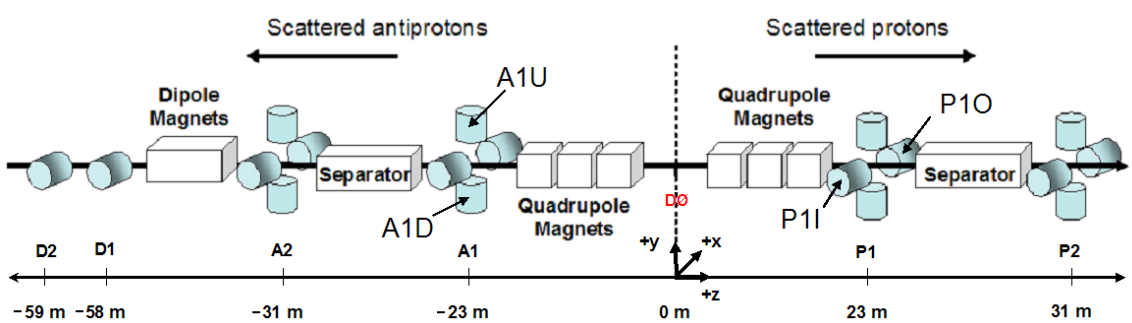

Figure 4.1 Schematic layout of the FPD system.

A castle (shown in Fig. 4.2) is made of stainless steel and specially cleaned before installation because of the UHV environment in which it operates. A set of hot cathode-

and convection Pirani-style sensors[1] continuously monitor the vacuum inside a chamber. Each castle also has an associated ion pump to help maintain the UHV.

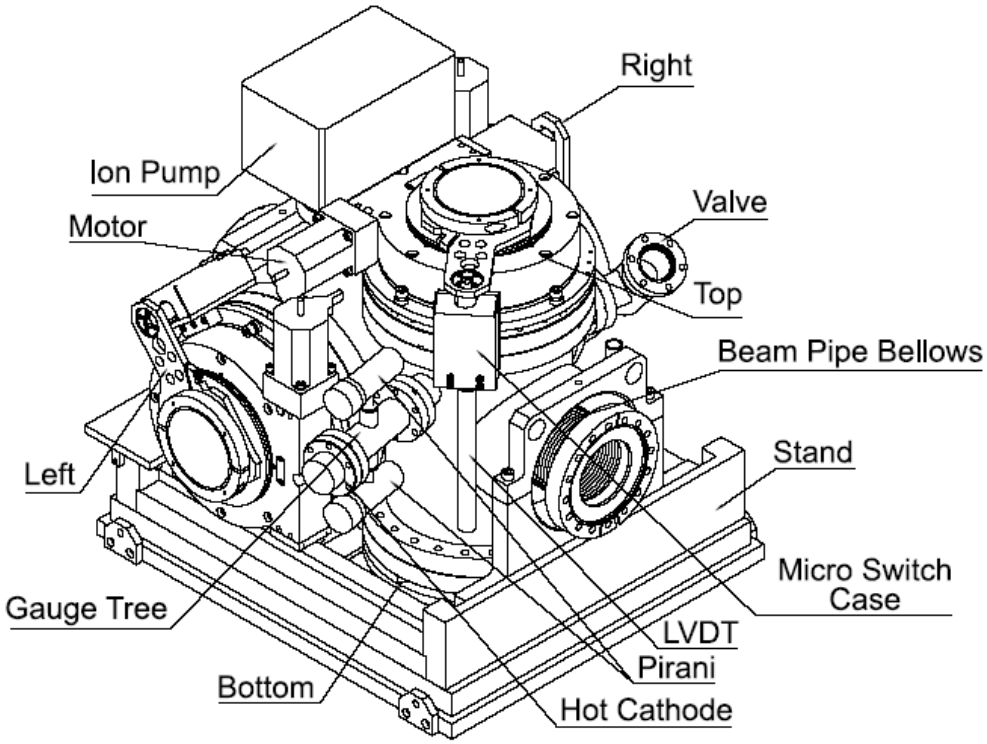

Figure 4.2 Diagram of an FPD castle.

The castle is mounted on a stand whose position can be adjusted in all directions over a range of ±15 mm and with an accuracy of 0.1 mm. The castles were aligned when originally installed such that they were centered with respect to the beamline. Each pot is connected to a driving system that makes it possible to remotely move it perpendicular to the beam. The motion system operates a step motor and a set of reduction gears

[1]Pirani-style gauges use a measure of the current needed to keep a wire at a constant temperature to determine the pressure of a gas since thermal conductivity is linear with density (pressure) below 1 Torr and are accurate down to around 10^{-3} Torr. Hot cathode-style gauges emit electrons into the vacuum where they collide with gas molecules to create ions. These ions are collected and the current is proportional to the gas density and are accurate down to around 10^{-10} Torr [92].

resulting in movement with a precision of approximately 8 μm per half turn of the step motor. A system of cylindrical and conical bearings can be used to adjust pot alignment and a linear variable differential transformer[2] (LVDT) monitors the pot position. A steel bellows makes it possible to move the pot without affecting the vacuum.

4.2 FPD Position Detectors

The FPD position detector technology was motivated by the following needs:

- Position resolution of approximately 100 μm (dictated by a comparable uncertainty in beam position);
- High efficiency;
- Modest radiation hardness (expected dose of 0.03 MRad/year);
- High rate capability;
- High background rejection;
- Small dead area close to the beam (acceptance driven by distance from beam).

As illustrated in Fig. 4.3, each detector consists of *channels* of 0.8 mm-thick, double-clad, square[3] scintillating fibers bundled in stacks of four parallel fibers forming a scintillating structure measuring 0.8×3.2 mm^2 in cross-section. A typical particle passing through an active element results in approximately 10 scintillation photons in the blue part of the visible spectrum with a peak emission wavelength of about 475 nm. The fibers are positioned in plastic frames which maintain both the position of the fibers and the relative alignment between layers. The channels are separated from each other by 250 μm thick plastic fins that reduce optical cross-talk between neighboring channels.

[2]An LVDT consists of three coils and a ferritic core. An oscillating signal is provided to the primary coil, and the position of the core controls how much of an induced field is produced in the secondary coils. The secondary coils are aligned in opposition, such that with the core in the central position, the sum of the output from the secondary coils is zero [93]. Since the output voltage is linear with the position of the core, the position of the pot can be deduced from the output voltage.

[3]The use of square fibers increases the light yield by about 20% with respect to round fibers.

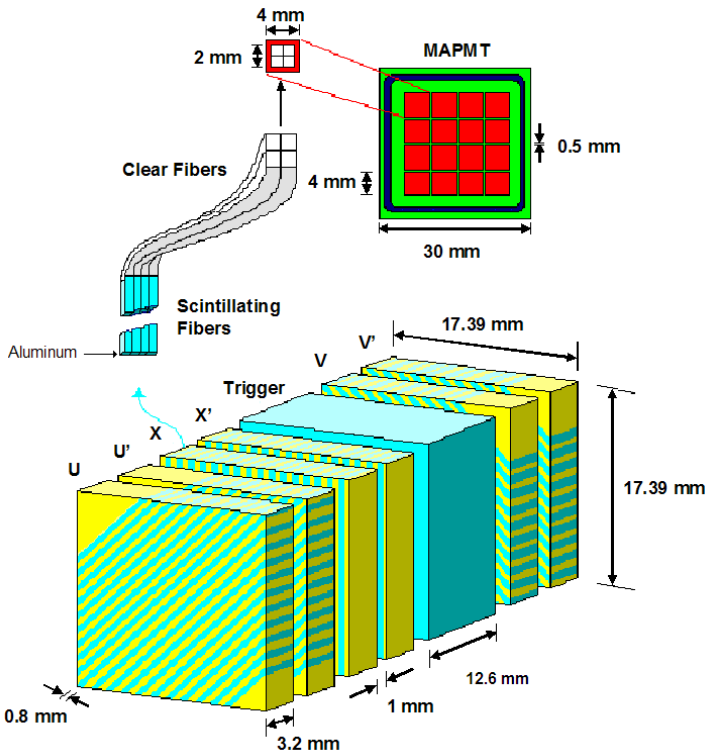

Figure 4.3 Schematic diagram of FPD position detectors and MAPMT.

One end of the active detector element is coated with an aluminum layer about 3 μm thick to increase light yield and the other end is spliced to a double-clad clear waveguide fiber of square cross-section which has the same dimensions as the active fiber. The fibers are first polished using an ice polishing method. They are then held in place under pressure while an intense light beam fuses the cladding of the two fibers together using the splicing machine shown in Fig. 4.4. This process minimizes discontinuities in the cladding, assures optimal optical connection and avoids a bulky region around the connection that often results with the typical shrink-tubing procedure.

Each detector consists of six *layers* (u, $u^{'}$, x, $x^{'}$, v, $v^{'}$) which are arranged in three *planes* (u, x and v). Each plane is made up of a "primed" and an "unprimed" layer with the primed layers being offset by two-thirds of a fiber width with respect to the unprimed

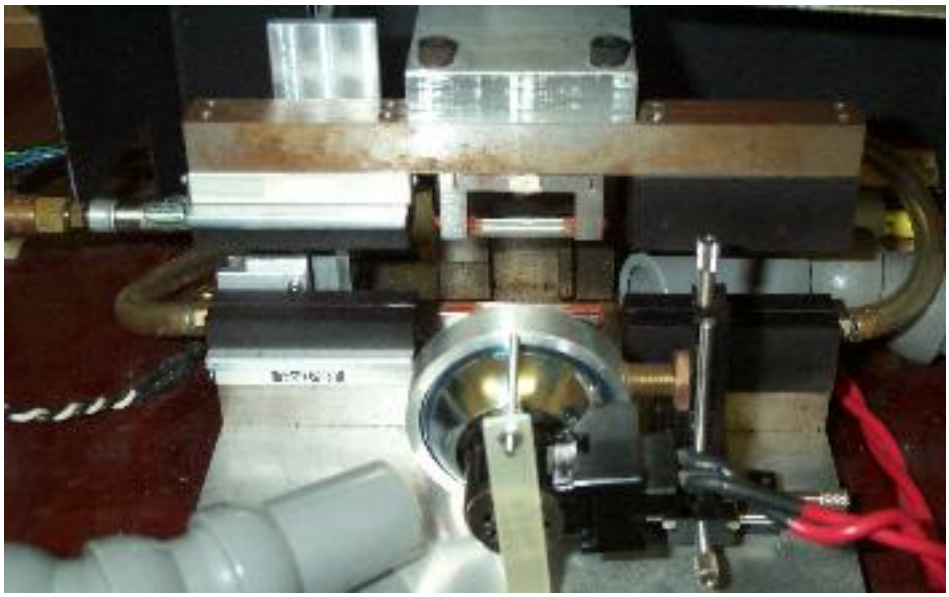

Figure 4.4 Picture of splicing machine used in production of FPD fibers.

layer. In each detector, there is also a trigger scintillator located between the x and v frames with an active area of approximately 2×2 cm^2. The three plastic frames that make up the planes are held together and aligned through the use of bolts through the u and v frames into the x-frame. The channels of the u, v and x planes are oriented at $\pm 45°$ and $90°$ with respect to the horizontal bottom of the detector. There are twenty channels in each layer of the u and v planes and sixteen channels in each of the x layers. Thus, there are 112 channels (each with four fibers) per detector giving a total of 2016 channels for the full system.

The clear waveguide fibers take the light of a single detector channel to one pixel of a 16-pixel multi-anode photomultiplier tube (MAPMT). There are seven MAPMTs in total for each detector. The clear fibers allow the tubes to be located away from the active area of the detector. The halo background, optical cross-talk, and light attenuation is expected to be small in these fibers. The clear fibers are held in a diamond polished plastic support (*cookie*) which maintains their position relative to the pixels of the MAPMT as

shown in Fig 4.5(a). The entire detector including cookies is mounted in an aluminum *cartridge base* that can slide down into a Roman pot, where it is held in place securely against the 200 μm thin window of the Roman pot tip through the use of long threaded rods as shown in Fig 4.5(b).

(a) (b)

Figure 4.5 Picture of (a) cookie and (b) cartridge base used in the FPD detector.

The seven MAPMTs and single (fast photomultiplier) trigger tube are housed in an aluminum *cartridge top* that can be placed over the cartridge base aligning the tubes over the cookies as shown in Fig. 4.6(b). The cartridge top is secured firmly against the base to provide good optical contact between the fibers and the MAPMTs.

(a) (b)

Figure 4.6 Picture of (a) MAPMT and (b) cartridge top used in the FPD detector.

The MAPMT signals are carried to Amplifier/Shaper (A/S) boards located nearby in the tunnel and the amplified signals are then propagated through 16-channel ribbon cables to the central DØ platform where they are processed by Transition Patch Panels (TPP) consisting of transformers and resistors that reduce the charge of the signal to a level that can be processed by the CFT electronics already described in Section 3.2.4. A Trigger Manager (TM) of the same type used by the muon system receives fiber information in and uses it to make a Level 1 trigger decision based on FPD tracks[4] (see Section 3.2.8). The trigger signal is not amplified but is sent directly to the luminosity monitor electronics already described in Section 3.2.6 for processing.

A picture of the fully installed dipole spectrometer used to collect data for this analysis is shown in Fig 4.7. The dipole spectrometer was the first to be installed and commissioned, becoming available early in 2003. In early 2004, the remaining quadrupole detectors were installed and are in the process of being commissioned now. For more details on detector assembly see Appendix A.

4.3 FPD Operations

The first step in the operations procedure is to establish operating positions for the individual pots. Due to the fact that beam conditions can change from store to store, four possible positions are determined for each spectrometer. At each pot location, there is a "sigma" value associated with the beam profile in both the x and y direction, σ_x and σ_y respectively. Detectors within a spectrometer are moved to matching sigma values to maximize diffractive acceptance. As the pot is moved closer to the beam (*i.e.* smaller sigma values), the singles rate measured by the detector can increase dramatically with small position increments. Ideally, a pot position is determined where the pot is barely within the halo profile (this is achieved with the dipole detectors). Insertion of

[4] A track is a pair of hits in the two detectors of a spectrometer.

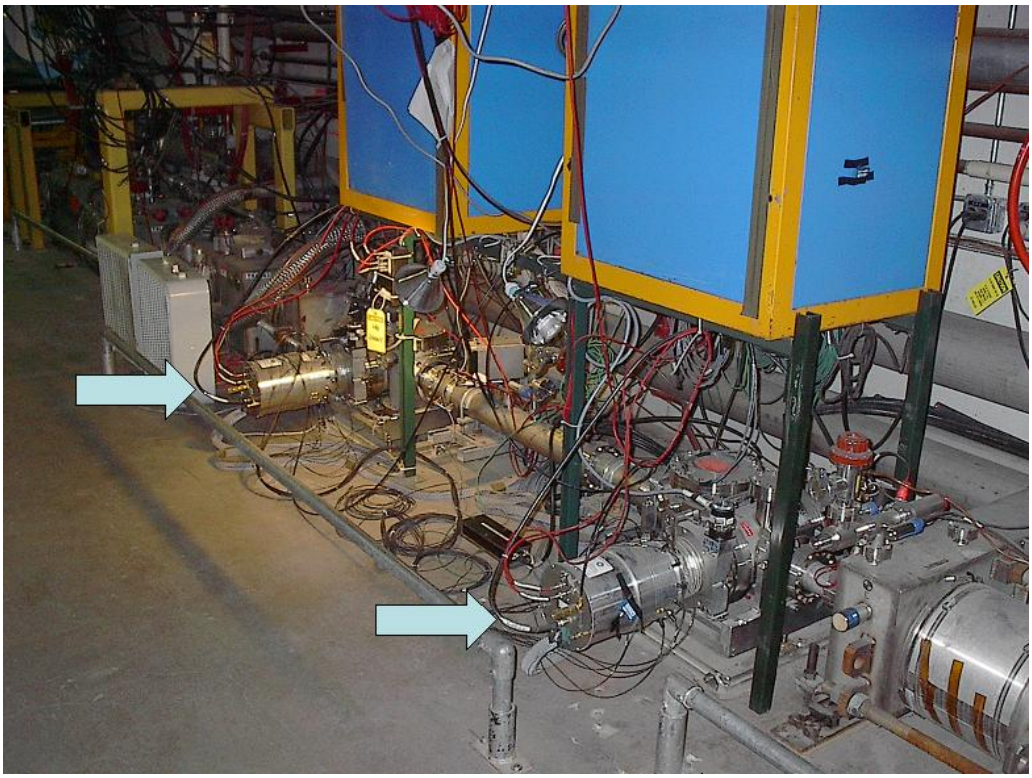

Figure 4.7 Picture of fully installed dipole spectrometer. The detector cartridges are the cylindrical structures (indicated by arrows) and the blue racks above them house the pot motion electronics and amplifiers.

the quadrupole pots increases the halo to a measurable limit in the luminosity systems at DØ and CDF. Final operating positions for these detectors are determined by the percentage increase measured in the central detectors and this limits the pot operating positions to a region prior to the exponential increase in the singles rates. Once the closest matched positions are determined for each spectrometer (green tables) the remaining three matched positions are just integral numbers of sigma further away from the beam (yellow, red and brown tables). For further information on how these positions are found as well as additional information on the detector operation, see Appendix B.

The pot motion system is monitored and controlled through a python program GUI communicating with each station through a 1553 controller connected to a *Rack*

Monitor (RM) at each castle [94]. Each RM is then connected to a Multiplexor (MUX), which allows a single RM to control the motion of up to 4 pots. Each pot in a castle has an Interface Board (IB) that receives signals from the MUX and translates a command to move to a particular position (entered in mm from home and desired speed in the control program) into the number of turns and direction necessary to complete the move. This information is then conveyed to a driver, which provides the necessary signals to the step motor. The driver is able to move the motors at two different speeds: fast speed corresponding to $6 - 8$ mm/minute, and slow speed corresponding to $1 - 2$ mm/minute.

Several systems provide monitoring information during operation. A Hall probe which uses magnets on the shaft of the motor determines the number of rotations and hence the distance moved by the pot. This value is calculated by the IB at the end of every movement. In addition, the LVDT continuously measures the position of the pot. Also, the trigger scintillator located in each detector provides a measure of the hit rate in each pot through a CAMAC (Computer Automated Monitor and Control) scaler system. LVDT positions, rates, and the motion status of each pot is updated every second and displayed in the control program. Pot positions and rates are also transferred to the Accelerator Division (AD) through the use of the ACNET (Accelerator Control NETwork) system [95].

In order for the drivers to be powered to enable pot motion, control switches in the DØ control room need to be activated. There is one switch for the proton (P) side pots and one for the antiproton (A) side pots. Manual activation of the switch provides +5 V to a relay in the control box that provides power to the drivers. In addition, the drivers of an individual castle need to be activated in the control program. Unless both of these controls are activated, the pots are unable to move since the drivers are disabled. In a situation where the software is unresponsive, there is a manual "Emergency Line" switch that can be turned on. This provides both the "+5 V control" signal and the "driver on"

signal and issues a command directly to the hardware to return all pots home at high speed.

There are several safeguards and monitoring programs to protect against various possible hardware failures:

- The closest (to the beam) allowed operating position for each individual pot is set as a parameter in the pot control program. Any attempt to enter a position beyond this "software limit" will not be allowed by the program; this protects against any attempt to send a pot to a position closer than its minimum allowed position.
- There is also a position-watcher feature in the control program that monitors the LVDT value and compares it to the desired position. If the desired direction of motion is towards the beam (IN) and the LVDT value exceeds the desired position, a stop command is issued. This safeguard protects against a possible hardware failure that might otherwise allow a pot to go beyond the desired position. In addition, if the LVDT readback indicates the pot is moving in the direction opposite to the desired direction, pot motion is disabled.
- There is an independent rate-watcher program that monitors the singles rates of each pot. It is primarily intended to protect FPD equipment against high rates from beam-loss spikes, but also gives warnings if there are abnormally high rates during pot insertion. This program runs on a different online node than the pot motion program. If the singles rate in any pot exceeds 350 kHz, a warning window is displayed. If the singles rate exceeds 420 kHz, the HV to the MAPMTs is disabled, and on-screen and verbal alarms are issued. HV to the trigger tubes is retained to monitor rates. Finally, if the rate exceeds 500 kHz, pot motion is disabled. This program runs continuously and can restart itself automatically.
- In the case of any anomalous occurrence during pot motion, the control line switches can be turned off, freezing the pots in place.

With all of these safeguards and monitoring tools available, the pots are inserted during each store once the integrated luminosity reaches 40×10^{30} cm^{-2}s^{-1} (to minimize the contribution from multiple interactions). Pots are inserted in groups of 2 (dipoles) or 4 (quadrupoles). The pot insertion positions are determined on a store-by-store basis based on the measurements of singles rates and halos. Information is recorded for each insertion in a database. This information is used later in the analysis. At the end of each store, the pots are retracted using an "all pots home" command and the HV channels for the FPD system are all switched off, thus placing the FPD in standby mode prior to the dumping of the beam and injection of new beam.

CHAPTER 5

OBJECT IDENTIFICATION

The first step towards using the information from the DØ detector as described in Chapter 3 and 4 is reconstructing the data. During the reconstruction step, the various detector channels are processed through algorithms to enable the identification of objects (*e.g.* jets, protons, muons). For this analysis, the two objects that are necessary are jets and protons.

5.1 Jet Identification

As introduced in Section 2.3.1.1, jets are the final states observed when a parton in a hadron is ejected through a collision. A jet can be described at various levels as shown in Fig. 5.1. In fixed order perturbative QCD, jets are treated as *parton jets*. These partons then undergo hadronization and become *particle jets*. Finally, the jets are detected in a detector as *detector jets*. Theoretical predictions pertain to parton jets, while detector jets are observed experimentally. Particle jets are not well handled in the theory and must be modeled mathematically. It is imperative that jet properties (*e.g.* energy and direction) are strongly correlated between the various levels allowing a detector jet to be compared to the parton or particle jet. The information that follows is drawn primarily from references [84, 85].

Since jets are not fundamental objects, they need to be modeled. This is done through the use of a *jet algorithm*. The most important feature of such an algorithm is how well it preserves the correlations between jet properties at the different levels. It

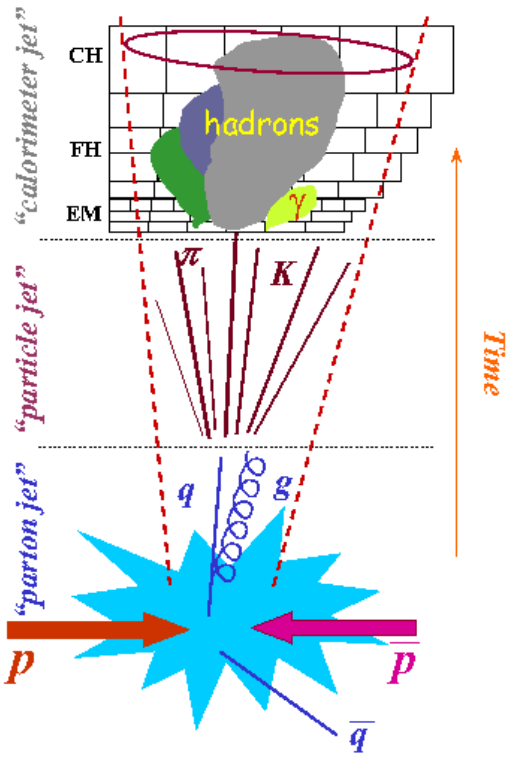

Figure 5.1 Schematic illustration of different levels of a jet [84].

should be independent of the actual detector parameters (*e.g.* calorimeter cell size) and should be insensitive to soft and collinear emission of partons. There are two typical types of algorithms: *cone* and $k_\perp$.

Cone algorithms are based on a geometrical definition of jets. A jet is defined as a group of partons (particles or towers) within a particular cone of radius R. The distance of a particle from the center of the cone (*i.e.* the jet direction) is found using Equation 3.3 and must be less than the cone radius. The particular value of R to be used is an arbitrary parameter of the algorithm. For this analysis, a standard value of $R = 0.7$ is used. It roughly corresponds to the observed size of particle sprays induced by hard scattered partons. Also, this value of R exhibits the smallest dependence on renormalization and factorization scales in the various theoretical predictions.

A prescription is applied to the detector information from which the jet properties are calculated depending on an algorithm known as the *recombination scheme*. The most commonly used scheme is the *Snowmass accord* [96]:

$$E_T^{jet} = \sum_i E_{Ti}, \quad \eta^{jet} = \frac{\sum_i \eta_i E_{Ti}}{\sum_i E_{Ti}}, \quad \phi^{jet} = \frac{\sum_i \phi_i E_{Ti}}{\sum_i E_{Ti}}, \tag{5.1}$$

where i consists of the towers within the cone. Jets in this scheme are by definition massless. This scheme was used as the Run I jet definition (and is still used in the jet triggers). For Run II, a different scheme (the *E-scheme*) is applied for offline analysis as described in Section 5.1.1.

While cone algorithms have a simple geometrical interpretation, they are not without complications. These arise when jets start to overlap, requiring a jet merging and splitting procedure to avoid effects of soft and collinear singularities. Also, such a procedure needs to be modeled in theoretical calculations leading to the ad-hoc parameter R_{sep} (specifying the maximum separation between partons for them to be included in the same jet) applied to jet algorithms at the parton level [97].

A second major class of jet algorithms are called $k_\perp$*-algorithm*. These algorithms are motivated by the characteristics of the perturbative development of the parton shower [98, 99, 100]. Partons in a jet are typically radiated along the direction of the original parton or they are soft. A typical $k_\perp$-algorithm orders the partons such that the distance between soft and collinear particles is small. The algorithm is iterative in that at each step particles that are sufficiently close to each other are combined into a single "particle". The iteration stops when the distance between the closest particles is greater than some value D[1]. Each remaining unclustered "particle" is defined as a jet. Such jets do not have a fixed geometric shape, and their size is driven by the parameter D. This type of

[1]Some $k_\perp$-algorithms don't have such a parameter and instead require a fixed number of jets in the final state and the iteration continues until that number of jets is achieved.

algorithm does not suffer from the theoretical problems of the cone algorithms as they are by construction infrared and collinear safe and every particle is uniquely assigned to a jet.

5.1.1 Improved Legacy Cone Algorithm

The algorithm used by DØ in Run II is a cone algorithm known as the Improved Legacy Cone Algorithm (ILCA). It is similar to the one used for Run I, but with a few important changes that improve the behavior of the algorithm on the parton level. The E-scheme recombination is used (4-vector addition) where the jets maintain a mass, and additional starting seeds are used to ensure that all jets are reconstructed. These changes are based on the recommendations of the Run II jet physics group [101] and the Jet Definition Group Les Houches [102, 103].

Detector jets are formed from calorimeter pseudo-projective towers as shown in Fig 3.6. Cells within the tower that satisfy the T42 algorithm[2] and not identified as hot by the New Anomalous Deposit Algorithm (NADA)[3] are included in the recombination. The Lorentz 4-momentum, P^{μ}_{tower}, assigned to the tower is computed as the sum of the 4-momenta of the associated cells:

$$P^{\mu}_{tower} \equiv (E_{tower}, \mathbf{p}_{tower}) = \sum_{cell} P^{\mu}_{cell}, \tag{5.2}$$

where the cell 4-momentum, P^{μ}_{cell}, is determined from the measured cell energy E_{cell} and the direction, $\hat{\mathbf{n}}_{cell}$, that points from the primary vertex of the interaction to the cell. The

[2]Cells that are 4σ above pedestal are kept, as well as cells between 2σ and 4σ as long as they neighbor a 4σ cell. Negative energies (which can occur due to the baseline subtraction used by the Calorimeter) are rejected [104, 105].

[3]Isolated cells on an event by event basis that are found to have energy much higher than some threshold above neighbor cells are considered spurious noise cells and are not included in any calorimeter analysis [106, 107].

jet 4-momentum, P^{μ}_{jet}, is then just the sum of the 4-momenta of the associated towers,

$$P^{\mu}_{jet} \equiv (E_{jet}, \mathbf{p}_{jet}) = \sum_{tower} P^{\mu}_{tower}, \tag{5.3}$$

This recombination scheme fully specifies the jet 4-momentum (energy and direction). Since the jets are not massless, jet rapidity, y, as defined in equation 3.1, is not the same as pseudorapidity, η, as defined in equation 3.2. The reasons for choosing this scheme for Run II over the old Snowmass scheme is its simpler, 4-vector form and the fact that it satisfies *boundary stability* conditions[4].

The Run II cone algorithm is an iterative jet definition procedure that can be described as follows:

1. Calorimeter towers with transverse energy bigger than $E_T^{seed} = 0.5$ GeV are starting "seeds" of the algorithm.
2. A small cone of radius, $R = 0.3$, is drawn around the seed in $\phi \times y$ space (replacing η with y in Eq. 3.3). All positive towers within the cone form a seed protojet.
3. The seed protojet 4-momentum is calculated according to Eq. 5.3. A new cone is drawn around the new direction and the towers within the new cone are used to calculate the new direction of the seed protojet, which is compared to the direction of the old seed protojet. Once the distance between the new seed protojet and the old seed protojet becomes sufficiently small (10^{-3}), the seed protojet is deemed "stable" and is moved to the pre-protojet list, otherwise the new seed protojet replaces the old seed protojet and the iteration continues. This process continues until all seed protojets become stable or a maximum number of iterations (currently 50) is performed. Stable seed protojets with "identical" directions (within 10^{-6}) are treated as one pre-protojet.

[4]Boundary stability means that jet kinematic boundaries are independent of the details of the final state configuration.

4. Midpoints between final pre-protojet pairs are used as additional seeds. The midpoint position is defined as the p_T-weighted average of the 4-momenta contributing to the midpoint. Only pre-protojets within $2R$ of each other are considered since they have the possibility of overlap. Stable positions for the midpoint seeds are found as in step 3 and any new, unique midpoint seed protojets are added to the pre-protojet list.
5. The final list of pre-protojets serves as the starting points for finding stable jet directions. The same iterative procedure as step 3 is applied for the desired cone radius R (for this analysis 0.7), summing over the pre-protojets. Stable cones are called *protojets*. Stable protojets with identical directions are treated as a single protojet.
6. The final protojets are ordered in transverse momentum. The protojet with the highest p_T that overlaps with another protojet is identified. The two protojets are *merged* if they share more than some fraction f of energy (50% for this analysis) of transverse momentum of the softer protojet, otherwise they are *split*. New merged protojets contain all of the towers from both protojets and no longer have a cone shape. When split, every shared tower is assigned to the closest protojet. The 4-momenta of merged or split protojets is recalculated according to Eq. 5.3. A new protojet list is ordered and the procedure is repeated until no overlapping jets remain.
7. Protojets with transverse momentum below 8 GeV are removed from the list of protojets.
8. Any remaining protojets become the final list of jets.

Employing seed towers rather than using all towers as starting points for jet finding speeds up the algorithm and is essential for jet reconstruction to occur in an acceptable time. However, the combination of seeds and the split/merge procedure introduces

collinear and infrared sensitivities (also an undesirable feature of the Run I algorithm). As illustrated in Fig. 5.2, a soft gluon radiated between the two partons with a transverse energy just above the seed threshold will form an additional jet that includes the other two partons, thus resulting in a single found jet in the final state (Fig. 5.2(b)) rather than the two that should be reconstructed (Fig. 5.2(a)). Therefore, the final number of jets is sensitive to soft gluon emission above threshold.

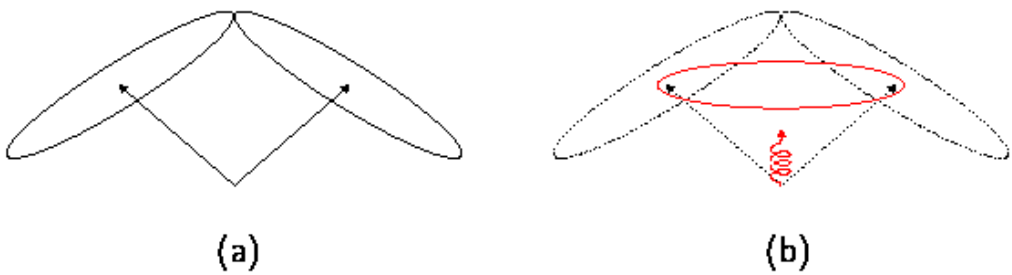

Figure 5.2 Illustration of infrared sensitivity of cone algorithm with: (a) two jets in final state with well separated partons, (b) one jet in final state if additional soft gluon emitted between partons with transverse energy above threshold [84].

The best solution would be to use every single calorimeter tower as a seed were it not for reconstruction speed issues. Since the number of jets is sensitive to the emission between jets, the midpoint seeds provide a compromise that results in the Run II algorithm having a smaller sensitivity to the infrared radiation [101], providing results similar to a seedless algorithm, but without a significant penalty in speed.

5.1.2 Jet Energy Scale

Before jet data can be compared to theory, the jet energies as measured in the calorimeter must be corrected to the particle level (*i.e.* the original energy of the jets before entering the calorimeter). For a compensating calorimeter, the detector response does not depend on whether the jet shower is dominated by the electromagnetic or

hadronic part of the shower. Consequently, the response is Gaussian, meaning it can be characterized by a mean value and a width. Measuring jet cross-sections requires that the response needs to be corrected as a function of both of these variables. For this analysis, only the mean needs to be corrected.

Detector response is corrected through the use of the *jet energy scale* (JES) algorithm. The DØ experiment formed a JES group to calculate the proper correction as a function of location and energy, and JES version 5.2 is used in this analysis [108].

The jet energy, E_{uncorr}, as reconstructed by the cone algorithm, is corrected to the particle level, E_{corr} according to the formula,

$$E_{corr} = \frac{E_{uncorr} - O(R, \eta)}{\rho(E_{uncorr}, \eta, R) \times S(R, E_{uncorr}, \eta)} \tag{5.4}$$

where η is the jet pseudorapidity, R is the cone size used, O is the *offset*, ρ is the *response* and S is the *showering* correction.

The offset is a correction for energy deposited in the cone that is not directly associated with the $p\overline{p}$ interaction itself (*e.g.* uranium noise, pile-up from previous beam crossings, and additional minimum bias interaction in current bream crossing). This correction depends on the jet's location in the calorimeter and the size of the jet. Currently, this correction is determined from the measured average transverse energy density deposited in the calorimeter during a special minimum bias run. This correction is most important for low-p_T jets.

The response correction is a measure of how the calorimeter responds to the individual particles in the jet. While the calorimeter is designed to be compensating, the response to jets is smaller than 1.0 because of non-linear calorimeter response to low energy particles and dead material in front of the calorimeter. The correction is deter-

mined from the transverse energy imbalance in photon+jet events. Since the photon's[5] energy can be measured with more precision in the EM part of the calorimeter than the jet's energy in the hadron part, the jet's energy can be deduced through conservation of momentum to find the desired correction.

Finally, the showering correction is a measure of the energy that radiates outside of the cone during the shower development in the detector (or energy that showers into the cone). Also, the solenoid field can change a particle's trajectory from its emitted angle outside (inside) of the jet's cone. This correction is determined from the jet profiles in the photon+jet sample by comparing the transverse momentum balance for varying cone radii; it is larger for smaller cones.

A representative sample of the JES corrections along with their errors (dominated by systematic uncertainties) is shown in in Fig. 5.3. For central jets (Fig. 5.3(a)), the correction drops from $\sim$ 30% for 50 GeV jets to $\sim$ 10% for 500 GeV jets. The overall relative uncertainty, obtained from adding the systematic and statistical error in quadrature, falls from about 17% for 20 GeV jets to 4% for 60 GeV jets. It has a plateau at 4% for jets over a wide range of energy, gradually increasing to 8% for 500 GeV jets (Fig. 5.3(b)). The η dependence of 50 GeV jets (Fig. 5.3(c)), it is flat at around 30% until the ICD region, where it grows to almost 50% before dropping to approximately 40% in the EC cryostat. The errors also grow in the ICD region as well as towards the forward regions (Fig. 5.3(d)).

5.2 Proton Identification

Proton identification refers to the measurement of protons or antiprotons. Particles passing through the position detectors of the FPD leave a signal in the fibers of the various

[5]In order to maximize statistics, any highly electromagnetic jet is deemed a photon for the purpose of this correction.

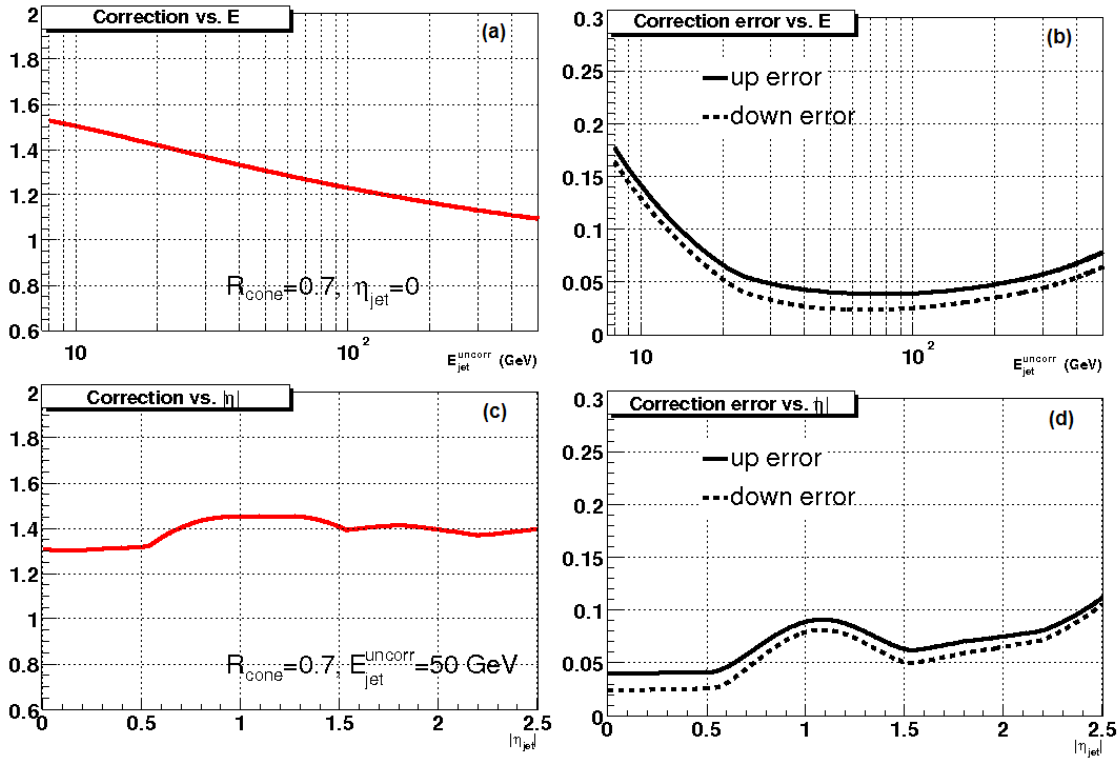

Figure 5.3 JES corrections for $R = 0.7$ jets for (a) central jets as a function of E_{uncorr} and (b) associated errors, (c) 50 GeV jets as a function of η and (d) associated fractional errors [108].

detector layers that can be reconstructed into a hit which can then be tracked through the magnetic and electric fields of the Tevatron lattice to determine the angle and momentum loss of the candidate diffracted particle at the interaction point. Reconstructed tracks that are consistent with forward particles (*i.e.* with trajectories making an angle of less than 1 mradians with respect to the z-axis due to the geometric acceptance of the position detectors) are considered as diffracted protons and provide a *tag* for diffractive events that are within the acceptance of the pot position relative to the beam and also give the ξ and t of the proton when calibrated. For this analysis we are concerned with diffracted antiprotons as detected in the dipole spectrometer of the Forward Proton Detector.

5.2.1 Hit Reconstruction

As described in Section 4.1, the Forward Proton Detector consists of scintillating fiber position detectors. The signals from the fibers are processed through the AFE electronics to provide ADC counts for each fiber. The first step of hit reconstruction is to determine which fibers have a real deposition of energy. This is accomplished by identifying those fibers with ADC counts in excess of 2.5σ above the pedestal value of the fiber channel. Because of the possibility of optical cross-talk between fibers in a layer at the frame[6] or at the MAPMT interface[7], there is an additional minimum discrimination value of 10 counts above the pedestal subtraction to determine which fibers are to be considered "ON". This discrimination value is determined on an MAPMT-by-MAPMT basis, and for the dipole detectors ranges from 25 to 55 counts.

To improve the hit resolution, each plane of fibers is split into two layers offset by 2/3 of a fiber width. This allows for the definition of a *segment* which is defined as a combination of fibers within a plane consistent with the passage of a particle as seen in Fig. 5.4. The first type of segment has only one fiber on in the plane (Fig. 5.4(a)). The second type has an "ON" fiber in each plane (Fig. 5.4(b)). This gives a total of 79 segments in the u and v planes and 63 segments in the x plane. Each segment has a width of 0.27 mm, giving a theoretical hit resolution of $270\mu\text{m}/\sqrt{12} \sim 80\mu\text{m}$. Since a diffractive event can only have one diffracted particle on a side, a multiplicity cut of five segments is applied to each plane (*i.e.* if more than three segments are on in any plane, the event cannot be tagged) in order to increase the processing speed and reject events with hits from noise or halo spray.

[6]If the angle of light within a fiber is sufficient, it is possible for light from one fiber to pass through the cladding into an adjacent fiber.

[7]Because of the way the MAPMT is constructed, light in one channel can leak to surrounding channels at the face of the tube. Studies of this cross-talk by shining light on a single channel while measuring the signal in surrounding channels found a cross-talk at about the 2.5% level. Including the possibility of misalignment between the cookie and the tube, this can increase to around 10%.

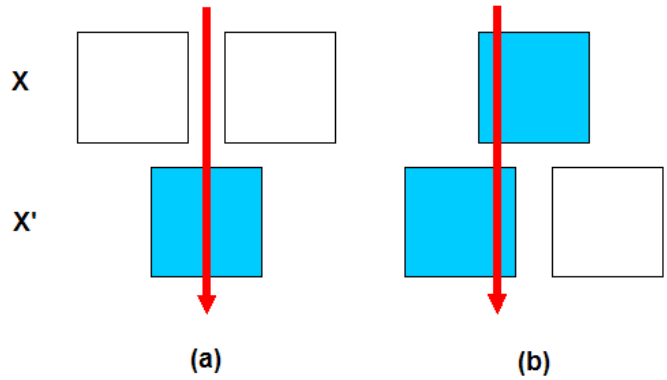

Figure 5.4 Examples of two types of FPD segments: (a) single fiber, (b) two fiber.

Once the struck segments have been determined, the combination of segments in different planes is used to define a *hit* where at least two segments intersect as shown in Fig. 5.5. The geometry of the center of each segment in its native detector coordinates (*i.e.* u_d, v_d, and x_d) is maintained. The construction of the detector defines two Cartesian planes, (x_d, y_d) and (v_d, u_d) which are related to each other through a simple rotation and shift as seen in the figure.

Two types of hits are possible. A "loose" hit requires two of the possible three segments. A "tight" hit requires all three segments overlap within a certain tolerance as shown in Fig. 5.5. Such a configuration helps remove unphysical hits and can reduce the effect of noise and stray particle hits. For this reason, the tight requirement is used in this analysis for the determination of tags, at the cost of some loss in efficiency.

For the tight requirement, the u and v segments are used to define the hit (expressed in (x_d, y_d) coordinates) and the x segment is used to validate the x coordinate. Because of the simple geometry of the detector construction, they are related by the equation:

$$\begin{pmatrix} x_d \\ y_d \end{pmatrix} = \begin{pmatrix} \cos\theta & -\sin\theta \\ \sin\theta & \cos\theta \end{pmatrix} \times \begin{pmatrix} v_d \\ u_d \end{pmatrix} + \begin{pmatrix} +8.695 \\ -8.695 \end{pmatrix}, \tag{5.5}$$

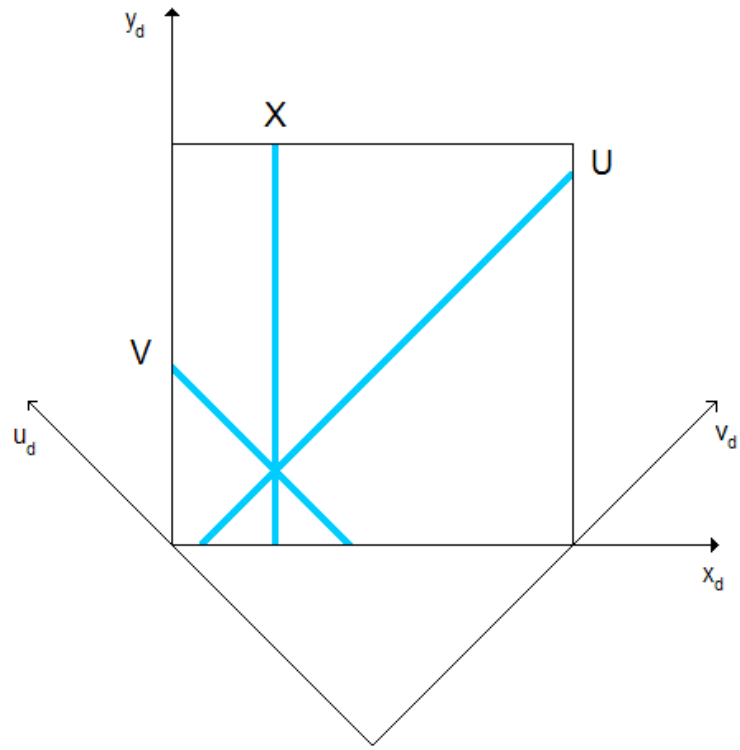

Figure 5.5 Example of a segment combination giving an FPD hit. The two coordinate systems used are also displayed.

where $\theta = 45°$. By looking at the difference between the two methods of finding the x_d coordinate (x_d from $u - v$ overlap versus x_d from the struck x segment), a measure of the actual hit resolution is available as seen in Fig. 5.6 which provides a value of 134 μm for a typical detector.

The relative alignment of the planes within a position detector is studied using data and detailed further in Appendix A. Because of the way the detectors are assembled, each detector will have different offsets in the relative positions of the u and v frames relative to the x frame compared to the ideal case. If such an offset is present, it is clearly seen in a hit resolution plot via an offset in the mean of the resolution. Such offsets are accounted for in the geometry files used during hit reconstruction which give the positions of the centers of the segments within the native coordinates relative to the x

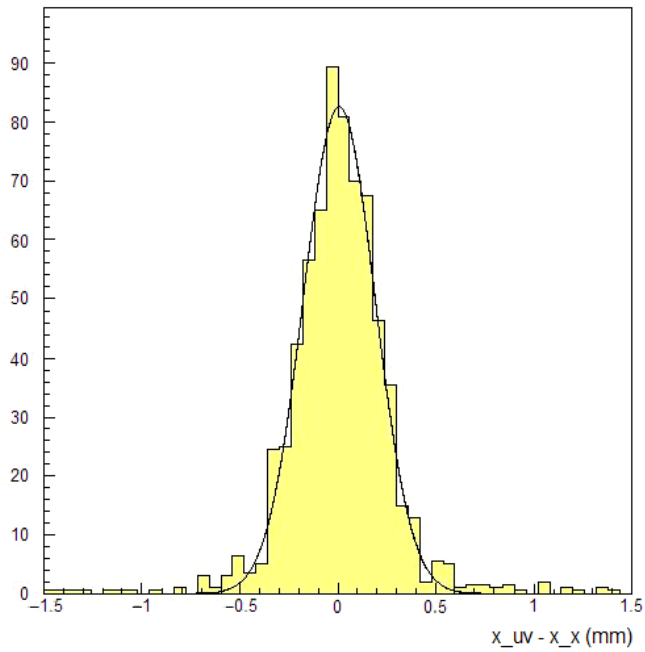

Figure 5.6 Hit resolution of an FPD detector by comparing x_d-coordinate from u- and v-segments to x_d-coordinate from x-segment (from data).

plane as shown in Fig. 5.5. It is also possible to find relative offsets between layers within a plane by looking at segment occupancy plots, allowing for corrections in segment sizes.

A *prototrack* requires a good hit in each detector of a spectrometer. For a particle passing through both detectors, a correlation between the hit coordinates in each detector is expected. Figures 5.7(b) and (c) show these correlations for the x_d and y_d coordinates respectively.

For the dipole spectrometer, because of its location in the Tevatron lattice, at the time a diffracted antiproton might be passing through the detector after an interaction there is also the possibility of outlying halo particles from the next incoming proton bunch to pass through the detector during the AFE integration window. However, because of the action of the dipole magnets on a diffracted particle that has lost a small fraction of its momentum, it is possible to tell the difference between these two types of particles.

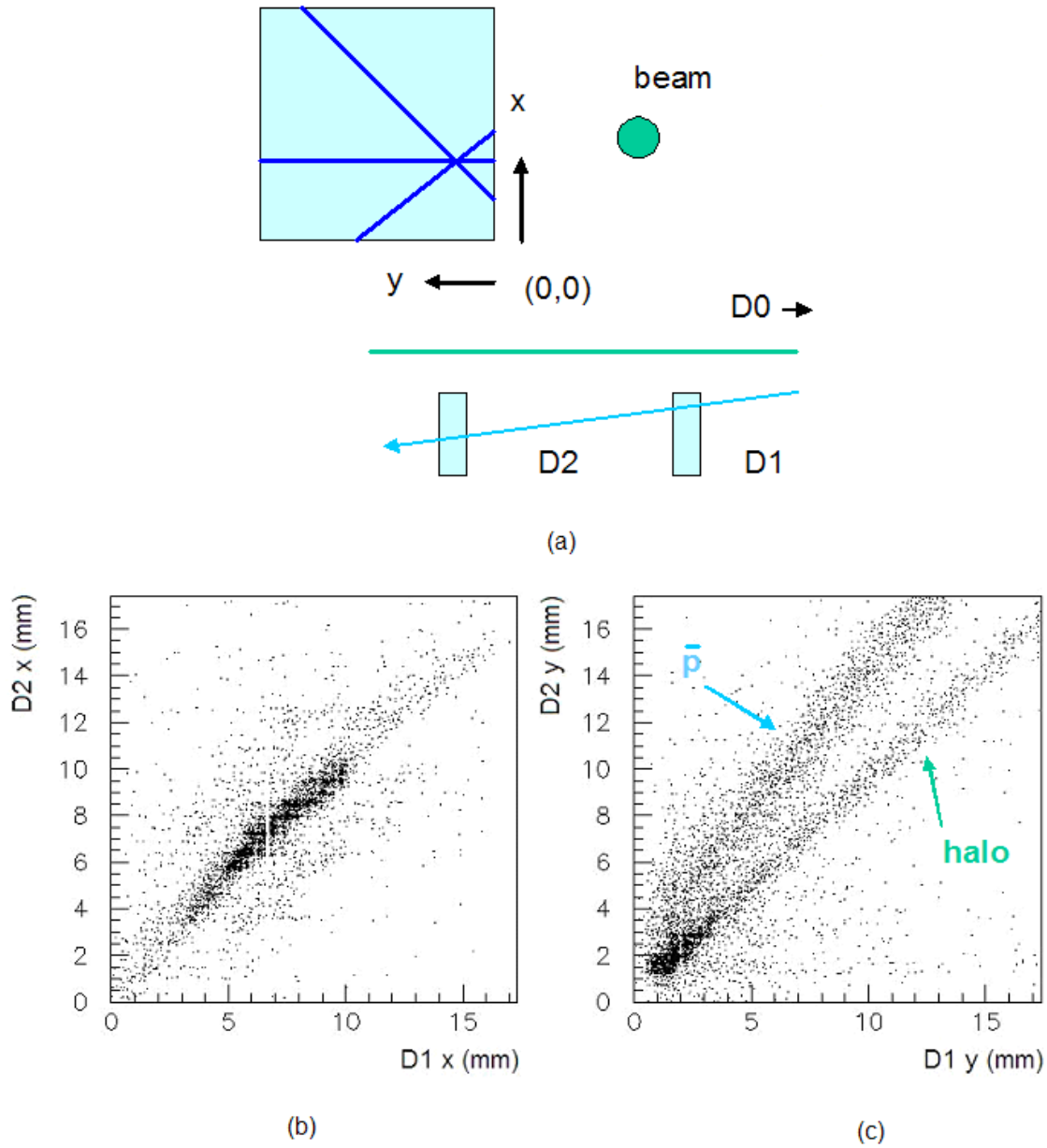

Figure 5.7 Hit comparison between detectors in the dipole spectrometer with (a) schematic layout of the detectors showing particle trajectories, (b) comparison of x_d between detectors, (c) comparison of y_d between detectors showing different trajectories for diffracted $\overline{p}$ and halo particles.

As shown in Fig. 5.7(a), the dipole detectors are on the inside of the Tevatron ring. An antiproton that has lost a small fraction of its momentum will be preferentially bent

further than the beam halo particles, therefore making a significant angle as it passes through the spectrometer. A halo particle is not expected to exhibit this behavior. As shown in Fig. 5.7(c), the larger angle is exhibited in the upper band of the y_d correlation, while the lower band has the expected behavior of halo particles. By requiring hits to be correlated in the upper y-band, we are preferentially selecting possible diffracted antiprotons to further process through the tracking code as well as once again discriminating against "fake" hits that are not consistent with in-time antiprotons passing through the detectors.

Before passing a prototrack on to the tracking code, it is necessary to transform the detector coordinates into beam coordinates (standard x and y as described in Section 3.2.1). During the alignment process, the location of the center of each pot is measured relative to the center of the beam pipe as well as the position of the bottom of the pot in the home position. The position of the active area of the position detector is known relative to the center of the pot and therefore relative to the beampipe. The final step is to determine the location of the beam relative to the center of the beampipe and then, through a simple translation and rotation, convert from one coordinate system to the other.

Relative alignments between detectors within a spectrometer can also be studied using data. Assuming ideal alignment, a simple Monte Carlo propagates particles from the interaction point to the detectors allowing the production of expected correlations. Comparing these correlations to those provided in the data gives access to relative alignments which can then be accounted for in the translation of detector coordinates to beam coordinates.

5.2.2 Proton Tracking

Prototracks are processed through the Tevatron lattice as the final step of determining a diffractive tag and calculating the appropriate ξ and t for the particle as defined in Equations 2.2 and 2.19. This is accomplished by measuring the hit location in the two detectors of a spectrometer, (x_1, y_1) and (x_2, y_2), and finding the physical parameters at the IP region by reverse propagating the track through the Tevatron lattice. The procedure used to accomplish this is summarized here and presented in more detail in Ref. [109].

5.2.2.1 Tevatron Lattice Propagation

A particle that is diffracted at the IP, has a small angle relative to the beam and small change in momentum relative to the beam particles. As the particle propagates through the Tevatron lattice elements, depending on their nature (straight or bending), its trajectory will be changed. The trajectory can be tracked through each element if the phase variables are known at the start of the element (edge closest to IP):

$$\Omega_i = (x, y, \theta_x, \theta y), \tag{5.6}$$

where $\theta_x = dx/dz$ and $\theta_y = dy/dz$ are the slopes in mrad and the positions are in mm relative to the beam. As a particle traverses the element, a translation matrix allows the phase variables to be transformed into their final values according to:

$$\Omega_f = M \times \Omega_i + b, \tag{5.7}$$

where the M and b are determined by the type of element. The description that follows is for a particle traveling to the dipole spectrometer.

First there are various straight elements between each bending element. For a straight element of length L, the appropriate transform equation is:

$$\begin{pmatrix} x \\ y \\ \theta_x \\ \theta_y \end{pmatrix}_f = \begin{pmatrix} 1 & 0 & L & 0 \\ 0 & 1 & 0 & L \\ 0 & 0 & 1 & 0 \\ 0 & 0 & 0 & 1 \end{pmatrix} \times \begin{pmatrix} x \\ y \\ \theta_x \\ \theta_y \end{pmatrix}_i + \begin{pmatrix} 0 \\ 0 \\ 0 \\ 0 \end{pmatrix}, \tag{5.8}$$

The next type of element is the quadrupole magnet which focuses the beam in one direction while defocusing in the other direction. A triplet of quadrupole magnets comprised of focusing (F) and defocusing (D) magnets (F, D, F for example) provides focusing in both directions. The appropriate transport equation is:

$$\begin{pmatrix} x \\ y \\ \theta_x \\ \theta_y \end{pmatrix}_f = M_{F,D} \times \begin{pmatrix} x \\ y \\ \theta_x \\ \theta_y \end{pmatrix}_i + \begin{pmatrix} 0 \\ 0 \\ 0 \\ 0 \end{pmatrix}, \tag{5.9}$$

where the matrix for a quadrupole magnet focusing in the horizontal plane is:

$$M_F = \begin{pmatrix} \cos(L\sqrt{k}) & 0 & \frac{\sin(L\sqrt{k})}{\sqrt{k}} & 0 \\ 0 & \cosh(L\sqrt{k}) & 0 & \frac{\sinh(L\sqrt{k})}{\sqrt{k}} \\ -\sqrt{k}\sin(L\sqrt{k}) & 0 & \cos(L\sqrt{k}) & 0 \\ 0 & \sqrt{k}\sinh(L\sqrt{k}) & 0 & \cosh(L\sqrt{k}) \end{pmatrix}, \tag{5.10}$$

and for a quadrupole magnet defocusing in the horizontal plane,

$$M_D = \begin{pmatrix} \cosh(L\sqrt{k}) & 0 & \frac{\sinh(L\sqrt{k})}{\sqrt{k}} & 0 \\ 0 & \cos(L\sqrt{k}) & 0 & \frac{\sin(L\sqrt{k})}{\sqrt{k}} \\ \sqrt{k}\sinh(L\sqrt{k}) & 0 & \cosh(L\sqrt{k}) & 0 \\ 0 & -\sqrt{k}\sin(L\sqrt{k}) & 0 & \cos(L\sqrt{k}) \end{pmatrix}. \tag{5.11}$$

The quadrupole coefficient k depends on the particle momentum (expressed as $1-\xi$), the magnet field gradient G and the magnetic rigidity of the equilibrium momentum p_{beam}:

$$k = \frac{G[kG/cm]}{0.33356405 \cdot p_{beam} \cdot (1-\xi)}, \tag{5.12}$$

where the the beam momentum is 980 GeV and the field gradient is accessed through a database provided by the Accelerator Division based on the current in the magnet for a particular store[8].

After the quadrupoles, the particle passes through three electrostatic separators which provide horizontal (H) and vertical (V) electric fields. The particle passes through the separators in the order V, H, V. These fields control the separation between the p and $\overline{p}$ beams which travel around each other in a helical orbit around the Tevatron ring until they are focused at an interaction region. A separator can be modeled either as a dipole magnet with a magnetic field equivalent to the electric field or by a model where the separator is approximated by two drift spaces with an appropriate kick in between the drifts whose strength depends on the maximum electric field between the separator plates[9]. The second method is used in the reconstruction code since it is a good approximation that is easier and faster to calculate.

[8]Design value for a defocusing magnet is 135.16918 T/m and for a focusing magnet 137.04195 T/m.
[9]Design value for a horizontal field is 3.60 MV/m and a vertical field is 3.56 MV/m.

The final type of element is the dipole magnet which bends the beam in an approximately circular orbit as it traverses the ring. The antiproton passes through three dipole magnets prior to reaching the dipole detectors. The appropriate transform equation for this element is:

$$\begin{pmatrix} x \\ y \\ \theta_x \\ \theta_y \end{pmatrix}_f = \begin{pmatrix} \cos F_p & 0 & \frac{L \sin F_p}{F_p} & 0 \\ 0 & 1 & 0 & L \\ \frac{-F_p \sin F_p}{L} & 0 & \cos F_p & 0 \\ 0 & 0 & 0 & 1 \end{pmatrix} \times \begin{pmatrix} x \\ y \\ \theta_x \\ \theta_y \end{pmatrix}_i + \begin{pmatrix} \frac{10^3 \xi L (1 - \cos F_p)}{F_p} \\ 0 \\ \frac{2 \cdot 10^3 \xi \sin(F_p/2)}{\cos(F_p/2)} \\ 0 \end{pmatrix}, \tag{5.13}$$

with the dipole coefficient F_p given by,

$$F_p = -\frac{B[kG] \cdot L[m]}{33.356405 \cdot p_{beam}}, \tag{5.14}$$

where the design value for the field is $B = 43.35044$ kG.

5.2.2.2 Track Reconstruction Algorithm

It is possible to take the values of the position and slope as measured at the detector closest to the IP and propagate the particle backwards to the interaction region allowing the determination of ξ and t at the IP where:

$$|t| \approx (1 - \xi) p_{beam}^2 \theta^2, \tag{5.15}$$

with $\theta = \sqrt{\theta_x^2 + \theta_y^2}$ for small θ and $E_{beam} \gg m_p$. All of the previous lattice equations must be inverted since the positions at the detectors are known and we wish to derive the initial scattering angle and momentum at the IP.

Since the value of ξ is a part of the transport equation, an iterative procedure is used where a dummy value is first substituted into the equations. Using the coordinates of the hit in the spectrometer detector closest to the IP, (x_1, y_1) (in this case from D1I) and the coordinates of the hit in the further spectrometer detector, (x_2, y_2) (in this case from D2I), it is possible to calculate the slopes, $\theta_x = (x_2 - x_1)/L$ and $\theta_y = (y_2 - y_1)/L$, where L is the distance between detectors. With these values, it is possible to construct the phase vector, Ω_f which is reconstructed through all of the elements back to near the IP to find Ω_i. After each element, it is verified that the trajectory calculated remains within the constraints of the beampipe and if not, the prototrack is rejected. In the initial iterative step, a value of ξ_1 is used giving a result of (x_{O1}, y_{O1}). A second iterative step with a value of $\xi_2 = \xi_1 + 0.001$ is used giving a result of (x_{O2}, y_{O2}). These values are then used to find the first estimate for ξ_0 using a linear approximation between the x and y coordinates with the parameter ξ such that:

$$\xi_x = (\xi_2 - \xi_1) \times x_{O1}/\Delta x, \tag{5.16}$$

and

$$\xi_y = (\xi_2 - \xi_1) \times y_{O1}/\Delta y, \tag{5.17}$$

where $\Delta x = x_{O2} - x_{O1}$ and $\Delta y = y_{O2} - y_{O1}$ to give,

$$\xi_0 = (\xi_x + \xi_y)/2. \tag{5.18}$$

Any initial values of ξ can be used. However, because there is a linear approximation in this procedure, it is important to use a small step between the first and second values used so as not to invalidate the assumption (hence the use of step size 0.001). In addition, in order to avoid any indeterminacy through division by zero, a minimum value of 0.01

is applied to the quantities $|\Delta x|$ and $|\Delta y|$. In the case where either $|\Delta x|$ or $|\Delta y|$ is less than 0.01, the associated ξ_x or ξ_y is approximated as zero. This brings up an additional special case when ξ_x or ξ_y is zero, in which case, Equation 5.18 is replaced by:

$$\xi_0 = \xi_x + \xi_y. \tag{5.19}$$

In the first iterations, a value of $\xi_1 = 0.0$ is used (and therefore $\xi_2 = 0.001$). The value obtained for ξ_0 in these first two steps is not accurate enough (in some cases, depending on the value of t, the value can be off by as much as 10% as shown in Ref. [109]), so a second batch of iterative steps is performed using the same procedure just described with $\xi_1^{'} = \xi_0$ and $\xi_2^{'} = \xi_1^{'} + 0.001$ to arrive at a value $\xi_0^{'}$. The sum of the values from these two iterative steps provides the final reconstructed value ($\xi_{reco} = \xi_0 + \xi_0^{'}$). This final value of ξ_{reco} is then used in the reconstruction to arrive at the associated values of θ_x and θ_y at the interaction point and the value of t_{reco} is found according to equation 5.15. A probe particle of values ξ_{reco} and t_{reco} is then propagated from the IP through the lattice back to the detectors to verify that it satisfies all conditions of remaining within the beampipe and gives the expected hit coordinates at the detector before the prototrack is accepted as a track (tag).

To determine the reconstruction resolution, various probe particles with known initial values ξ_0 and t_0 are propagated from the interaction point $z = 0$ to the detector. The position at the detector is translated into which fibers would be fired. These fibers are then combined into segments and the segments into hits, then the reconstruction algorithm is applied to arrive at a ξ_{reco} and a t_{reco} as described. The difference in these two values $\Delta\xi = \xi_{reco} - \xi_0$ and $\Delta t = t_{reco} - t_0$ are the reconstruction resolutions for each variable. The results of this measurement for the dipole spectrometer are shown in Fig 5.8 with a theoretical resolution of 0.003 in ξ and 0.270 GeV^2 in t.

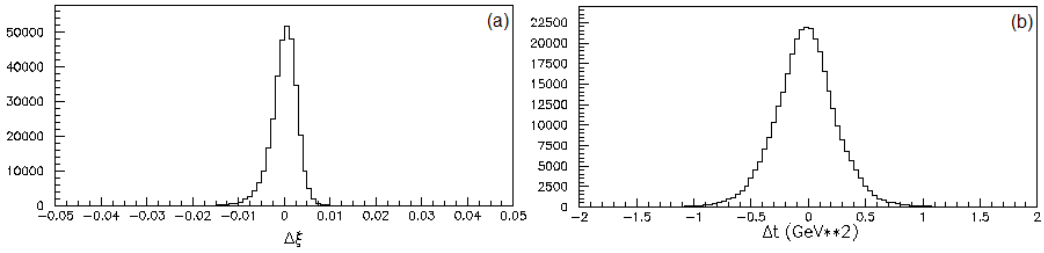

Figure 5.8 FPD reconstruction resolutions determined from MC for (a) ξ and (b) t for the dipole detector [110].

Any measurement of ξ and t is limited by the acceptance of the system. The geometric acceptance of the system is maximized by minimizing the distance between the position detectors and the beam. This distance is primarily limited by interaction with the beam halo which increases sharply as the pots are inserted closer to the beam. The acceptance is determined as a function of t and ξ. As shown in Fig. 5.9, for typical operation positions, for the dipole spectrometer the acceptance is highest for $|t| \lesssim 2$, $0.04 \lesssim \xi \lesssim 0.08$ and extends to $|t| \lesssim 4.5$, $0.018 \lesssim \xi \lesssim 0.085$ (coverage is incomplete).

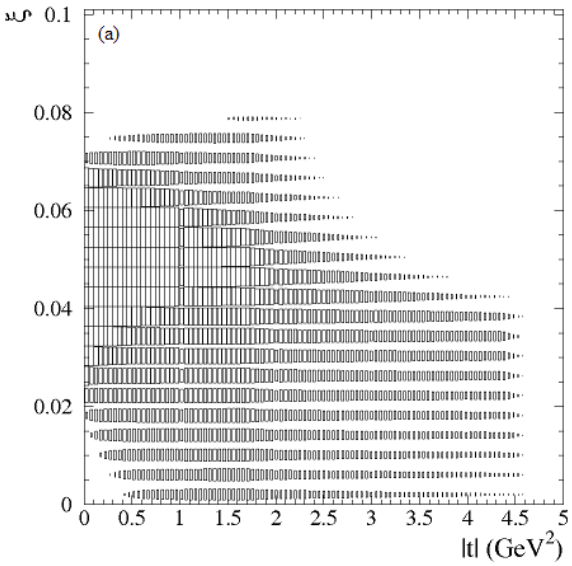

Figure 5.9 Geometric acceptance of the dipole spectrometer with flat t dependence and detectors at $8\sigma_x$ positions [110].

CHAPTER 6

DATA SELECTION OF DIJET SAMPLE

The data used in this analysis was taken in early 2003. It was selected because it was the first data that included any FPD spectrometers (the dipole spectrometer) integrated into the DØ readout. As the FPD system was still being commissioned at this time, the running conditions varied over the course of 2003, so this analysis is restricted to the first part of the year where conditions were stable and well understood[1].

6.1 Run Selection

The stable running period for the FPD used in this analysis was for physics quality data collected from February 28, 2003 (run 173522, store 2285) to May 16, 2003 (run 176974, store 2549), and consisted of 365 runs with an integrated luminosity of 43.51 pb^{-1}. The dipole detectors were not inserted at the beginning of each store, so the first step was to select only those runs where the dipole detectors were inserted for the entire run. This selection retained 147 runs. In addition, runs marked as bad (*e.g.* there was a problem with a detector subsystem) by the SMT, CFT or Calorimeter were removed from the list, resulting in 111 runs remaining for the analysis with an integrated luminosity of 13.24 pb^{-1}.

The data was reprocessed through version p14.06.02 if the DØ reconstruction code into the TMB (ThuMBnail) format resulting in what is known as the QCDtmbfix2 dataset. The FPD part of the data was not reconstructed due to lack of reconstruction

[1]For the first third of the year, the gains and timing were fixed. Afterwards, changes to the gain and timing of the system were applied during the commissioning leading to a fragmented dataset.

infrastructure at the time and therefore resided in the raw data known as the FPDraw dataset.

6.2 Data Merging

Since the data existed in two independent datasets, it was necessary to merge the two samples together in order to perform an analysis including both the FPD and central DØ information. This involved the merging of the raw FPD data and reconstructed central DØ data as shown in Fig. 6.1.

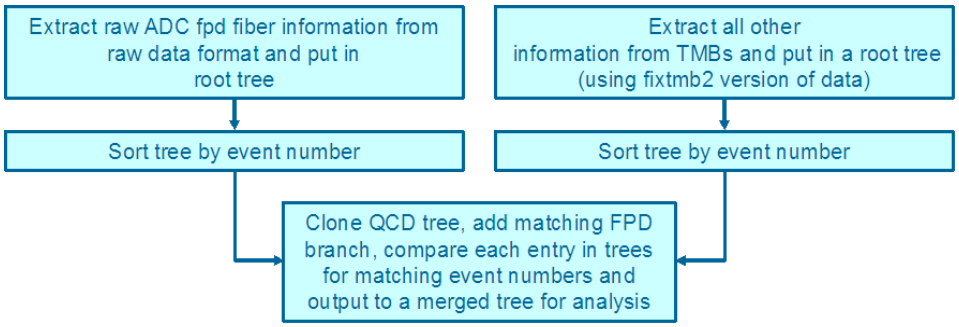

Figure 6.1 Schematic illustration of data merging.

The data was extracted from each dataset on a run-by-run basis, with the resulting information residing in a root-tree format. Each run tree was sorted by event number, then the FPD and QCD trees were merged together into the final analysis tree. The FPD data is reconstructed on an event-by-event basis as the data is being analyzed.

6.3 Trigger Selection

Once the runs were selected and merged, the next step was to limit the analysis to the triggers of interest. For this analysis, that consists of a subset of the available jet triggers: JT_25TT_NG, JT_25TT_GapN, JT_25TT_GapS, JT_25TT_GapSN, and JT_45TT.

At the first hardware trigger level (L1) these triggers all require two jet towers ($\phi \times \eta = 0.2 \times 0.2$) above a five GeV threshold. The second tower requirement is needed to suppress noise in the calorimeter and could either be part of the leading jet or the second jet. Some of the triggers also require a gap as determined by lack of activity in the LM scintillators on one or both sides of the interaction point (GapN corresponds to a gap on the North side, which is the outgoing antiproton side on which the dipole spectrometer is located). At the software trigger level (L3), it is possible to run a jet algorithm, and at least one jet with 25 or 45 GeV in a 0.7 radius cone is required. The full criteria for each trigger is shown in Table 6.1.

Table 6.1 Summary of triggers used in analysis

Trigger	**L1**	**L2**	**L3**
JT_25TT_NG	2 towers > 5 GeV	none	1 jet with $E_T > 25$ GeV
JT_25TT_GapN	2 towers > 5 GeV Empty North LM	none	1 jet with $E_T > 25$ GeV
JT_25TT_GapS	2 towers > 5 GeV Empty South LM	none	1 jet with $E_T > 25$ GeV
JT_25TT_GapSN	2 towers > 5 GeV Both LM empty	none	1 jet with $E_T > 25$ GeV
JT_45TT	2 towers > 5 GeV	none	1 jet with $E_T > 45$ GeV

6.4 Event Cuts

An event must pass certain quality requirements before it is used in an analysis. This is necessary to remove possible sources of fake triggers and ensure that the event consists of objects that are well measured. To remove intermittent hardware problems, events that fall within particular Luminosity Blocks (LBs) can be removed. All remaining events are subject to standard DØ QCD cuts for a jet analysis.

6.4.1 Vertex

A good measurement of the event's primary vertex is necessary in order to have a proper offline reconstruction of a jet's properties. The first vertex quality cut that is applied is based on the number of tracks (N_{trk}) associated with the primary vertex. The the distribution of the variable is shown in Fig. 6.2.

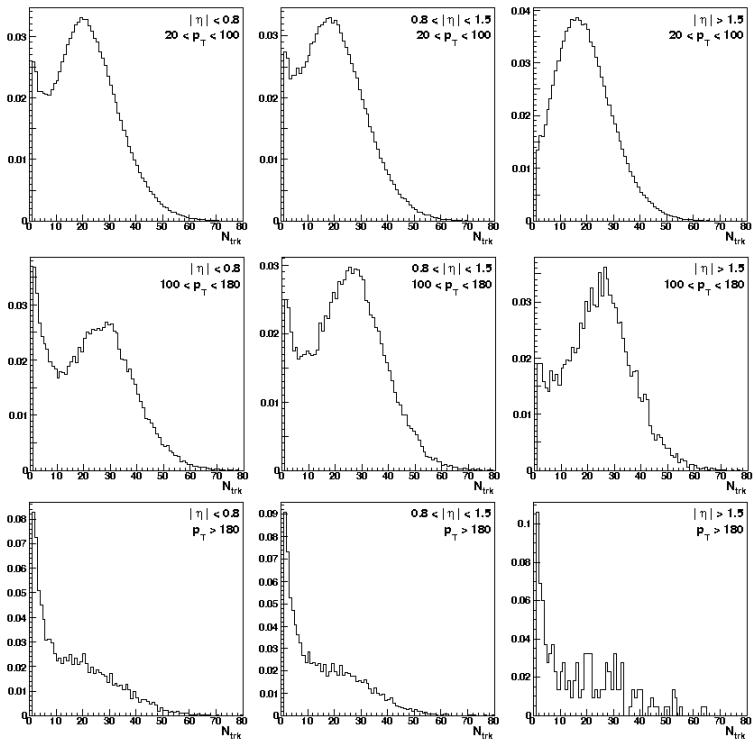

Figure 6.2 Distributions of number of tracks associated with primary vertex in bins of η and p_T of the leading jet. From left to right, the columns correspond to central ($|\eta| < 0.8$), intermediate ($0.8 < |\eta| < 1.5$), and forward ($|\eta| > 1.5$). From top to bottom, the rows correspond to low-p_T ($20 < p_T < 100$ GeV), medium-p_T ($100 < p_T < 180$ GeV), and high-p_T ($p_T > 180$ GeV).

From these plots, it is clear that there are a subset of events with few reconstructed tracks. For events in this lower peak, it is likely there is a mis-measurement of the event so such vertices cannot be trusted and the event is discarded. The applied cut is:

$$N_{trk} > 4, \tag{6.1}$$

to remove these events.

A primary source of the low number of tracks are the gap triggers which are often fired on empty or noisy events as shown in Fig. 6.3.

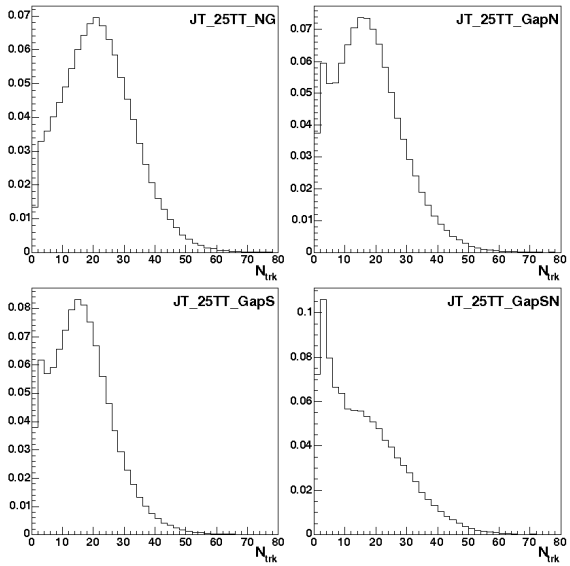

Figure 6.3 Distributions of number of tracks associated with primary vertex split out by trigger.

For the JT_25TT_NG trigger, there is no excess of tracks at low multiplicity. However, as a gap is introduced in the event, such a peak becomes apparent. The primary source is from the double gap trigger (JT_25TT_GapSN) which is often fired by random noise in the calorimeter. Forward bins of Fig. 6.2 exhibit a suppressed peak at low multiplicity since such bins require activity that would spoil a gap. Increasing p_T allows for more fake events since the cross-section for obtaining such real events decreases.

The z position of the vertex for events that pass the previous cut is also used. The distribution of this variable as shown in Fig. 6.4. It follows a clear Gaussian centered at zero with a σ of 26 cm.

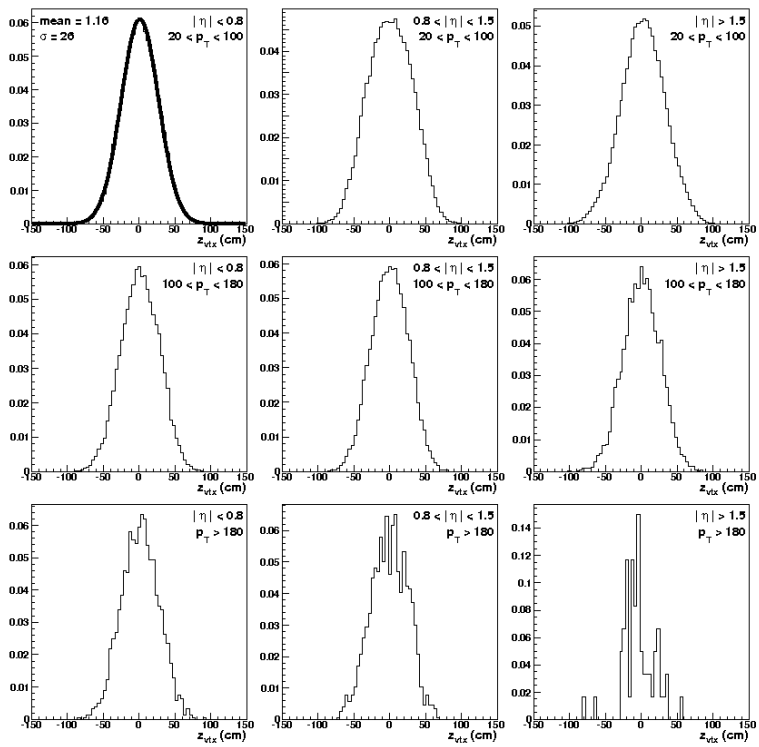

Figure 6.4 Distributions of z position of primary vertex in bins of η and p_T of the leading jet for events that pass the N_{trk} cut. From left to right, the columns correspond to central ($|\eta| < 0.8$), intermediate ($0.8 < |\eta| < 1.5$), and forward ($|\eta| > 1.5$). From top to bottom, the rows correspond to low-p_T ($20 < p_T < 100$ GeV), medium-p_T ($100 < p_T < 180$ GeV), and high-p_T ($p_T > 180$ GeV).

A fiducial cut that restricts the interactions to be centrally located in the detector such that the tracking and energy measurements are reliable is applied:

$$|z_{vtx}| < 50 \text{ cm}, \tag{6.2}$$

where the cut is set at 2σ from the interaction point.

6.4.2 Missing E_T

Momentum conservation requires that the sum of the vector transverse momenta of all particles must be zero in each event. However, some events have high-momentum particles that are difficult or impossible to measure (*e.g.* muons, neutrinos). In these

cases, the conservation of momentum will seem to be violated. In the jet sample, events containing such particles are expected to be quite rare. However, there are situations where the energy might not be balanced (*e.g.* cosmic rays particles, detector malfunction, fluctuations in jet development) that can result in large missing energy ($\not\!\!E_T$). The $\not\!\!E_T$ is calculated using the the event's primary vertex and the energies in the cells of the calorimeters. It is a vector in (x, y) defined as:

$$\mathbf{METC} = \sum_i E_{Ti}(\hat{\mathbf{x}}\phi_i + \hat{\mathbf{y}}\phi_i), \tag{6.3}$$

where i corresponds to every cell above threshold. The ratio of the magnitude of the METC vector and $p_T^{leading}$ (the transverse momentum of the leading jet before any JES corrections) is shown in Fig. 6.5.

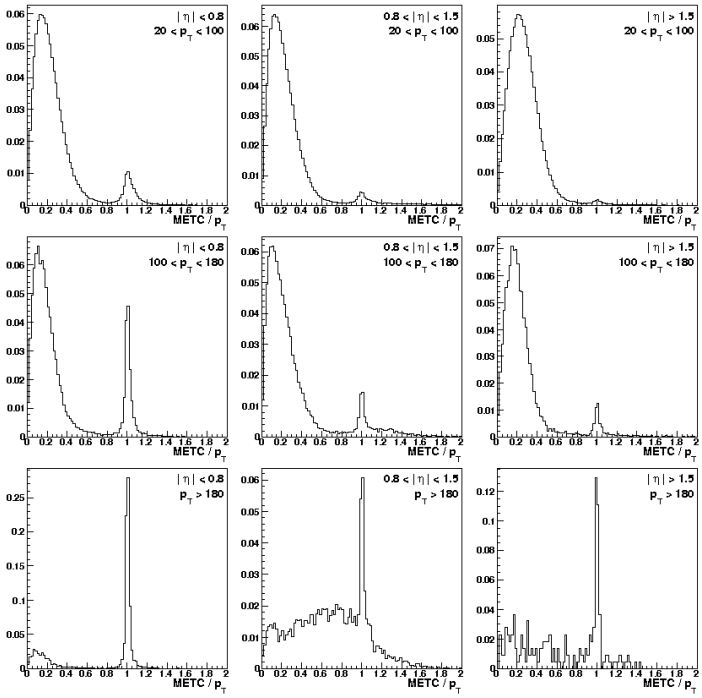

Figure 6.5 Distributions of METC / $p_T^{leading}$ in bins of η and p_T of the leading jet. From left to right, the columns correspond to central ($|\eta| < 0.8$), intermediate ($0.8 < |\eta| < 1.5$), and forward ($|\eta| > 1.5$). From top to bottom, the rows correspond to low-p_T ($20 < p_T < 100$ GeV), medium-p_T ($100 < p_T < 180$ GeV), and high-p_T ($p_T > 180$ GeV).

The peak at METC/$p_T \approx 1$ corresponds to the fake events that we wish to remove which motivates the cut:

$$\not{E}_T < 0.7 p_T^{\text{leading}}. \tag{6.4}$$

The peak is primarily from events where a single jet is reconstructed with the majority of the energy, requiring the METC to balance the momentum. A primary source for the fake events is once again largely from the gap triggers as shown in Fig. 6.6. As they are often fired by a noisy calorimeter, they only reconstruct as a single jet, balanced through METC. For this reason, the N_{trk} and METC cut are highly correlated, in many cases removing the same event.

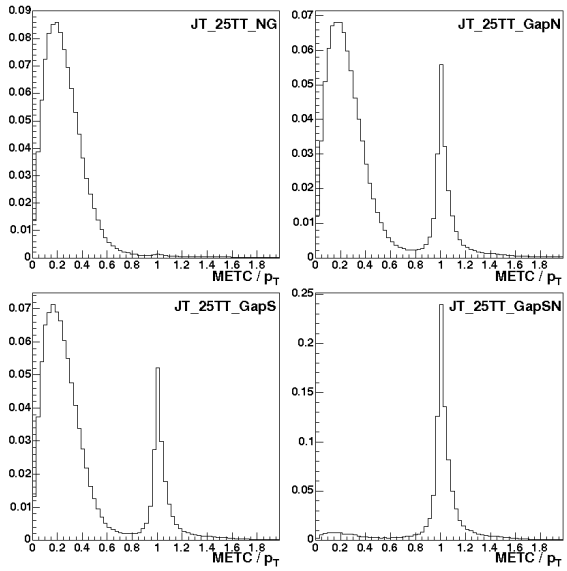

Figure 6.6 Distributions of METC / $p_T^{leading}$ split out by trigger.

6.5 Jet Cuts

It is possible for the DØ reconstruction code to sometimes reconstruct jets from electrical noise or uranium decays in the calorimeter. To minimize such contamination,

requirements are placed on jet parameters to assure acceptable jet quality. The leading jet and second jet distributions are shown, both normalized to unit area.

6.5.1 Electromagnetic Fraction

The ElectroMagnetic Fraction (EMF) is the fraction of a jet's measured uncorrected energy that is deposited in the four electromagnetic layers of the calorimeter. The distributions are shown in Fig 6.7.

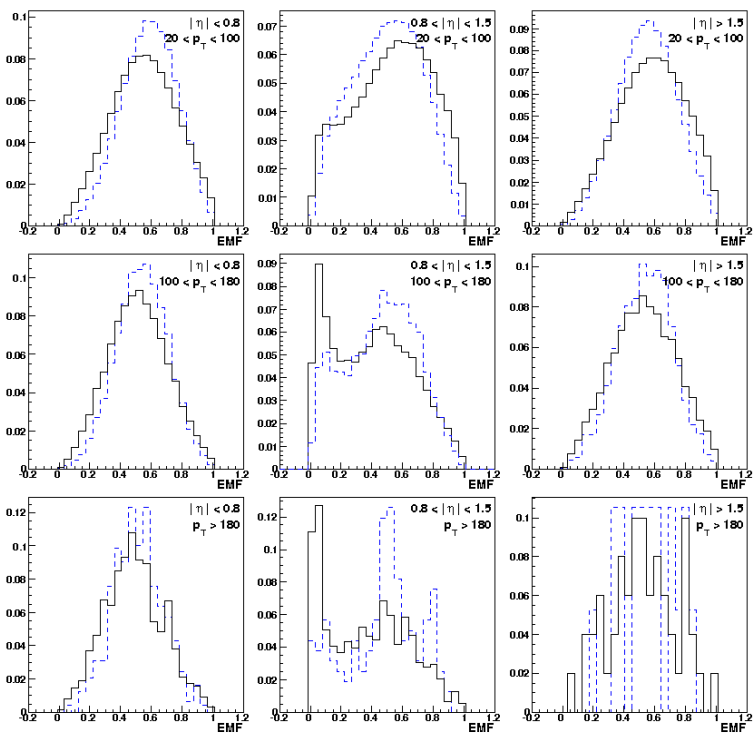

Figure 6.7 Distributions of EMF in bins of η and p_T. The solid black line is the leading jet distribution and the dashed blue line is the second jet distribution. All distributions are normalized to unit area. From left to right, the columns correspond to central ($|\eta| < 0.8$), intermediate ($0.8 < |\eta| < 1.5$), and forward ($|\eta| > 1.5$). From top to bottom, the rows correspond to low-p_T ($20 < p_T < 100$ GeV), medium-p_T ($100 < p_T < 180$ GeV), and high-p_T ($p_T > 180$ GeV).

The EMF for good jets can vary widely. Some jets contain many neutral pions that decay into two photons that then shower predominantly in the EM layers. Other

jets might have few such particles and shower predominantly in the hadronic part of the calorimeter. Jets with extreme values are likely to have been created by a few noisy cells in the EM section of the calorimeter. Also jets with high EMF are more likely to correspond to photons or electrons. Therefore, the applied cut is:

$$0.05 < \text{EMF} < 0.95. \tag{6.5}$$

As the p_T of the jets grow, the distributions shift to the left since a more energetic jet would be expected to penetrate deeper into the calorimeter and deposit less of its energy in the EM layers. For the same reason, the leading jet on average has a lower mean than the second jet. In the ICR, an excess of low EMF can be seen due to the ICD which has no EM component. For this reason, the lower end of the EMF cut is not applied to jets in this η region.

6.5.2 Coarse Hadronic Fraction

The Coarse Hadronic Fraction (CHF) is defined as the fraction of a jet's measured uncorrected energy that is deposited in the coarse hadronic layer of the calorimeter. The distributions are shown in Fig 6.8.

Only a fraction of the shower energy should be deposited in this outermost layer, and therefore when a large fraction of a jet's energy is found here, it suggests there might be an instrumental problem, usually because of noise in the electronics. To limit such contamination a cut of:

$$\text{CHF} < 0.4, \tag{6.6}$$

is applied.

The distributions exhibit the expected behavior of peaking at zero with a roughly exponential drop as the percentage of energy deposited in this layer increases. In the

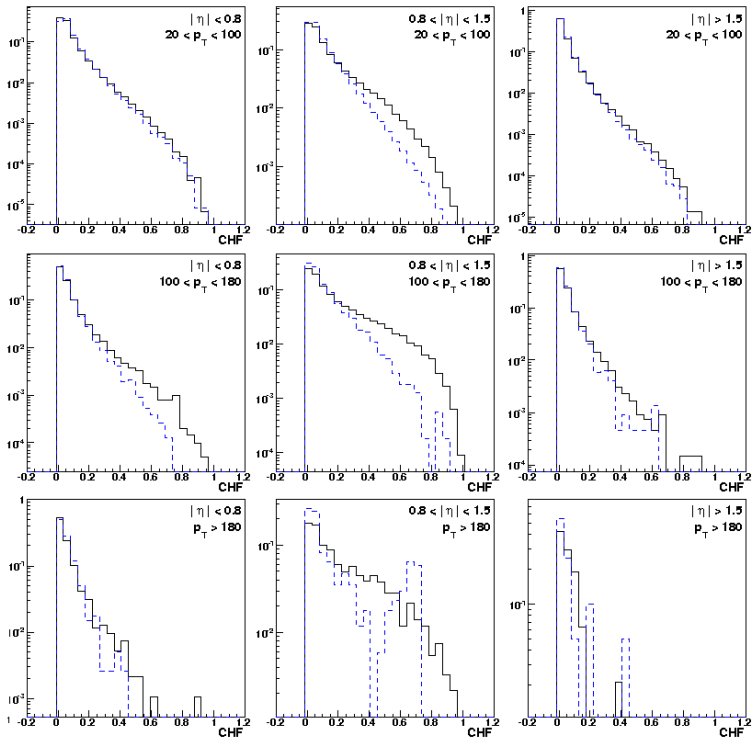

Figure 6.8 Distributions of CHF with a logarithmic scale in bins of η and p_T. The solid black line is the leading jet distribution and the dashed blue line is the second jet distribution. All distributions are normalized to unit area. From left to right, the columns correspond to central ($|\eta| < 0.8$), intermediate ($0.8 < |\eta| < 1.5$), and forward ($|\eta| > 1.5$). From top to bottom, the rows correspond to low-p_T ($20 < p_T < 100$ GeV), medium-p_T ($100 < p_T < 180$ GeV), and high-p_T ($p_T > 180$ GeV).

ICR region, there is an enhancement of energy deposited in the CH as expected due to the lack of an EM section for the ICD.

6.5.3 Hot Fraction

The "hot fraction" (HotF) of a jet is defined as the largest uncorrected transverse energy observed in any cell divided by that found in the second highest cell in the jet and by definition must be higher than unity. The distributions are shown in Fig 6.9.

When a jet has a very large value for HotF, the jet is likely to have been caused by substantial noise in one readout cell of the calorimeter. Even if a jet has very energetic

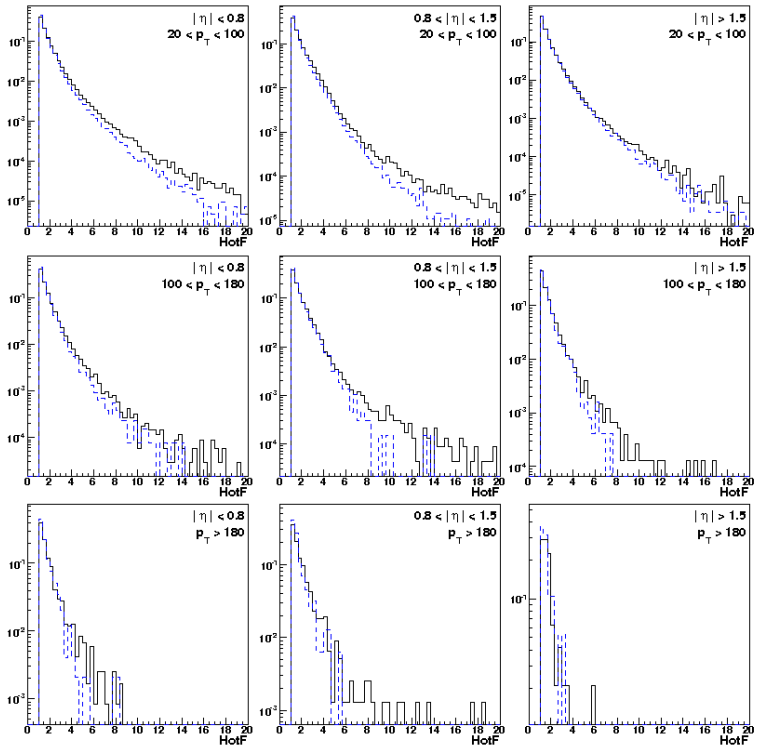

Figure 6.9 Distributions of HotF with a logarithmic scale in bins of η and p_T. The solid black line is the leading jet distribution and the dashed blue line is the second jet distribution. All distributions are normalized to unit area. From left to right, the columns correspond to central ($|\eta| < 0.8$), intermediate ($0.8 < |\eta| < 1.5$), and forward ($|\eta| > 1.5$). From top to bottom, the rows correspond to low-p_T ($20 < p_T < 100$ GeV), medium-p_T ($100 < p_T < 180$ GeV), and high-p_T ($p_T > 180$ GeV).

particles in it, we would not expect a factor of ten more energy in one cell than in its neighboring cells and therefore we apply a cut of:

$$\text{HotF} < 10. \tag{6.7}$$

6.5.4 n90 Variable

The n90 variable is defined as the minimum number of towers that contain at least 90% of a jet's measured uncorrected transverse energy. The major difference between

n90 and HotF is that HotF refers to single readout cells and not to full towers. The distributions are shown in Fig 6.10.

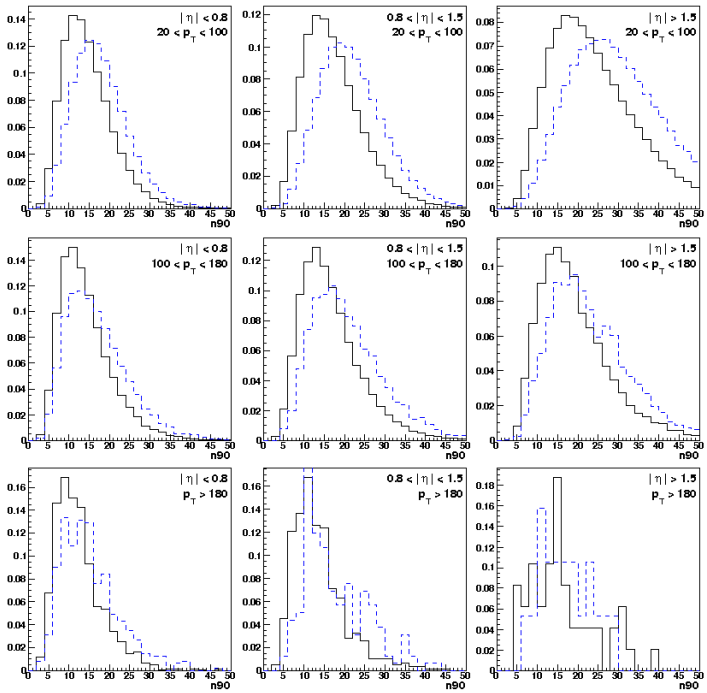

Figure 6.10 Distributions of n90 in bins of η and p_T. The solid black line is the leading jet distribution and the dashed blue line is the second jet distribution. All distributions are normalized to unit area. From left to right, the columns correspond to central ($|\eta| < 0.8$), intermediate ($0.8 < |\eta| < 1.5$), and forward ($|\eta| > 1.5$). From top to bottom, the rows correspond to low-p_T ($20 < p_T < 100$ GeV), medium-p_T ($100 < p_T < 180$ GeV), and high-p_T ($p_T > 180$ GeV).

When a jet is caused by two hot channels in the same tower, a selection on HotF will not remove it, while requirements on n90 can. We require:

$$\text{n90} > 1. \tag{6.8}$$

In addition, this variable is correlated with the "size" of the jet, with smaller n90 values correlating with narrower jets (*i.e.* fewer towers containing the majority of the

energy). Leading jets are narrower than second jets, and forward jets appear broader due to the smaller size of the projective towers in the EC calorimeter.

6.5.5 L1 Scalar E_T

The L1 scalar transverse energy (L1SET) is computed from the L1 calorimeter towers in an $R = 0.5$ cone around the jet direction. This is compared to uncorrected jet energy deposited in all layers except for the coarse hadronic as the CH is not included in the calorimeter L1 readout. The ratio of the L1SET to the uncorrected jet energy is shown in Fig 6.11.

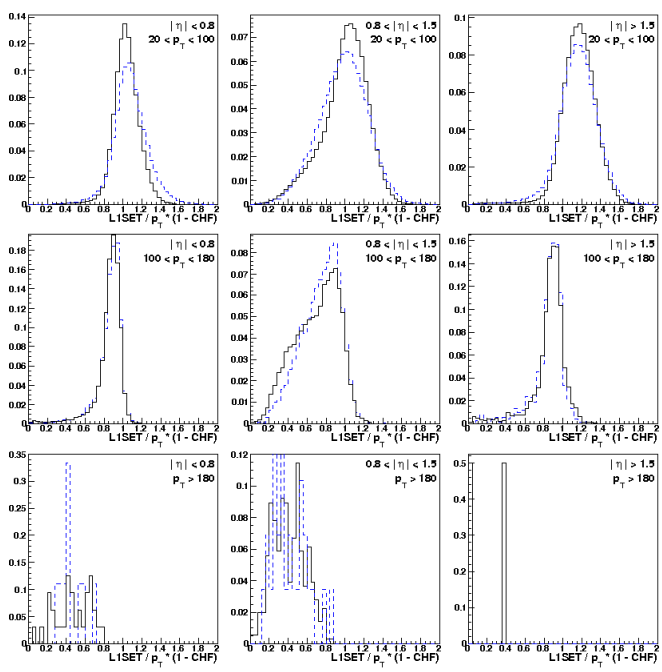

Figure 6.11 Distributions of L1SET / p_T(1-CHF) in bins of η and p_T. The solid black line is the leading jet distribution and the dashed blue line is the second jet distribution. All distributions are normalized to unit area. From left to right, the columns correspond to central ($|\eta| < 0.8$), intermediate ($0.8 < |\eta| < 1.5$), and forward ($|\eta| > 1.5$). From top to bottom, the rows correspond to low-p_T ($20 < p_T < 100$ GeV), medium-p_T ($100 < p_T < 180$ GeV), and high-p_T ($p_T > 180$ GeV).

The change of the distribution in the ICR region and at high-p_T motivates different cut conditions depending on the η_{det} of the jet within the calorimeter and the value of L1SET by itself. This motivates a final cut of:

$$\begin{aligned} & 0.4p_T(1-\text{CHF}), \quad \text{for} \quad |\eta_{det}| < 0.8, \quad |\eta_{det}| > 1.5 \\ \text{L1SET} \quad > \quad & 0.2p_T(1-\text{CHF}), \quad \text{for} \quad 0.8 < |\eta_{det}| < 1.5, \quad \text{or} \\ & 80 \text{ GeV}, \end{aligned} \tag{6.9}$$

which is designed to have a high rejection.

6.5.6 Corrected Jet Energy

The final requirement is based on corrected jet energy. The leading jet is required to have energy greater than or equal to the L3 requirement of the trigger that fired the event. All other jets are required to have at least 20 GeV.

6.5.7 Dijet Event

If the original leading and second jet (after jet energy scale correction) do not satisfy all jet quality cuts, the event is not considered to be a valid dijet event and is rejected.

6.6 Event Summary

Table 6.2 shows the rejection of events as the various cuts are applied, and the final number of events in the "good" dijet sample.

Each cut is applied in succession, with the number of events that pass the dijet requirement listed as well as the percentage of events that survive from the previous cut as a measure of the rejection of each new cut. Many of the cuts are correlated with each

Table 6.2 Summary of number of events after quality cuts

Cut	**Number of Events**	**% of previous cut**
Trigger filter	1440654	
BadLBN	1380458	95.82
Trigger "efficient"	1373478	99.49
N_{trk}	1192191	86.80
z_{vtx}	1095297	91.87
$\not{E}_T$	1073082	97.97
p_T	1024454	95.47
EMF	989933	96.63
CHF	967838	97.77
HotF	965351	99.74
n90	965302	99.99
L1SET	958123	99.26
TOTAL AFTER ALL CUTS	958123	

other (*e.g.* N_{trk} and $\not{E}_T$ expected to remove many of the same double gap events), while others have a high rejection by design (*e.g.* L1SET). This leads to the increasing rejection of each cut as they are applied in succession.

CHAPTER 7

ANALYSIS

DØ now has the capability of making measurements of diffractive events using tags in the FPD spectrometers. Here, the initial observation of dijet events with an antiproton tag at $\sqrt{s} = 1.96$ TeV is presented.

7.1 FPD Performance

As a first step, a study of the performance of the dipole spectrometer for the data sample is required. For this study, the FPD is read out for the previously described triggers, but no jet quality cuts are applied. In the figures that follow, each column corresponds to a different detector, with the first column corresponding to D1I and the second to D2I.

The first quantity is the ADC distribution for a selection of fibers as shown in Fig. 7.1. A few representative fibers from the x frame are presented where the solid line corresponds to the raw ADC count and the blue dashed line to ADC counts from events where single validated hits (hits with one segment from each plane in agreement with each other) are found in both detectors in the same event.

As can be seen in Fig. 7.1, there is no clear separation of signal and pedestal in the raw distribution. After application of pedestal subtraction and discrimination, the ADC distribution of events that contain a prototrack (single validated hits in each detector that are correlated with each other) are overlaid, showing a distribution of the signal ADC. For the D2I column, this second distribution indicates a signal peak within the

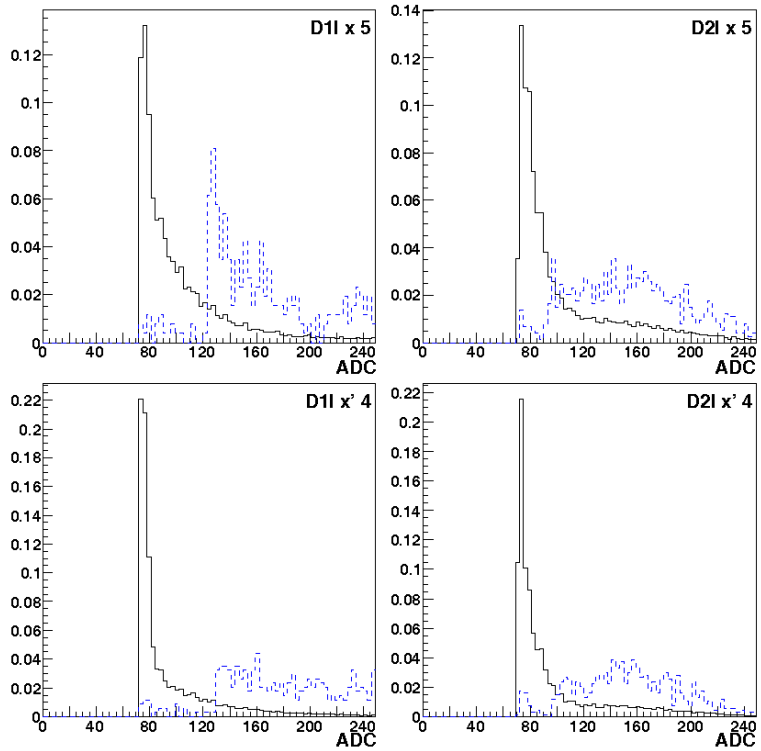

Figure 7.1 ADC distributions of representative fibers normalized to unit area. The left column corresponds to D1I and the right to D2I. The black solid line corresponds to the raw ADC distribution, the blue dashed line corresponds to the distribution of events with a prototrack.

pedestal tail. For the D1I column, the sudden turn on indicates that the discrimination of this detector might be too aggressive, throwing away some possible good events.

Figure 7.2 shows the correlations between prime and unprime layers in each detector plane. The first row shows the u plane, the second corresponds to the x plane, and the last to the v plane. All fibers above threshold are plotted for events that have a single validated hit in both detectors.

The expected correlation between fibers can be seen, where the fiber number is either the same in both layers or shifted by one. Some additional uncorrelated "noise" and cross-talk can also be observed. The correlation band indicates that the signals from

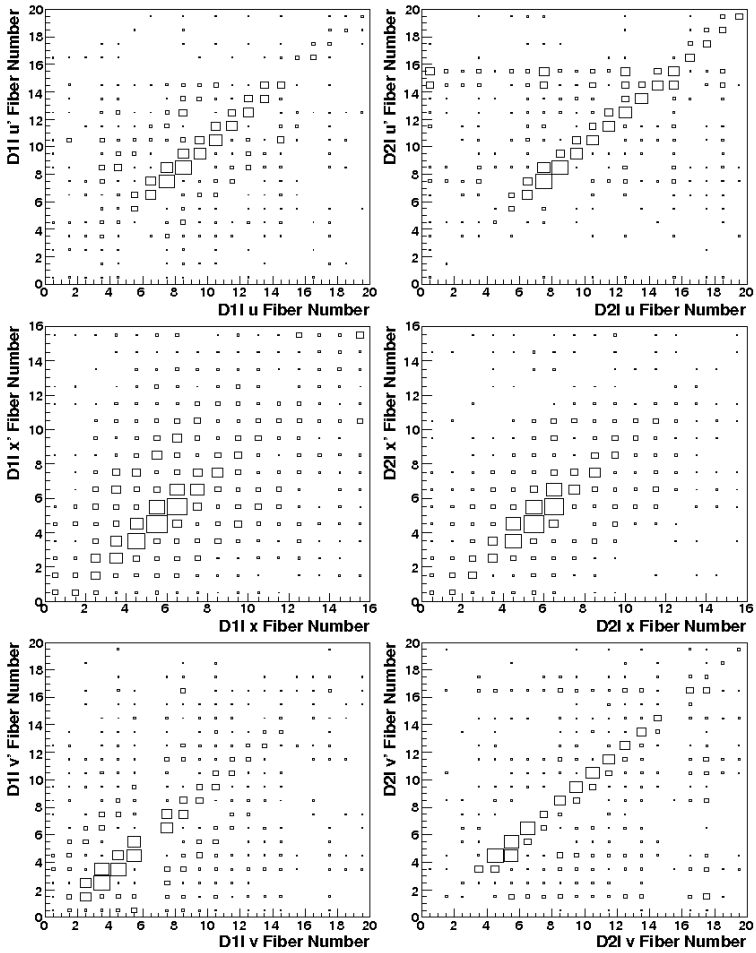

Figure 7.2 Fiber correlations between layers as a function of plane for the dipole spectrometer. The left column corresponds to D1I and the right to D2I. The top row shows the u plane, the middle corresponds to the x plane, and the bottom to the v plane.

the system are consistent with real particles passing through the detectors. It should be noted that the step of going from fibers to segments discards the non-correlated hits.

Figure 7.3 shows the fiber occupancy by layer (equivalent to the projections of Fig. 7.2). The two columns show the occupancy for the D1I and D2I detectors, with rows showing the occupancy of the u, u', x, x', v, and v' layers respectively. The solid line in each plot shows the projection for all events (including halo) while the blue dashed line corresponds to the fiber occupancy for events with a prototrack.

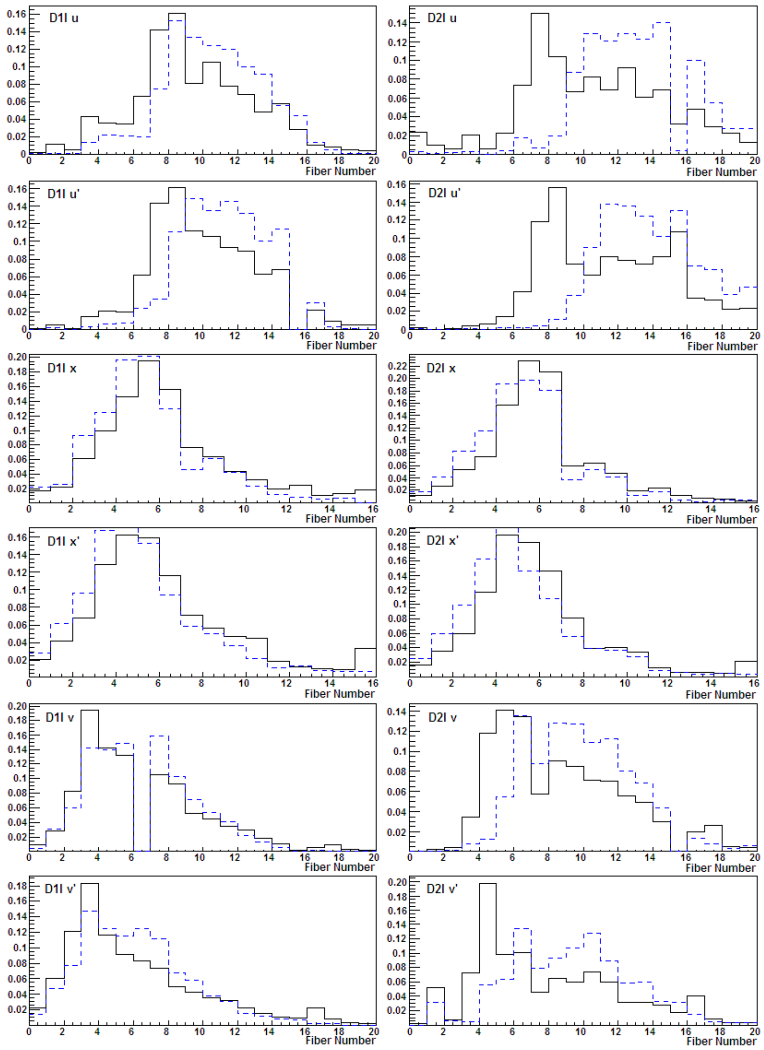

Figure 7.3 Fiber occupancies for each layer in the dipole spectrometer normalized to unit area. The left column corresponds to D1I and the right to D2I. From top to bottom, the rows correspond to the u, u', x, x', v, and v' layers respectively. The solid lines correspond to all events (including halo) while the blue dashed lines correspond to events with a prototrack.

This figure exhibits the same structure as seen in the hit correlation plots shown in Chapter 5. The prototracks are found in fibers further from the bottom of the detector, especially in the u and v frames of D2I.

Next we must convert the fibers into segments and then hits as described in Chapter 5. When these steps are performed, the relative position provided by the u and v

segments can be compared to the position provided by the x segment as shown in Fig. 7.4.

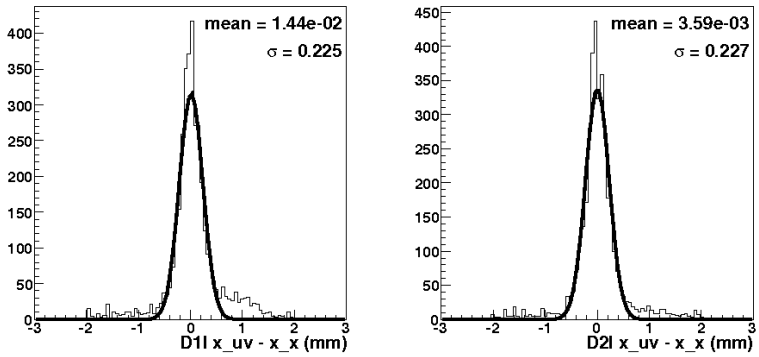

Figure 7.4 Hit resolution for each detector of the dipole spectrometer with mapping correction applied overlaid with the Gaussian fit. The left column corresponds to D1I and the right to D2I.

From this figure, it is clear that the hit position provided by the u and v segments is close to that provided by the x segment providing a measure of the hit resolution of the detector. The sigma from a Gaussian fit is 225 mm and 227 mm for D1I and D2I respectively. This corresponds to a hit resolution of 159 mm and 160 mm respectively. As long as the two measurements for x_d agree within 4σ, the hit is considered to be validated.

Once hits have been found, we can observe the hit map of where they fall within the detector as shown in Fig. 7.5. The first row corresponds to hits where there is one validated hit in each detector in the same event. The second row corresponds to events where each detector has one or more validated hits, independent of the state of the other detector. The final row removes the validation requirement and shows all hits as determined by any two segments.

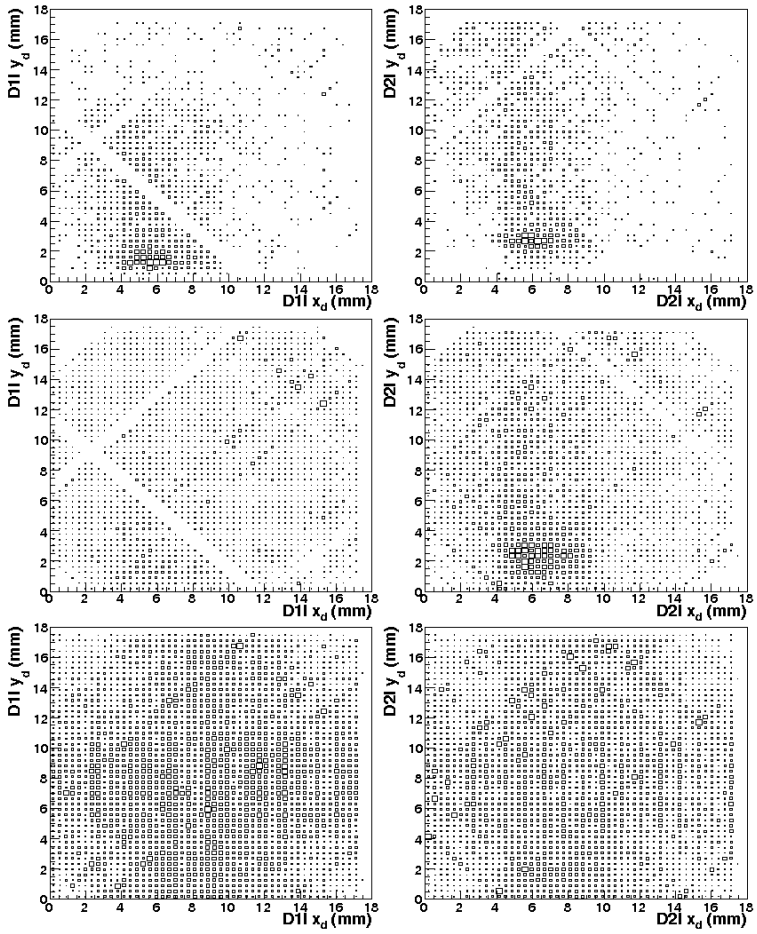

Figure 7.5 Hit maps for each detector of the dipole spectrometer. The left column corresponds to D1I and the right to D2I. The top row corresponds to events with one validated hit in each detector in the same event, the middle row corresponds to events with a validated hits in the detector, independent of the state of the other detector, and the bottom row corresponds to all hits as determined by any two segments.

From the first two rows, the dead channels can clearly be seen. As three segments are required for a validated hit, validation is biased against these dead channels. In the second row, the outline of the active area as described in Chapter 4 can clearly be noted as the corners are clipped since there are only two layers overlapping each other in this region. It is also evident in D1I, that relaxing the requirement that the two detectors each have hits at the same time allows for some contamination by "hot" fibers. This

becomes more evident in the third row, where the bias against dead channels is lifted by the removal of the validation, but hot segments become more prevalent.

The final step is to show that the correlation between hits in the two detectors is consistent with particles passing through the spectrometer. This is shown in Fig. 7.6 where the expected halo and in-time bands can clearly be seen for different triggers.

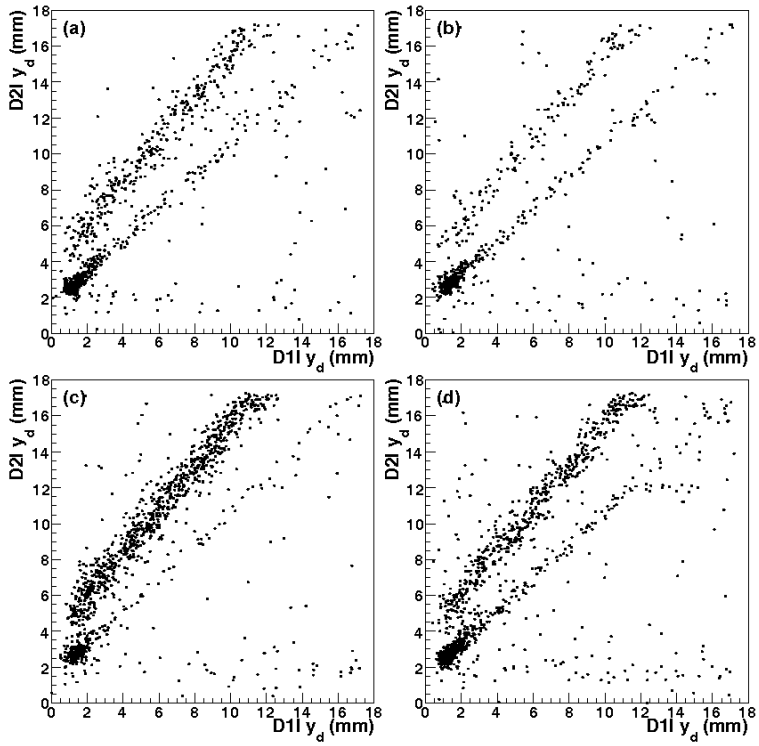

Figure 7.6 Hit correlation between detectors in the dipole spectrometer for different triggers: (a) JT_25TT_NG, (b) JT_25TT_GapS, (c) JT_25TT_GapN, and (d) JT_45TT.

The in-time band is strongest for the JT_25TT_GapN (Fig. 7.6(c)) sample as expected. The halo band is stronger for the JT_25TT_GapS (Fig. 7.6(b)) sample as expected, but an in-time band is also observed, warranting further study. This could be due to multiple interaction contamination or double gap events.

From this study, it appears that the dipole spectrometer is performing as expected providing detection of particles passing through the spectrometer and providing the ability to tag diffractive events.

7.2 Effect of Quality Cuts on Gaps and Tags

The next phase of the analysis is to apply the quality cuts described in Chapter 6 and study the effect on tags and gaps. This is shown in Table 7.1. Information on this tables starts after the trigger "efficient" cut (see Table 6.2).

Table 7.1 Summary of number of gaps and tags after quality cuts

Cut	**GapN (%)**	**GapSN (%)**	**GapS (%)**	**Tag (%)**
Start	137503	64159	209696	1751
N_{trk}	115573 (84.05)	4306 (6.71)	180279 (85.97)	1582 (90.35)
z_{vtx}	107909 (93.37)	4098 (95.17)	166948 (92.61)	1458 (92.16)
$\not{E}_T$	105639 (97.90)	4008 (97.80)	163684 (98.04)	1423 (97.60)
p_T	99085 (93.80)	3845 (95.93)	152877 (93.40)	1353 (95.08)
EMF	94499 (95.37)	3635 (94.54)	146011 (95.51)	1309 (96.75)
CHF	92430 (97.81)	3544 (96.96)	142888 (97.86)	1290 (98.55)
HotF	92177 (99.73)	3526 (99.49)	142487 (99.72)	1288 (99.84)
n90	92173 (99.99)	3526 (100.0)	142478 (99.99)	1288 (100.0)
L1SET	91729 (99.51)	3506 (99.43)	141470 (99.29)	1281 (99.46)

From this table, it can be seen that the N_{trk} cut removes much of the double gap sample, as expected, since this sample is contaminated by noise. For the remaining quality cuts, the number of gaps and tags lost is minimal, and it appears that the cuts do not significantly bias against gaps or tags.

Looking in more detail at the N_{trk} and $\not{E}_T$ cuts, some striking differences between the types of events can be seen. In the following plots, the variables are binned by trigger where (a) corresponds to trigger JT_25TT_NG, (b) to JT_25TT_GapN, (c) to JT_25TT_GapSN, and (d) JT_45TT. The black histogram corresponds to events with no

gaps or tags, the blue dashed histogram corresponds to a GapN or a GapSN with or without a tag, and the red dotted histogram corresponds to tags (with or without a gap in the case of triggers (a) and (d)).

As shown in Fig. 7.7, the gap samples seem to be a significant source of events with few or no tracks, and in general the gap samples exhibit fewer tracks than the other samples. This is not entirely unexpected since gap events have reduced activity in the central detector due to the presence of the gap. This also makes such triggers prone to noise. The addition of a tag appears to remove this bias towards noise.

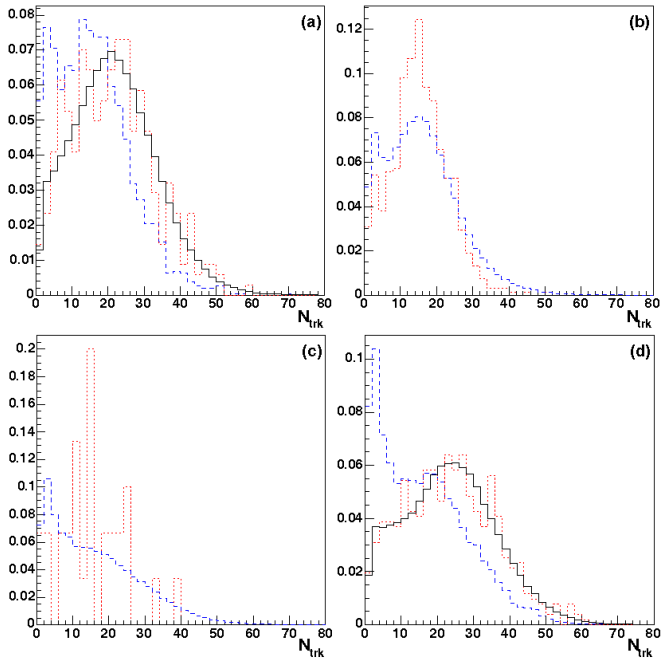

Figure 7.7 N_{trk} distribution for non-diffractive, gap and tag samples normalized to unit area. Plot (a) corresponds to trigger JT_25TT_NG, (b) to JT_25TT_GapN, (c) to JT_25TT_GapSN, and (d) JT_45TT. The black histogram corresponds to events with no gaps or tags, the blue dashed histogram corresponds to a GapN or a GapSN with or without a tag, and the red dotted histogram corresponds to tags (with or without a gap in the case of (a) and (d)).

The bias towards isolated noise in the calorimeter for gap triggers is also seen in the METC distributions as shown in Fig. 7.8. In the gap samples, the peak at one is prominent, indicating that in many cases the gap is not correlated with real activity in the calorimeter. Of particular interest is the addition of a tag in the gap sample, which largely removes this spurious peak, indicating that a tag in the FPD is strongly correlated with real activity in the central detector.

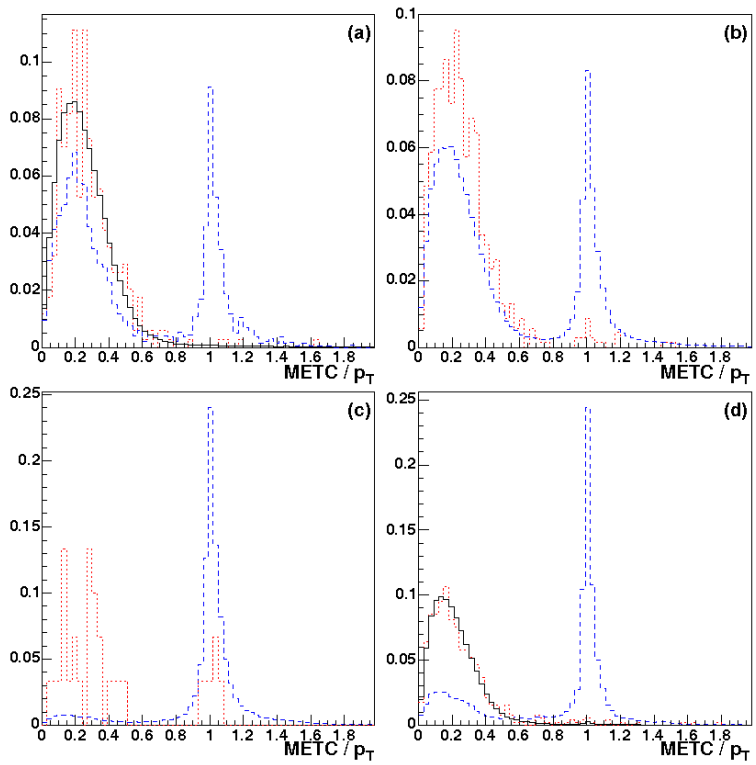

Figure 7.8 $METC/p_T^{leading}$ distribution for non-diffractive, gap and tag samples normalized to unit area. Plot (a) corresponds to trigger JT_25TT_NG, (b) to JT_25TT_GapN, (c) to JT_25TT_GapSN, and (d) JT_45TT. The black histogram corresponds to events with no gaps or tags, the blue dashed histogram corresponds to a GapN or a GapSN with or without a tag, and the red dotted histogram corresponds to tags (with or without a gap in the case of (a) and (d)).

7.3 Diffractive Dijets

The final step is to compare dijets with and without a diffractive tag. It is expected that they should have different behavior because of the different kinematics involved.

To begin with, since a diffractive event is expected to have less overall energy available and less radiation when compared to a non-diffractive event, the number of jets in an event is expected to be smaller. As shown in Fig 7.9, this is indeed the case.

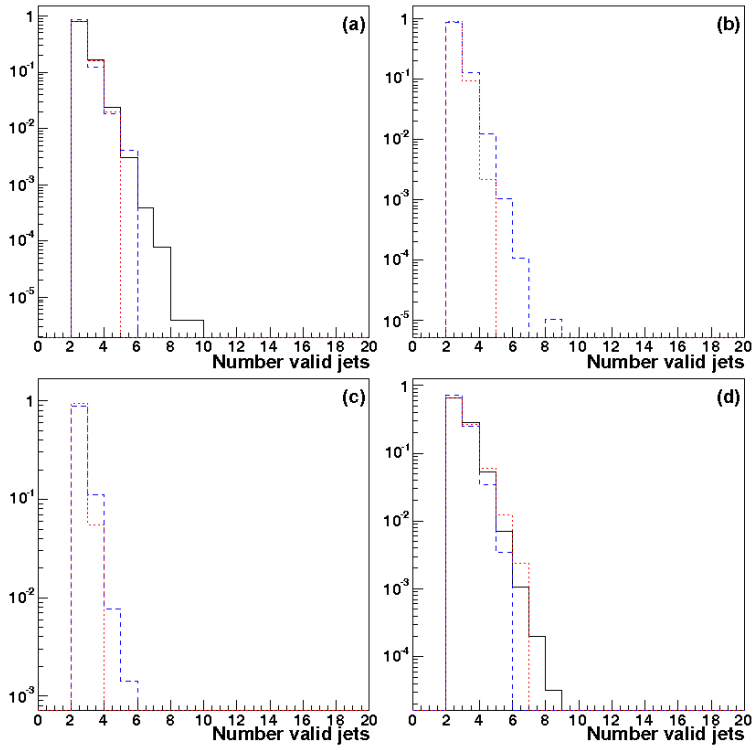

Figure 7.9 Number of jets for non-diffractive, gap and tag samples normalized to unit area. Plot (a) corresponds to trigger JT_25TT_NG, (b) to JT_25TT_GapN, (c) to JT_25TT_GapSN, and (d) JT_45TT. The black histogram corresponds to events with no gaps or tags, the blue dashed histogram corresponds to a GapN or a GapSN with or without a tag, and the red dotted histogram corresponds to tags (with or without a gap in the case of (a) and (d)).

The jet η distribution is expected to be boosted away from the side of the detector containing the tag or the gap. For a North tag, this means the diffractive system should be boosted towards positive η. Figure 7.10 shows this effect and also includes the means to quantify the boosts of different samples.

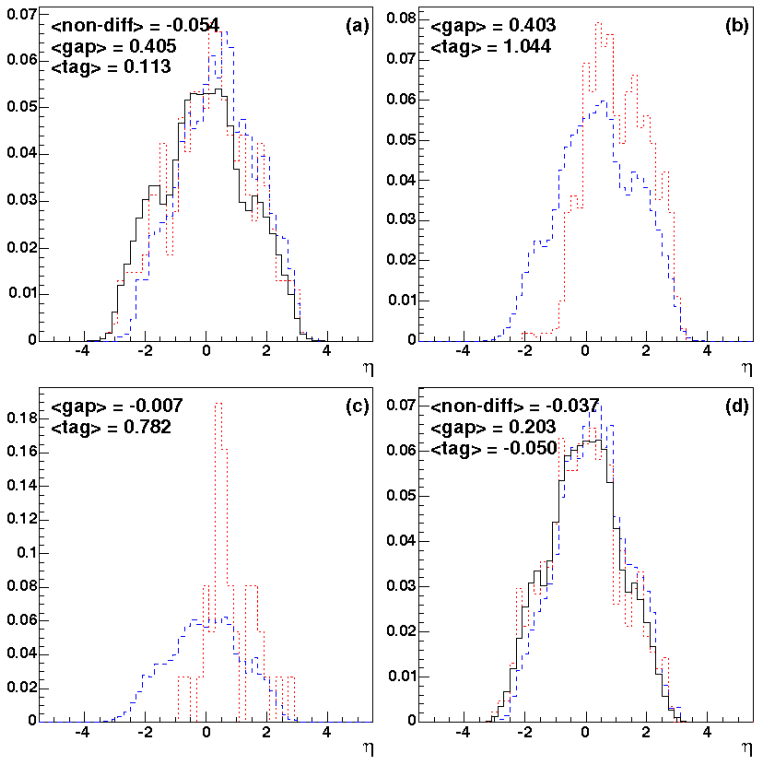

Figure 7.10 η distribution for non-diffractive, gap and tag samples normalized to unit area. Plot (a) corresponds to trigger JT_25TT_NG, (b) to JT_25TT_GapN, (c) to JT_25TT_GapSN, and (d) JT_45TT. The black histogram corresponds to events with no gaps or tags, the blue dashed histogram corresponds to a GapN or a GapSN with or without a tag, and the red dotted histogram corresponds to tags (with or without a gap in the case of (a) and (d)).

There are two effects leading to this boosted behavior. When a gap is present, there is a suppression of activity on the side of the detector with the gap. For the lower energy triggers, the mass of the diffractive system is less, and therefore, on average

the ξ of the event is smaller, leading to a larger gap (the size of the associated gap is related to ξ through $\Delta\eta \sim \ln(1/\xi)$ [111]). In addition, kinematics requires that as the mass of the system increases, the momentum fraction of the struck parton in the proton must increase, leading to a boosted system. For tagged events in the gap sample, the acceptance of the dipole spectrometer is biased towards the higher ξ events, implying that the parton from the proton is interacting with the softer component of the Pomeron to preserve the gap and leading to an enhanced boost of the tag sample with gaps. As the overall energy of the jet (mass of the diffractive system) increases due to the trigger, the phase space for forward jets is reduced, leading both the gap and tag samples to become more central as seen in Fig. 7.10(d).

The structure in the η distribution (reduction of jets in the ICR region) can be explained as a trigger bias in the finding of the leading jet. As shown in Fig. 7.11, the structure is entering into the distribution from the leading jet. The second jet distribution is smooth and has no apparent bias.

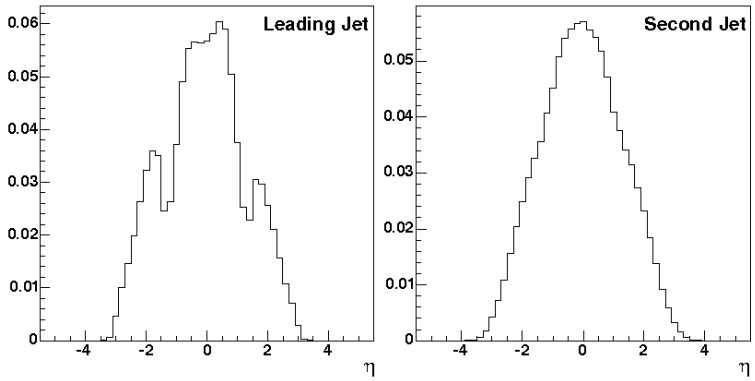

Figure 7.11 η distribution of leading and second jets.

This observation can be explained by the fact the ICD is not included in jet triggers. Therefore, a jet in this area needs to deposit sufficient energy in the surrounding EM and

FH cells to fire the trigger. The flattening of the distribution near zero can be explained by the fact that jets in this direction follow the shortest path through the tracking system, raising the possibility that tracks might be misconstructed since there will be fewer hits along the path. Such structure needs to be compensated for in any diffractive analysis since the boosted system tends to peak in this ICD region.

Figure 7.12 shows the ϕ distribution of the leading two jets. There is no expected ϕ dependence of jet production for any of the data samples, and within errors, none is observed.

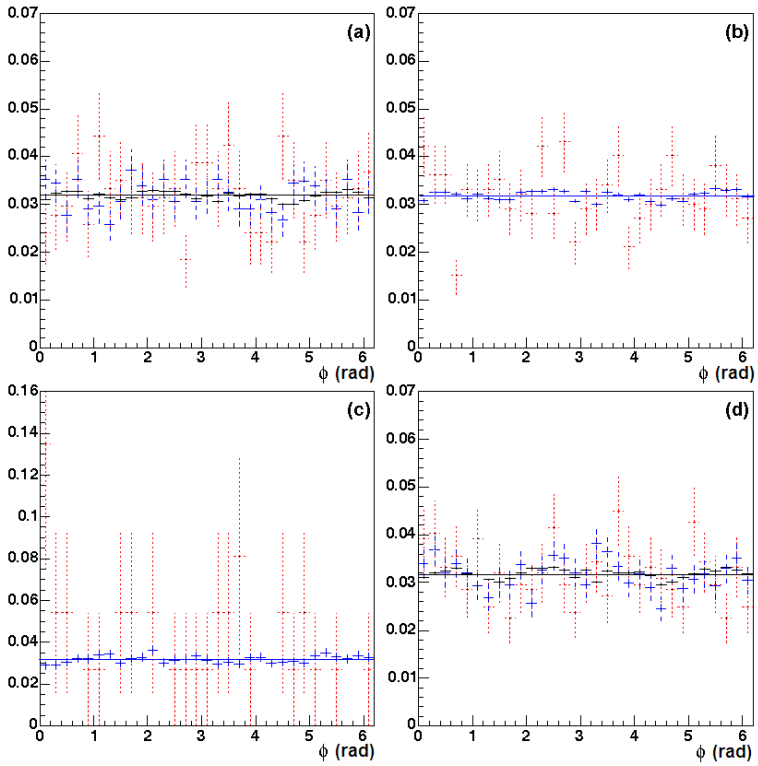

Figure 7.12 ϕ distribution for non-diffractive, gap and tag samples normalized to unit area. Plot (a) corresponds to trigger JT_25TT_NG, (b) to JT_25TT_GapN, (c) to JT_25TT_GapSN, and (d) JT_45TT. The black histogram corresponds to events with no gaps or tags, the blue dashed histogram corresponds to a GapN or a GapSN with or without a tag, and the red dotted histogram corresponds to tags (with or without a gap in the case of (a) and (d)). Errors are statistical only.

Diffractive jets are expected to be more back-to-back (peaked at $\phi = \pi$ radians) since the kinematics of the interaction requires less radiation between the jets (otherwise any gap would be spoiled), and the presence of a gap suppresses any third jet in the event. In Fig. 7.13, the angle , $\Delta\phi$, between the two leading jets is shown.

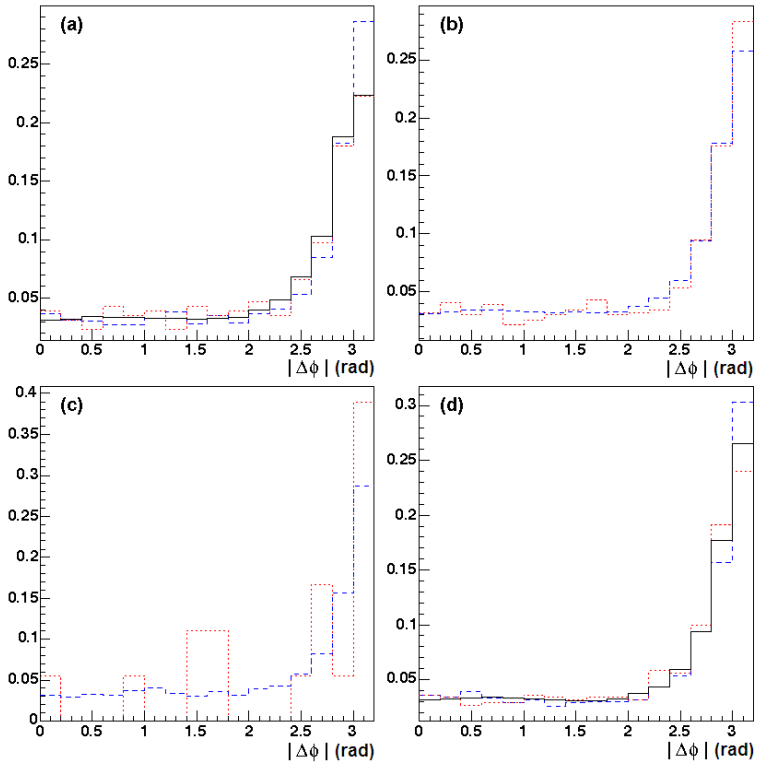

Figure 7.13 $\Delta\phi$ distribution for non-diffractive, gap and tag samples normalized to unit area. Plot (a) corresponds to trigger JT_25TT_NG, (b) to JT_25TT_GapN, (c) to JT_25TT_GapSN, and (d) JT_45TT. The black histogram corresponds to events with no gaps or tags, the blue dashed histogram corresponds to a GapN or a GapSN with or without a tag, and the red dotted histogram corresponds to tags (with or without a gap in the case of (a) and (d)).

The ratio of the different histograms is shown in Fig. 7.14 where the blue points correspond to the ratio of gap to non-gap sample for triggers (a) and (d), the red points correspond to the ratio of tags to non-gaps for triggers (a) and (d), and the ratio of tags to

gaps for (b) and (c). From this figure, it appears that the gap sample might have excess events in the most back-to-back bin, while the tag sample does not exhibit the same behavior, but the difference is not striking. This might be explained by a trigger bias arising from the two towers greater than 5 GeV requirement leading to more energetic second jets (supported by the low rejection of the p_T cut) which would tend to produce a more back-to-back jet system.

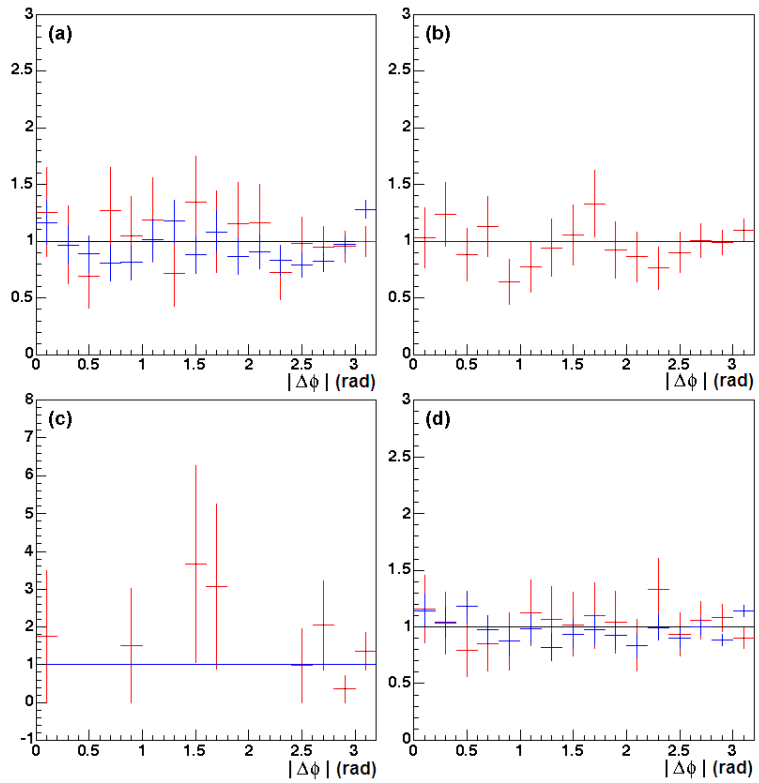

Figure 7.14 Ratio of $\Delta\phi$ distributions for non-diffractive, gap and tag samples. Plot (a) corresponds to trigger JT_25TT_NG, (b) to JT_25TT_GapN, (c) to JT_25TT_GapSN, and (d) JT_45TT. The blue points correspond to the ratio of gap to non-gap samples for (a) and (d), the red points correspond to the ratio of tags to non-gap for (a) and (d), and the ratio of tags to gaps for (b) and (c). Errors are statistical only.

Previous diffractive dijet studies [112] have observed similar p_T distributions for diffractive and non-diffractive data samples. As shown in Fig. 7.15, at lower jet energies,

the distributions are very similar. At higher energies the gap and tag samples have insufficient statistics for comparison, but up to this point, the slope is comparable.

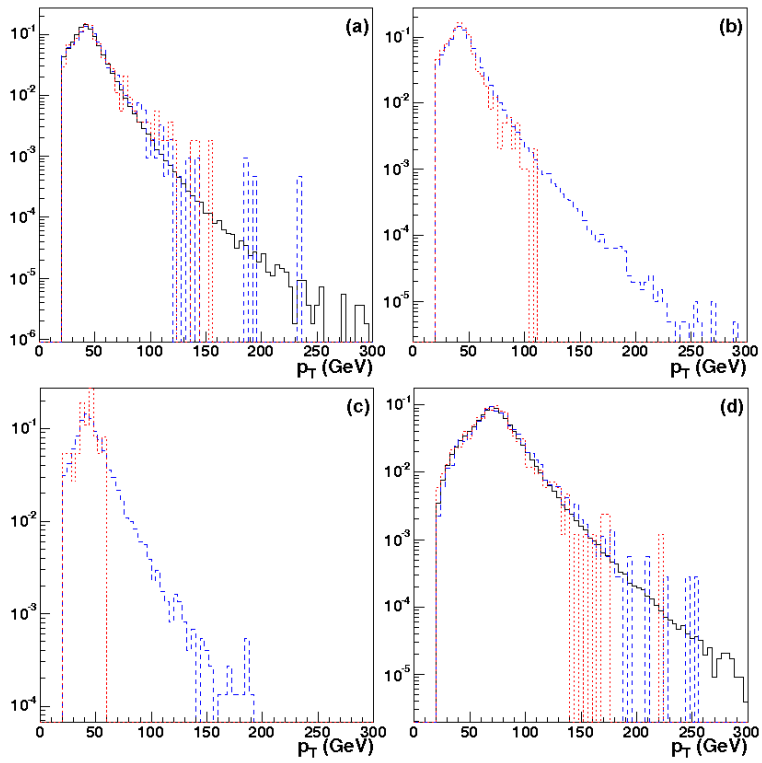

Figure 7.15 p_T spectrum for non-diffractive, gap and tag samples normalized to unit area. Plot (a) corresponds to trigger JT_25TT_NG, (b) to JT_25TT_GapN, (c) to JT_25TT_GapSN, and (d) JT_45TT. The black histogram corresponds to events with no gaps or tags, the blue dashed histogram corresponds to a GapN or a GapSN with or without a tag, and the red dotted histogram corresponds to tags (with or without a gap in the case of (a) and (d)).

The ratio of the different histograms is shown in Fig. 7.16 where the blue points correspond to the ratio of gap to non-gap sample for triggers (a) and (d), the red points correspond to the ratio of tags to gaps for triggers (a) and (d), and the ratio of tags to gaps for (b) and (c). From this figure, the p_T spectrum appears the same within error. In Fig. 7.16(b), there might be evidence of a steeper slope for tagged events with gaps

than gaps alone. This tends to support the supposition that the bias towards higher ξ for tagged events requires that the lower momentum fraction component of the Pomeron is being probed in order to preserve the gap.

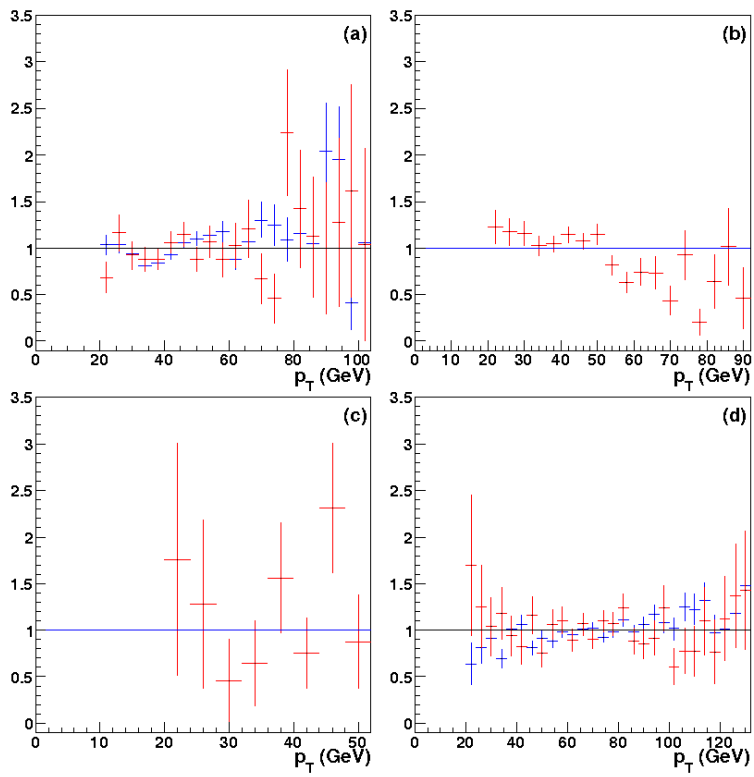

Figure 7.16 Ratio of p_T spectrum for non-diffractive, gap and tag samples in the region of reasonable statistics. Plot (a) corresponds to trigger JT_25TT_NG, (b) to JT_25TT_GapN, (c) to JT_25TT_GapSN, and (d) JT_45TT. The blue points correspond to the ratio of gap to non-gap sample for triggers (a) and (d), the red points correspond to the ratio of tags to non-gap samples for (a) and (d), and the ratio of tags to gaps for (b) and (c). Errors are statistical only.

Finally, the width of diffractive jets is expected to be narrower than the non-diffractive case once again due to less radiation for the diffractive sample. As shown in Fig. 7.17, the different samples show the same basic structure with the gap sample shifted to lower widths.

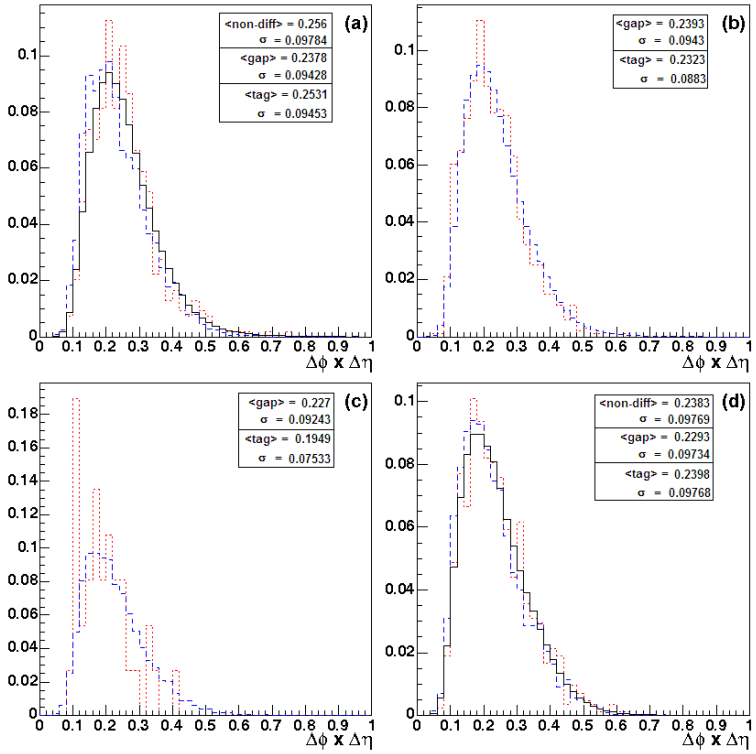

Figure 7.17 Jet width distribution for non-diffractive, gap and tag samples normalized to unit area. Plot (a) corresponds to trigger JT_25TT_NG, (b) to JT_25TT_GapN, (c) to JT_25TT_GapSN, and (d) JT_45TT. The black histogram corresponds to events with no gaps or tags, the blue dashed histogram corresponds to a GapN or a GapSN with or without a tag, and the red dotted histogram corresponds to tags (with or without a gap in the case of (a) and (d)).

The tags in the dipole spectrometer seem to be correctly associated with diffractive dijets possessing the expected properties. Processing these prototracks through the track reconstruction procedure described in Section 5.2.2.2, provides access to the ξ and t distributions of the diffractive events. As shown in Fig 7.18, the ξ distribution is within the region expected for diffraction, $\xi < 0.1$, with most of the events in the region dominated by Pomeron exchange ($\xi < 0.05$). The structure in the distributions is likely attributable to the triggers used in the study. The acceptance of the dipole spectrometer is highest for high ξ events, yet the gap triggers bias the sample towards lower ξ events. The en-

hanced number of gap events in the trigger biases the distribution to lower values of ξ than expected from the cross section alone, leading to what appears to be two different distributions (low-ξ, high-t and high-ξ, low-t). In addition, different operating positions used during the data taking can contribute to structure in these distributions. Final alignment of the spectrometer also needs to be taken into account, which will provide a better measurement of these variables in the future.

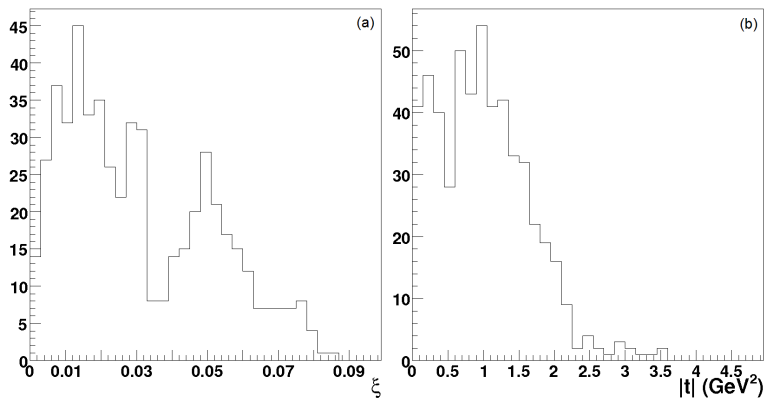

Figure 7.18 Distribution of (a) ξ and (b) t for the tag sample.

Looking at the distribution of ξ vs. t as shown in Fig 7.19 shows that they are related to each other as expected by the acceptance of the dipole spectrometer as shown in Fig. 5.9. Because of the triggers used in the study, the diffractive mass is already small, forcing the selection of events with smaller ξ on average. The observation that these low-ξ events have higher $|t|$ is the result expected from the dipole acceptance. The events with higher ξ have lower t as expected.

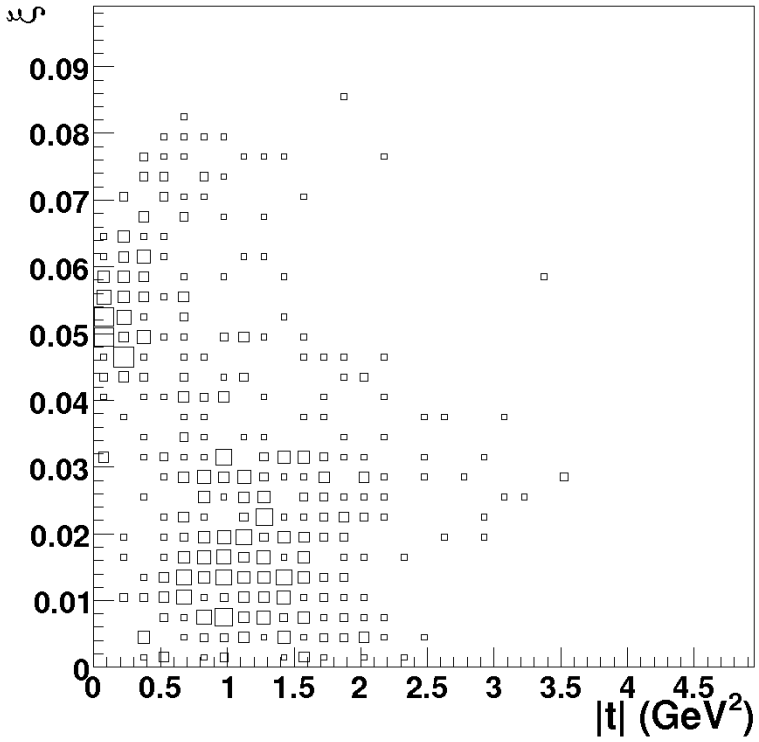

Figure 7.19 ξ vs. t for tag sample.

CHAPTER 8

CONCLUSION

In this dissertation, I have presented the phenomenological groundwork upon which diffractive QCD is currently established. This includes attempts to combine Regge Theory with perturbative QCD through the Ingelman-Schlein model as well as the application of various parton evolution schemes (DGLAP, BFKL, and CCFM). In addition, the Soft Color Model attempts to describe diffractive processes without resorting to Regge Theory.

To explore these various theories, a new detector sub-system was built and integrated with the existing DØ detector. Significant effort was expended in the construction, installation, commissioning and operation of the new Forward Proton Detector, enabling such future measurements. In this dissertation, I have described the DØ detector with a special emphasis on the FPD.

I have presented the basis of the reconstruction algorithm used to analyze data collected by the system, upon which significant effort was also expended. To demonstrate that the dipole spectrometer of the system is working as expected, I have presented a study of dijet events, comparing the properties of such jets in events with no diffractive signature (gap or tag) to those that have either a gap, or a tag, or both. It has been shown that the data being provided by the dipole spectrometer is consistent with that expected in the original design, and that the properties of dijets with gaps and/or tags do exhibit the expected behavior compared to non-diffractive dijets. Diffractive dijets show the expected boost in η away from the gap and/or tag, diffractive events have

fewer jets, the addition of a gap reduces the amount of radiation present in an event, as exhibited in the narrower jets that tend to be more back-to-back, and the p_T spectrum is not significantly different (except perhaps in the case of tagged events with a gap).

This indicates that the dipole spectrometer is providing access to the expected diffractive processes. We have shown that the algorithms are able to reconstruct such tagged events and that the dipole spectrometer is providing access to the expected acceptance region of ξ and t. Future studies using the dipole spectrometer will be able to explore differences between the various phenomenological models used to describe diffractive processes.

APPENDIX A

CONSTRUCTION OF THE FORWARD PROTON DETECTOR

A large fraction of my effort during my graduate studies was spent on the construction, installation and commissioning of the Forward Proton Detector. This included development of the procedures to be used as well as training of others to help in the tasks.

A.1 Position Detector Construction

The first task was the construction of the position detectors. The first step involved quality control of the scintillating fibers and clear waveguide fibers ensuring the integrity of the fibers was maintained through the ice polishing procedure before shipping them to UTA. In addition, manufacture and quality control of the support frames was conducted at Fermilab before shipping the frames to UTA.

With the polished fibers delivered, they were processed through the splicing machine in preparation for being placed in the frames. Considerable effort was spent in establishing the proper parameters to maximize spliced-fiber production. Once the frames were assembled, the final step was to put the appropriate fibers into the proper location of each cookie (as aligned to the notched corner) before securing them with optical epoxy.

The assembled frames were returned to Fermilab, where the the u and v frame inner sides were polished and then attached to the x frame. The fully assembled detector was polished again, both at the active bottom and at the cookie interface in preparation for incorporation in the cartridge base. The checklist used to assemble the fibers in the frames is reproduced on the following pages.

Detector Assembly Procedure

U/V Frame Preparation

1. Choose a good frame.
    a. Look at channels 1 and 20 from an edge view and ensure they are vertical. If not, set frame aside and choose another.
2. Prepare New Frame.
    a. Take frame, aluminum mask and 0.5mm mechanical pencil to marble table.
    b. Place long edge of frame on table with detector active area (gray area on picture) against table and gently push mask against detector.
        i. Gently place graphite from pencil on exposed fins.
            1. Move mask along table until all fins from this orientation are covered.
        ii. Extend line onto bulk of detector as shown in drawings.
        iii. Rotate frame so short edge with detector active area is against table and repeat.
    c. Repeat for other side of frame.
    d. Decide if you are doing a U or V frame. Take blue tape and attach to thin layer separating primed and unprimed planes in the edge view with excess tape towards primed side.
        i. Run edge of screwdriver against tape and detector to ensure good adhesion.
        ii. Cut tape vertically along leading edge and fold tape over the primed fins.
    e. Take double sided tape and tape detector onto table in orientation for U or V shown in picture.
        i. Surround table around detector with clear plastic or Mylar to catch dripping epoxy.
        ii. Place fiber support tray to the right of the detector about 5 inches away.
            1. Place cover over tray.
    f. Create 20 labels (label them U1, U2, U3 … etc. or V1, V2, V3 … etc.) with enough spare so that they can be folded in half and taped around four fibers.

U/V Frame Filling (fill frame from channel 20 to channel 1)

3. Take four fibers from tray.
    a. Align splice points using OptiVisor
    b. Take small piece of blue tape. Attach across the four fibers on the wave-guide side of the splice and fold tape over itself. Tape should only be attached to one side of the fibers.
    c. Take appropriate paper label and fold over fibers. Use a small piece of Scotch tape and secure allowing label to move freely over fibers.
4. Insert fiber bundle into fiber support tray.
    a. Take fiber support cover and lift it up on its left edge and slide along fiber support tray to the right until it is no longer over any fibers. Set aside.
    b. Hold onto paper label and insert wave-guide part of fiber into its appropriate channel at far right side of tray while keeping the scintillating fiber out of the support tray.
    c. Pull fiber through the tray until there is room to place cover on tray. Continue pulling until label is over the left edge of tray. While pulling, slide the cover after to keep all fibers in their appropriate channels.
5. Insert scintillating fiber into frame.
    a. With the splice point between the frame and the tray, gently ease the scintillating fibers into the frame until flush with top of fins.
6. Pull fibers with blue tape until splice point is properly aligned.
    a. To properly align splice point consider a line connecting the low edge of the graphite-covered part of the fins for the channel in question. Make the centerline of the fiber where it intersects the splice points coincide with the graphite line while looking through the OptiVisor.
7. Gently push down on fibers near splice point on wave-guide side until fibers are flush with fins.
8. Apply small drop of superglue near splice point and continue pushing down until glue cures.
9. Repeat from step (3) until frame is filled.
10. Look at instructions for epoxying fibers.
11. After epoxy cures, remove blue tape from fibers and blue tape from frame.
12. Turn frame over and tape to table in the primed orientation as shown in drawing.
13. Place fiber-holding tray over the already filled fibers and slide the paper labels down towards the tray.
14. Create the appropriate primed paper labels (U'1, U'2, U'3 … etc. or V'1, V'2, V'3 … etc.)
15. Repeat from step (3) to step (10)
16. After primed side is cured, remove blue tape from frames and wrap a piece of tape around the end of the wave-guide part of the fibers keeping the primed and unprimed fibers separated.
17. Set detector aside until the cookies can be filled.

Detector Assembly Procedure

X Frame Preparation

1. Choose a good frame.
    a. Look at channels 1 and 16 from an edge view and ensure that they do not narrow near the bottom. Look at the same channels from an overhead view. Look for warping. Slide a fiber through these channels and look for warping. If any of these things are observed, set frame aside and choose another.
2. Prepare New Frame.
    a. Take frame, aluminum mask and 0.5mm mechanical pencil to marble table.
    b. Place edge of detector active area (gray area on picture) against table and gently push mask against detector.
        i. Gently place graphite from pencil on exposed fins.
    c. Repeat for X' side.
        i. Draw line along edge of mask along bulk of frame on side with screw hole as shown in drawing.
    d. Take blue tape and attach to thin layer separating primed and unprimed planes in the edge view with excess tape towards primed side.
        i. Run edge of screwdriver against tape and detector to ensure good adhesion.
    e. Place an old cookie-securing mask under the frame on the table away from you.
    f. Take double sided tape and tape detector onto table in orientation for X shown in picture.
        i. Surround table around detector with clear plastic or Mylar to catch dripping epoxy.
        ii. Place fiber support tray to the right of the detector about 5 inches away.
            1. Place cover over tray.
    g. Create 16 labels (label them X1, X2, X3 … etc.) with enough spare so that they can be folded in half and taped around four fibers.

<u>X Frame Filling</u> (fill frame from top to bottom (1 to 16 for X, 16 to 1 for X'))

3. Take four fibers from tray.
    a. Align splice points using OptiVisor
    b. Take small piece of blue tape. Attach across the four fibers on the wave-guide side of the splice and fold tape over itself. Tape should only be attached to one side of the fibers.
    c. Take appropriate paper label and fold over fibers. Use a small piece of Scotch tape and secure allowing label to move freely over fibers.
4. Insert fiber bundle into fiber support tray.
    a. Take fiber support cover and lift it up on its left edge and slide along fiber support tray to the right until it is no longer over any fibers. Set aside.
    b. Hold onto paper label and insert wave-guide part of fiber into its appropriate channel at far right side of tray while keeping the scintillating fiber out of the support tray.
    c. Pull fiber through the tray until there is room to place cover on tray. Continue pulling until label is over the left edge of tray. While pulling, slide the cover after to keep all fibers in their appropriate channels.
5. Insert scintillating fiber into frame.
    a. With the splice point between the frame and the tray, gently ease the scintillating fibers into the frame until flush with top of fins.
6. Pull fibers with blue tape until splice point is properly aligned.
    a. To properly align splice point consider a line connecting the low edge of the graphite-covered part of the fins for the channel in question. Make the centerline of the fiber where it intersects the splice points coincide with the graphite line while looking through the OptiVisor.
7. Gently push down on fibers near splice point on wave-guide side until fibers are flush with fins.
8. Apply small drop of superglue near splice point and continue pushing down until glue cures.
    a. For X', fill channels 16 and 15 before using glue then proceed as normal
9. Repeat from step (3) until frame is filled.
    a. For X', allow superglue to cure hard in all channel then remove blue tape from fibers.
10. Look at instructions for epoxying fibers.
11. After epoxy cures, remove blue tape from fibers and blue tape from frame.
12. Turn frame over support with cookie-securing mask and tape to table in the primed orientation as shown in drawing.
13. Place fiber-holding tray over the already filled fibers and slide the paper labels down towards the tray.
14. Create the appropriate primed paper labels (X'1, X'2, X'3 … etc.)
15. Repeat from step (3) to step (10)
16. After primed side is cured wrap a piece of tape around the end of the wave-guide part of the fibers keeping the primed and unprimed fibers separated.
17. Set detector aside until the cookies can be filled.

Detector Assembly Procedure

Epoxy Preparation

1. Take a plastic beaker, bottle of hardener, can of resin and a spoon to digital scale.
2. Place beaker on scale and tare.
3. Add 2.5 g of resin to beaker.
4. Add 0.7 g of hardener to beaker (total to 3.2 g)
5. These amounts are sufficient for one frame. Increase in weight proportion for more.
6. Return supplies to clean room.
7. Take beaker and turn spout down until beaker is oriented at about 45 degrees to the vertical.
8. Scrape resin from the bottom of the beaker into the pool of hardener with the tip of a syringe.
9. Thoroughly mix hardener and resin.
10. Allow epoxy to sit for about 10 minutes after mixing to begin to set.

Frame Gluing

11. Pour small amount of epoxy over middle of active area and push to cover all the fibers in the frame that are within the fins. Do not put any epoxy outside of the fins.
12. Gently wiggle each scintillating fiber in the channels to encourage epoxy to filter down into frame.
13. Place a small amount of epoxy over scintillating fibers that are outside of the frame. Spread out over all the fibers and gently wiggle fibers to encourage epoxy to fill in around the fibers.
14. Allow epoxy to seep into the fibers for about 15 to 20 minutes.
15. Repeat the above procedure from step (11) using slightly less epoxy.
    a. For X' Frame:
        i. Get a Trigger Scintillator
        ii. Place some epoxy on the edges of the channel.
        iii. Insert the Trigger Scintillator into the channel and align the pencil mark on the frame with the joint between the scintillating trigger and the wave-guide.
        iv. Push the trigger flush with the frame.
        v. If there are any gaps between the trigger and the frame, put a small amount of epoxy and allow to seep down.
    b. Take flat sheet of plastic covered in Mylar and place edge of wave-guide fibers and lower over the epoxy.
    c. Push down onto frame and place a 100g weight over the plastic.
16. Allow epoxy to cure overnight for ~24 Hrs.
17. Gently remove weight and sheet of Mylar covered plastic.

A.2 Photomultiplier Tube Testing

Following preparation of the scinitillating fiber detectors, the next detector component consists of the photomultiplier tubes used to read out the detectors. The trigger tubes were reused from the Run I Luminosity system while the MAPMTs were purchased from Hamamatsu. Since individual HV channels are responsible for powering multiple tubes, it is necessary to bin the tubes in groups of similar performance.

This was accomplished with a blue/green LMB (Light Mixing Block) used to strobe the tubes with light of a desired intensity. A special cookie was employed that allowed LMB fibers to be directed to different channels of an MAPMT. There was also a trigger cookie that allowed an LMB fiber to be used to strobe the trigger tubes.

Each of the 16 LMB fibers was tested for variation using a reference trigger tube shining the light on the same spot of the photo-cathode. It was found that there was a negligible change in the ADC counts of the tube for each fiber. The same signal and HV cable was used in each test so the only variable was the performance of each tube.

Information was read out through a LeCroy ADC including the PinOut of the LMB. All tests were performed with similar PinOut ADC counts to minimize differences in setup between tubes. A value of 261$\pm$4 counts was used as a reference for trigger tube and 83$\pm$2 counts as a reference for the MAPMTs.

The average channel response was determined for each MAPMT and they were subsequently binned in groups of 7 with similar response. Spare tubes were placed between the bins allowing them to be used in either adjacent bin if needed.

At the same time, MAPMT cross talk was studied by sending light to a single channel and measuring the ADC response in all other channels. This study found light leakage at the level of 2.5% of the ADC count of the strobed channel in the immediate adjacent channels and negligible leakage further out for an optimally aligned MAPMT and cookie. With varying alignment, the crosstalk could increase to 10%.

A.3 Cartridge Construction

With the fully assembled detectors and binned tubes, the next step was to assemble everything together in the aluminum cartridge base and top and install in the tunnel. The aluminum parts were prepped for assembly (*e.g.* smoothing of sharp edges, cleaning) and tested for tolerance.

The cartridge base contains the detector within a small box at the end of a long tube at one end and the cookies at the other. The small box is held within the tub with slow-set silicon rubber to allow for tolerance changes when placing the cartridge base into the castle pot.

To cartridge top contains the photomultipliers. They are aligned with the cookie supports of the matched cartridge base and then held in place with slow-set silicon rubber. This allows for tolerance issues when placing the top over the base and provides for a slight tension to hold the tubes against the cookies. The checklist used in the assembly is reproduced on the following pages.

Cartridge Assembly Procedure

This page provides a description of the procedure to be used to assemble the cartridge that places the detector into the castle. Begin by assembling all necessary parts for one complete cartridge and labelling them in some manner so they stay together. Ensure all parts fit together before doing anything permanent.

The Cartridge consists of three main parts. There is a cartridge tube that protects the fibers and positions the detector in the right place for insertion. The Cartridge itself comes in two parts. The bottom part holds the fiber cookies in place and provides support for the cartridge tube. The top part hold the PMTs. What follows is intended as a check list for all the steps required in assembling the various parts of the cartridge.

Cartridge Base Assembly

- Place Cartridge Bottom (Part 6) against table with lipped edge facing down. The lipped edge will face towards the detector.
- Attach 3 Cartridge Alignment Blocks (Part 7) to Cartridge Bottom.
    - Threaded holes in Cartrige Alignment Blocks face up.
- Prepare Support Ring (Part 8). (CAUTION: Care must be taken while compressing ring due to internal stresses caused by compression. If control of ring is lost, it WILL fly away and can cause damage and injury).
    - Place pins in 1/8" holes nearest break in Support Ring (can tap holes with 6-32 thread and use allen screws to prevent mishaps).
    - Apply pressure with pliers to compress Support Ring together.
        - If Support Ring is unable to compress sufficiently, excess material from broken edge of Support Ring can be removed.
    - Place edge opposite pins into Cartridge Bottom.
    - Lower edge with pins into Cartridge Bottom and push Support Ring until snug against Alignment Blocks.
    - Release pliers and remove pins.
- Insert threaded rods into Alignment Blocks.
- Prepare Support Plate 1 (Part 9).
    - Round the sharp corners of the 7 square sockets.
    - On Plate 1 draw the unique line that bisects an alignment hole, the central PMT hole and one square socket hole.
        - Label the bisected socket hole 5 and in a clockwise manner label other square socket holes 4, 3, 2, 1, 7, 6 (write these numbers on the other side of the Plate as well).
    - Draw a bisecting line on the lipped side of the circular PMT socket that bisects the Pusher Rod holes.
    - Draw a bisecting line on the lipped side of a square socket with the angled corner in the upper left side.
- Insert Plate 1 into Cartridge Bottom with side containing the bisecting line facing down until flush with Support Ring.
    - Socket 5 should align with the Guide Bolt hole on the outside of the Cartridge Bottom and the bisected alignment hole should align with the threaded rod on the opposite side of the Cartridge Bottom.
    - Mark position of 6 securing holes in Plate 1 against inside of Cartridge Bottom and on top of Plate 1.
- Remove Plate 1 and threaded rods.
- Rotate Support Ring until 6 holes in Support Ring are aligned with marks on Bottom Cartridge Case.
- Reinsert Plate 1 and verify holes are aligned.
    - One hole of Plate 1 may be slightly off. Drill a new hole in the proper place.
- Once holes are aligned, insert Guide Bolt through Cartridge Bottom and into Support Ring.
- Temporarily secure Plate 1 to Support Ring with 6 screws.
- Turn over Cartridge Bottom so Plate 1 is towards the table and socket 5 is facing away from you.
- Apply a small amount of white RTV around square socket with the bisecting line near the lip and insert into socket 5 with angled corner in the upper left hand side. Push until snug against Plate.
    - Rotate Cartridge Bottom and apply RTV to remaining square sockets with and insert with angled corner in upper left hand side.

- Apply a small amount of white RTV to round socket near the lip and align bisecting lines with the trigger scintillating hole to the left.
- Insert Optical Connectors into 14 holes in Cartridge Bottom.
    - Place a small amount of black RTV on the threaded side of Optical Connector.
    - Insert Optical Connector into Cartridge Bottom with threads pointing outwards.
    - Secure with lock washer and nut.
- Allow Cartridge Bottom to cure overnight.

Cartridge Top Assembly

Step One

- Place completed Cartridge Bottom with lip facing towards table.
- Wrap MAPMTs with brown mailing tape and cut edge EXACTLY at top and bottom of PMT.
- Start by placing 2 thicknesses of paper onto each edge of the square sockets.
- Place PMT down into socket ensuring that the paper does not slip underneath the PMT.
    - Ensure proper alignment of PMT.
        - Looking at face of PMT, Channel 1 is in the upper left hand side. This channel should be in same corner as angled corner of socket.
- If PMT has any lateral movement, remove it and put an additional thickness of paper on each side of socket.
- Repeat until PMT has no lateral movement.
- Once all PMTs are in place, insert threaded guide bolts into Cartridge Bottom.
- Slide Support Plate 2 (Part 10) over guide bolts and over PMTs.
    - Using three pieces of tape around Cartridge Bottom ensure Plate 2 is concentric with Cartridge Bottom.
- Seal between Plate 2 and PMTs using black RTV.
    - Ensure there are no holes or silicon rubber will leak out.
- Wrap tape around bottom of circular PMT and insert into central hole.
    - Add tape until there is no lateral movement between PMT and socket.
- Seal between Plate 2 and PMT with black RTV.
    - Ensure there are no holes or silicon rubber will leak out.
- Remove alignment tape.
- Place Cartridge Top over Cartridge Bottom ensuring proper alignment of the Guide Bolt until snug.
- Place three long tubes over threaded alignment pins.
- Place black RTV round tubes and Plate 2.
- Allow RTV to cure overnight.

Step Two

- Ensure you are on a level surface.
- Place Cartridge Top and Bottom on level surface.
- Coat short tubes with petrolum jelly and place around Pressure screws.
- Insert Pressure screws into Plate 2.
- Make sure coated tubes are flush against Plate 2 or silicon rubber will leak out.
- Take Prototype Cylinder and attach solid lid to one side. Place lid against level surface.
    - Cover holes in lid with tape on inside.
- Mix Pink Silicon Rubber.
    - Use 10 Parts base (white) to 1 Part catalyst (pink) by weight.
    - For this part mix about 585 g (500 mL.)
- SLOWLY pour silicon rubber down onto plate 2 around the PMTs. Make sure Silicon Rubber is not leaking out.
- Continue to pour until silicon rubber is EXACTLY level to upper surface MAPMTs without flowing over.
- Pour remaining silicon rubber into Prototype Cylinder to make a sheet about 3mm thick.
- Allow silicon rubber to cure AT LEAST overnight, preferably longer (~24 hrs).
- Remove Cartridge Top from Bottom and remove papers.

Step Three

- Remove lid from Prototype Cylinder and pull silicon rubber sheet free.
- Place Support Plate 3 (Part 11) over sheet.
- Cut holes out of rubber sheet using Plate 3 as template.
- Remove Pressure screws and sleeves from Plate 2.
- Place rubber sheet over PMTs.
- Place Plate 3 over rubber sheet.
- Insert Pressure screws and screw Plate 3 down over PMTs. The Pressure screws can be used to ensure PMTs are snug against cookies when entire cartridge is assembled.

Step Four

- Wire HV Splitter for PMTs.
  - HV terminal is towards outside of Cartridge Top and ground is towards inside.
- Put female pins on HV cable end and cover pin with heatshrink tube.
- Remove about 2cm of wire mesh from each cable.
- Put heatshrink below mech to hold cable together.
- Put a single piece of wire and twist 7 leads around it and tie all wire mesh together
- Solder piece of wire into BNC connector with ground to mesh
- Attach base to L0 PMT
- Attach BNC connectors to L Bracket
- Attach L bracket to Cartridge Top
- Pass cables through top lid opening.
- Attack output cables to MAPMTs
- Group output cables together flat against each other
- Pass cables through secure mounting
- Attack secure mounting to side of Cartridge Top
- Pass cables through Cartridge Lid Top (Part 13)
- Attach Cartridge Lid Top to Cartridge Top

Cartridge Tube Assembly

Step One

- Label cookies on the Detector:
  - Looking at bottom of detector the planes are as follows: U, U', X, X', Trigger, V, V'.
    - The numbering of the 7 cookies is:
      - U = 1, U' = 2, V = 3, V' = 4, X = 5, X' = 6, U/V mixed = 7
- Insert Detector into Detector Case (Part 1).
  - Secure with screws.
- Screw Pusher Rods (Part 3) into X Frame of detector.
  - Secure with epoxy.
- Fill in corners of jig with modeling clay.
- Coat inside of jig with petrolium jelly.
- Remove screws from detector case.
- Place jig over detector with Detecor Case passing through hole in center of jig.
- Rest jig on spacer and push detector down until it is flush with level surface.
- Place Cartridge Tube (Part 2) down into jig until snug.
  - Make sure upper edge of Cartridge Tube has been rounded.
- Rotate Cartridge Tube until cutouts are perpendicular to Detector Case.

- Fill inside of Cartridge Tube with Pink silicon rubber until even with top of Detector Case.
- Allow to cure overnight to 24 hours

Step Two

- Remove jig from Cartridge Tube and from Detector Case. Reattach screw to case.
- Remove silicon rubber from cutouts of Cartridge Tube.
- Remove Plate 1 from Cartridge Bottom.
- Screw Cookies into Plate 1. Make sure trigger scintilar and pusher rod goes into the right holes.
    - Round off sharp edges of free part of socket.
    - Insert the appropriate cookie into the appropriate socket.
    - Secure with screw, washers and nuts screwing from top to bottom.
    - Make sure washers are as far in as possible.
- Pass Cartridge Tube through Cartridge Bottom with detector toward the bottom.
- Align Cartridge Bottom with Plate 1 and screw into place.
- Attach small LMB fibers to closest Optical Couple.
- Place Cartridge Collar (Part 4) into Cartridge Lid Bottom.
- Pass Cartridge Tube through Lid bottom and Collar with Collar towards the detector.
- Pull tube until small lip is flush with Collar and screw Collar against tube.
- Screw Lid into Cartridge Bottom.
- Ensure Cartridge Top fits over Cartridge Bottom and there is slight resistance due to cookies being flush against PMTs.

Cartridge Assembly into Pot

- Ensure the Cartridge Tube is aligned with the collar.
    - Tighten the four set screws and light guide faces should be parrallel to faces on the central socket hole.
- Prepare the end of the four 5/16" collar screws. The diameter should be reduced to 6mm at the end removing about 1cm of the thread.
- Make sure the remaining thread is clean and the screws can be attached to the collar by hand.
- Attach the long rods with threaded ends to the alligment pins on the pot. Pay attention to the treads THEY ARE DIFERENT! the 4mm diameter end will match the thread in the pot. BE CAREFULL NOT TO TOUCH THE WINDOW.
- Slide the bottom part (with the detector) of the cartridge only using the rods as a guide. Push the tube carefully and make sure of the correct side the particles will hit the detector. Push the tube until the cartridge collar fits the pot collar.
- You should see if the lateral notches on pot collar are alligned with the lateral holes on cartidge collar. If they are, attach the screws. If not, pull back the tube about 5cm and turn the pot collar to the correct position (you must loose two screws on the pot collar to do this adjustment). Push the tube again and attach the lateral screws.
- Put the cylindrical nuts on the rod end. Do not overtighten, use enough torque to make sure the detector is pressed against the window
- Attach the cartridge top and use three 1/4" washers and wingnuts to hold it in place.

A.4 Detector Geometry

The final step was to use the experience in assembling the detectors to help determine the actual fiber alignment in the detectors. An optical scanning method was attempted but was found to give unreliable results. However, it was clear from the attempt that there were alignment issues with the assembly of the detector. This was confirmed when the standalone system first started providing data and the PD spectrometer was examined. It was found that the hit resolutions and segment occupancies were not as expected, as shown in Fig. A.1.

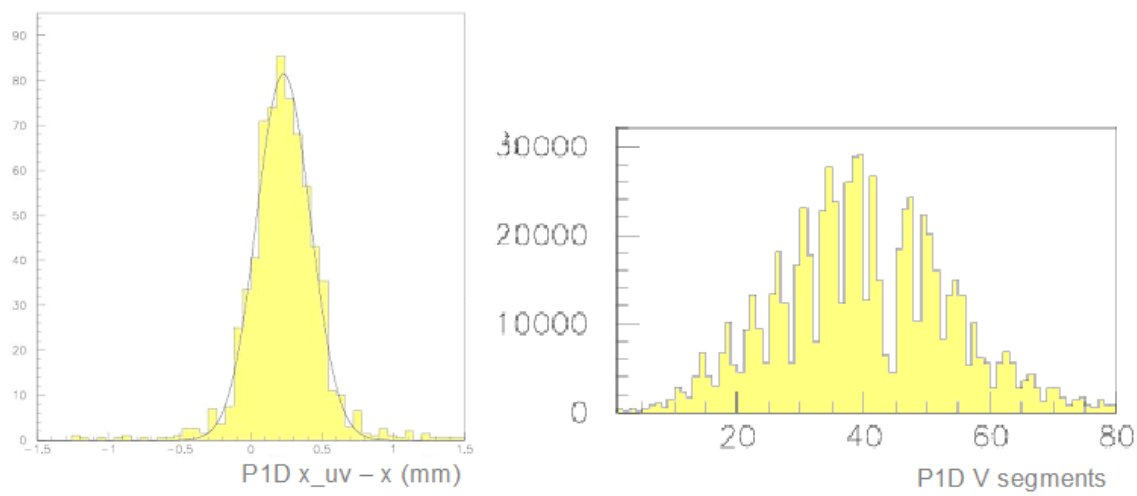

Figure A.1 Raw hit resolution (left) and segment occupancy (right) for the PD spectrometer standalone data.

This can be explained by shifts in the frames relative to one another (causing the shift in the hit resolution) and shifts between the layers within a plane (leading to structure in the segment occupancy as the size of the segments depends on the shift between layers). Therefore, the measurements of the actual components used in the construction of the detectors compared to the design drawings was used to arrive at an ideal drawing geometry and the ability to add corrections was included and a methodology

established to find modified geometry files to be used in reconstruction. The short note describing the corrections is reproduced on the following pages.

Detector Geometry and Alignment

All segment measurements are made in the native geometry of the frame (U, V, X). The actual hit coordinates are made in the detector (x,y) coordinate system where (v,u) is rotated 45 degrees with respect to (x,y). The origin is then shifted as determined by the active area of the detector, which is defined in the x direction as the area where at least 2 frame active areas overlap. In the y direction it is fixed at 17.39mm because of the way the detectors are constructed.

In my variable names, if I have (uvx) that means there can be a unique measurement for each value in parenthesis.

Native Fiber Geometry

In a detector frame, we have two planes. One plane is shifted with respect to the other and I call this the prime shift. Looking at the detector from the U side, the leading plane (the one for which fiber 1 defines the edge of an active area we have) is U', X and V. As an example, using the X frame:

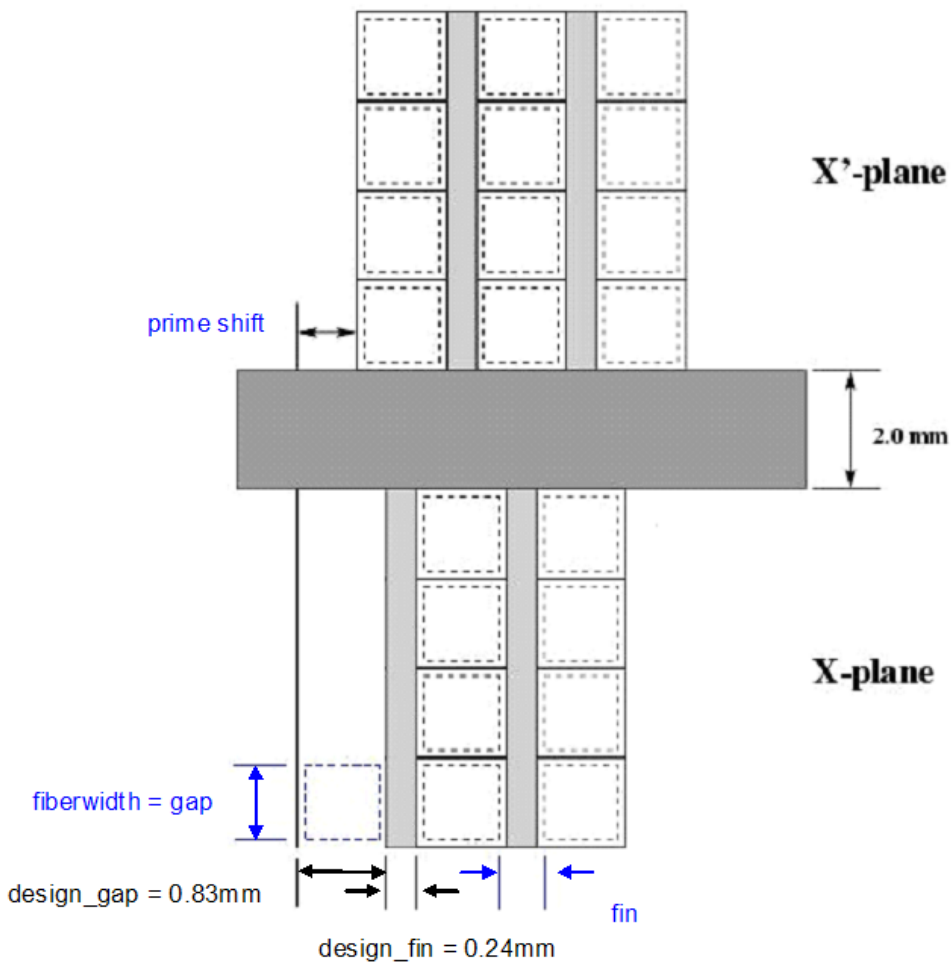

From the final drawing of the detector, a gap is defined as design_gap = 0.83058mm, a fin is design_fin = 0.23876mm and the prime shift is design_(uv)_pshift = 0.54061mm for the U/V frame and design _x_pshift = 0.54102 for the X frame.

In reality, a smaller fiber is placed in every groove. We will assume that the fibers are aligned in the center of each groove. From this, we are able to determine a final gap and fin using the formulas:

(uvx)_gap = (uvx)_fiberwidth
(uvx)_fin = design_fin + design_gap – (uvx)_fiberwidth

From the drawing, the native active area can be found using the formula:

(uv)_active = 20 * (uv)_gap + 19 * (uv)_fin + (uv)_pshift
xi_active = 16 * x_gap + 15 * x_fin + x_pshift

Where a U/V frame has 20 channels and an X frame has 16 channels. Using the initial design values, we get design_x_active = 17.4117mm and design_uv_active = 21.68865mm.

Because the fiber is smaller than the design_gap, there is a slight offset from the edge of the frame (the initial origin of the (x,y) coordinate system), and the beginning of the first fiber. The value of the offset is given by:

(uvx)i_offset = (design_gap – fiberwidth) / 2

This offset doesn't affect the prime shift, since it occurs in both planes of a frame. This offset will be later corrected for frame alignment.

With this information, we can determine segment widths. To do so, you just start at the edge of the leading fiber and you will get:

(uvx)_seg1 = (uvx)_pshift
(uvx)_seg2 = (uvx)_gap – (uvx)_pshift
(uvx)_seg3 = (uvx)_fin
(uvx)_seg4 = (uvx)_pshift – (uvx)_fin
(uvx)_seg5 = (uvx)_fin
…
repeat segments 2-5 until you reach the end (63 segs for X, 79 segs for U/V)
…
x_seg63 = x_pshift
(uv)_seg79 = (uv)_pshift

Now all that is left is to determine where the leading segment edge starts with respect to its natural coordinate system by defining a final offset.

UV Frames

Looking at a U/V frame in the (x,y) coordinates, we have a short side and a long side that is polished. The corner where they meet is important in determining the locations of the fibers in the final (x,y) coordinates.

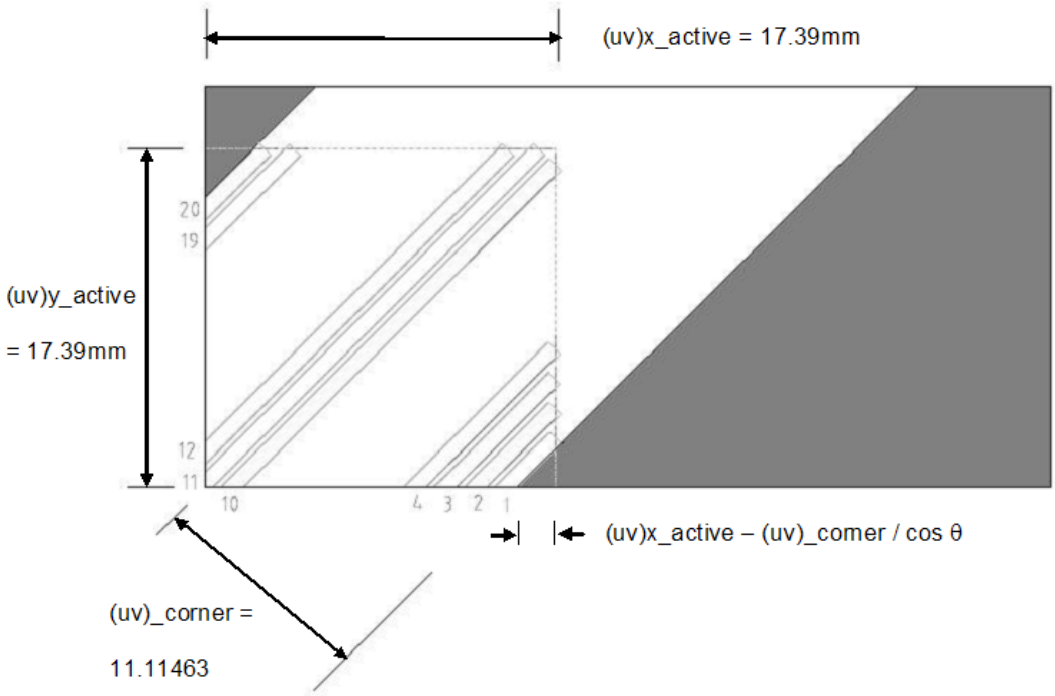

Frame Alignment

When a detector is assembled, the U and V frames are attached to the X frame through screws and a stabilizing fin to prevent rotation. Because of the way the detector is assembled, the active areas of the various frames do not all line up exactly the same. To account for this in the calculations, using the optical scanner, the distance from the x frame edge (initial x_0 is defined as the edge of the physical frame closest to the leading edge of the fiber in the first channel of the X plane) to the short edge of the U and V frames.

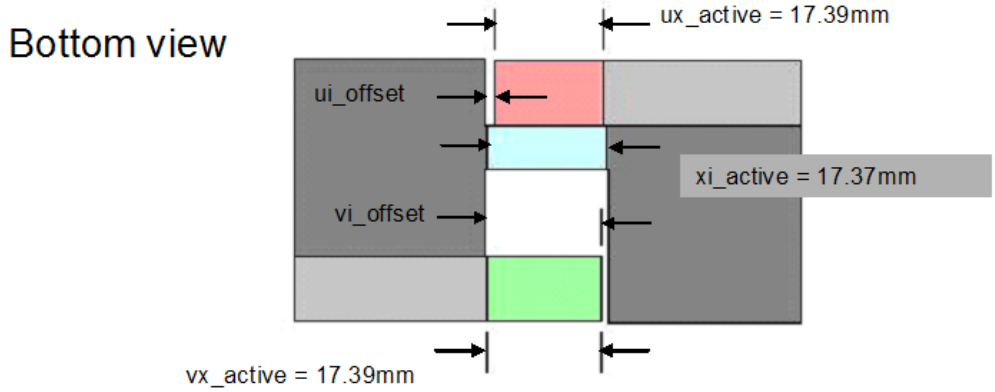

The value for xi_active is determined by adding up all of the fiberwidths and fins for the particlar geometry. Using 0.78 fibers gives the value in the picture.

Determine actual x_active

To determine the actual active area for a detector, we require that two of the three possible active areas overlap. y_active is defined at 17.39mm because of the way the detectors are constructed. Using the xi_active value and the measure (uv)i_offset values, we can determine where the two active area overlap starts and stops.

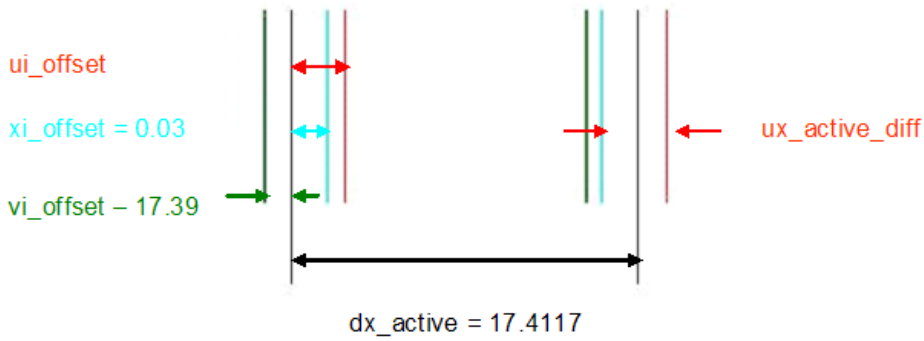

If you lay the active areas one on top of the other, you get a picture like the one above. The black lines are the limits imposed by the physical x-frame, the blue lines are the limits of the xi_active area, the red lines are the u active area limits (17.39mm by definition) and the green lines are the v active area limits. xi_offset is determined by the size of fibers used and is the distance from the physical x-frame to the leading edge of the first fiber in the X plane. For 0.78mm fibers, this becomes 0.03mm

The distance of all of these lines is measured with respect to the original x_0 defined by the x-frame. If you then order the distances from lowest to largest, the one in the middle is the place where two active areas first overlap. This line becomes the final x_0 and all of the offsets are shifted so that this corresponds to 0. Then to determine the far edge, take all of the modified offsets, and add the initial active width (xi_active or 17.39). Once again take the value that is in the middle and this becomes x_active. The distance from the active edge to the u frame active area is needed to final alignment and is called ux_active_diff.

Conversion from (v,u) coordinates to (x,y) coordinates

To convert from one coordinate system to the other, the (v,u) coordinate system is rotated by 45 degrees and shifted by one-half of the final x_active width in both the x and y directions.

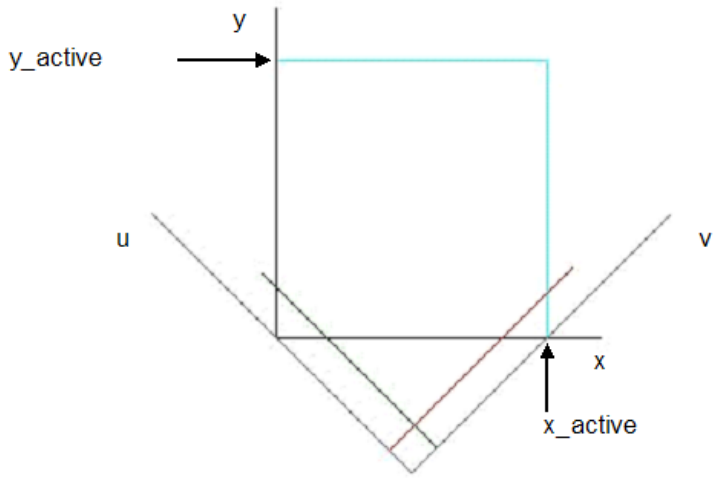

The red line represents where the U active area begins with respect to its coordinate system and the green line represents the same for the V active area.

Then using the rotation matrix, you can convert from one coordinate system to the other.

$$\begin{pmatrix} x \\ y \end{pmatrix} = \begin{pmatrix} \cos\theta & -\sin\theta \\ \sin\theta & \cos\theta \end{pmatrix} \begin{pmatrix} v \\ u \end{pmatrix} + \begin{pmatrix} x_active/2 \\ -x_active/2 \end{pmatrix}$$

Now all that remains is to find out where the segments for U and V start with respect to their coordinate system.

U/V Fiber Offset

Starting with (uv)x_active – (uv)_corner / cos θ (for current geometry this is 1.68mm) we can use simple trigonometry to find this offset:

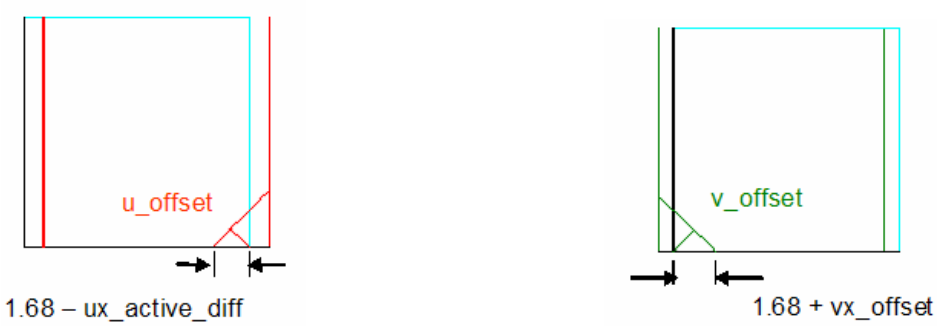

Then using these new numbers multiply by cos θ to get the final offset.

Tying it all together

Once all of these numbers are determined for your particular geometry, to reconstruct an (x,y) from segments you start by determining what segments correspond to the fiber hits you have. From this, you can determine where the edges of that segment are with respect to the native coordinate system including appropriate offsets.

Determine the centerline of all segments. Putting the segments into the rotation equation allows you to convert from (v,u) to (x,y) or through rearranging the resultant equations you can us x and u or x and v to get a y keeping the value from the x segment to get an (x,y).

APPENDIX B

OPERATION OF THE FORWARD PROTON DETECTOR

As explained in Section 4.1, each position detector can be independently moved in order to bring it close to the beam. This requires that a trained person (*shifter*) be available to insert the pots once the beam conditions have stabilized at the appropriate instantaneous luminosity. The training involves learning the FPD software that controls pot insertions, how to monitor beam conditions during the insertion and how to respond to the changing conditions as pots are being moved. Of primary importance is ensuring the safety of all subsystems as the pots are moving close to the beam to prevent any inadvertent loss of the beam.

B.1 Checklist

To maximize the safety and repeatability of the pot insertion procedure, a detailed website [113] is maintained that contains a checklist of all steps to be followed during an insertion as well as instructions on the use of the software and emergency response procedures. During training, each individual is required to undertake several training shifts with an expert, observing insertions and asking questions. After a few such insertions, the new trainee takes over, with an expert watching, until both the expert and trainee feel confident that the new individual can handle solo insertions. The first few sets of such insertions are held when other experts are easily available in case of problems.

The online website is based on the physical checklist that is filled out by the shifters during each insertion. It is reproduced on the following pages.

18 pot Run Checklist

Everyone should fill out the lines in black. Fill out the lines in blue if inserting pots and starting data, lines in green if retracting.

Person on Shift: _____ Time / Date (pots in/out): _____

!!!!!!IF AT ANY TIME THERE IS A PROBLEM, TURN OFF ALL CONTROL LINES!!!!!!

- ❑ Log in to elog book and read runplan on the web
- ❑ Read last 8 days worth of FPD entries in elog book (or last entry at a minimum)
  - o open in web browser, unselect INCLUDE_ALL, select FPD, change hours to days.
- ❑ Be familiar with emergency procedures to use during pot motion (see online checklist)
- ❑ Read FPD Issues (http://d0server1.fnal.gov/users/strang/web/fpd/documents/FPDIssues.txt)
- ❑ Verify software is running: ___Pot Motion, ___HV, ___rate watcher, ___SES alarm display, ___rack environment alarm monitor, ____ A/S on
- ❑ Verify that ACNET is setup properly: ___FTP, ___C72, ___D44, ___Lumberjack.
- ❑ Verify there are no alarms in the SES display. If there are, attempt to clear them.
- ❑ Turn on HV to all ____L0 tubes to 100% (verify trigger is using generator signal if rates not updating)
- ❑ Look over examine plots for anything unusual. If there is, make a screen capture and place in elogbook
- ❑ Create screen capture of D44 lumberjack screen showing normal rates for last store and put in elogbook.
- ❑ Create a screen capture of the fpd_run_state page (http://www-d0online.fnal.gov/fpd_run_state/) showing luminosity, singles rates and halo rates and put in elogbook. If this page isn't accurate, contact Vladimir Sirotenko and make copies of the Beams division page, halo rates from C72 and the FPDGui instead.
- ❑ Verify with captain that the beam spot at D0 has not significantly changed
- ❑ Open expert mode of FPDGui.
- ❑ Have Shift Captain notify MCR and CDF that we are going to insert pots
- ❑ Setup camera to display dipole motors.
- ❑ Setup D44 to display rates for dipole pots.
- ❑ Turn on drivers in Pot Motion Software for dipole castle
- ❑ Turn on A side control line.
- ❑ Insert dipole pots to closest possible position using provided insertion tables. Keep track of final position and reason for stopping for logbook. Stop if CDF ahalo more than doubles.
- ❑ Turn off dipole drivers
- ❑ Turn on HV to dipole _____(time) MAPMTs to 100%. Keep track of when this is done for logbook.
- ❑ Setup camera to display A vertical / horizontal motors.
- ❑ Setup D44 to display A vertical rates and calculate a 10% increase of starting phalo rate for stopping condition (10kHz max)
- ❑ Turn on drivers in Pot Motion Software for A1 and A2
- ❑ Insert A-side vertical pots to closest possible position using provided insertion tables. Keep track of final position and reason for stopping for logbook. Stop if CDF ahalo more than doubles.
- ❑ Setup D44 to display A horizontal rates and calculate 20% increase of starting phalo rate for stopping condition (10kHz max)
- ❑ Insert A-side horizontal pots to closest possible position using provided insertion tables. Keep track of final position and reason for stopping for logbook. Stop if CDF ahalo more than doubles.
- ❑ Turn off A1 and A2 drivers
- ❑ Turn off A side control line
- ❑ Turn on HV to A-side _____ (time) MAPMTs to 100%. Keep track of when this is done for logbook.
- ❑ Setup camera to display P vertical / horizontal motors (iris off A side cameras first).
- ❑ Setup D44 to display P vertical rates and calculate 10% increase of starting ahalo rate for stopping condition (6kHz max)

- Turn on drivers in Pot Motion Software for P1 and P2
- Turn on P side control line.
- Insert P-side vertical pots to closest possible position using provided insertion tables. Keep track of final position and reason for stopping for logbook.
- Setup D44 to display P horizontal rates and calculate 20% increase of starting ahalo rate for stopping condition (6kHz max)
- Insert P-side horizontal pots to closest possible position using provided insertion tables. Keep track of final position and reason for stopping for logbook.
- Turn off P1 and P2 drivers
- Turn off P side control line
- Turn on HV to P-side _____(time) MAPMTs to 100%. Keep track of when this is done for logbook.
- Close Expert mode of FPDGui.
- Iris off the P side cameras
- Setup D44 to display scalers for D2I, A2U, P2U, P1I (set upper limits to 400000)
- Make screen capture of this D44 window and put in elogbook.
- Start the examine program
- Record current D0 runnumber: _____ in elog book.
- Place all final position, HV on and any other observation information of insertion in elogbook using the table.
- Send mail to d0fpd_local@fnal.gov with a summary of the insertion.
- Notify shift captain that pots have been inserted.
- Inform non expert of tasks for which they are responsible:
  - Monitor Rates: In Lumberjack. Should be decaying with time. Gradual oscillations are ok, if spikes check tubes. If sustained increase or numerous spikes or anything else strange, page expert. Check every 30 minutes or so.
  - Monitor Alarms: Page expert if there are any LVPS or HV alarms (major or minor) or any major alarms in SES display
  - Rescrape: If there is a rescrape of beam, check with MCR if it is minor or major. For minor rescrape, do nothing special. Keep an eye on rates and trips. Major rescrape ramp down both MAPMT and trigger and ramp back to 100% when done.
  - Put pots into full standby 15 minutes before end of store or after loss of beam using green items below
- Name of Person Removing Pots_____ Time Removed _____
- At 15 minute EOS warning, turn HV to MAPMT tubes to standby (0%)
  - In HVGui, select MAPMT tab then Set HV ->click on Standby -> press ramp button
- Turn on A side and P side control line (located above FPD console). Red lights will come on. You will see a major alarm.
- Return pots to home using Pots Home ->click on Init in main FPDGui screen. Verify that all pots are actually moving home before doing anything else (all bars yellow, sliders moving left, LVDT values getting smaller). If not, turn off control lines and call expert.
- Check for any alarms (other than alarm caused by turning on control line)
- Verify all pots at home (drivers will turn off and all bars will turn blue in FPDGui).
- **TURN OFF ALL CONTROL LINES (located above FPD console). Red lights will turn off. Major alarm will clear.**
- Turn HV to Trigger tubes to standby (0%).
  - In HVGui, select Trigger tab then select Set HV ->click on Standby -> press ramp button
- Record current D0 Runnumber: _____ in elog book.

Last Updated: 22/February/05

B.2 Pot Positions

The procedure used to find the final operating positions begins by moving each pot individually to establish the positions where either the rate begins to increase exponentially (for dipole pots) or where the halo increase as measured at DØ reaches the agreed upon limit (2.5% per pot).

Once these positions are determined, the beam position is estimated by assuming that the beam that is correlated with the halo increase is centered on the matched positions of opposite pots (proton beam for A-side pots and antiproton beam for P-side pots). The ideal lattice helix is then used to find the expected location of the other beam. The pot positions are then combined with the survey information to determine the distance of the pot from the beam of interest (antiproton beam for A-side pots and proton beam for P-side pots) in terms of the appropriate beam σ. Pots within a spectrometer need to be inserted to matched sigmas, so the most restrictive sigma value between the two is used to find the operating positions for both. These final values are used in the pot inserted tables as shown on the following page.

1-Feb-05							
Dipoles							
I sigma	15.4		13.4		12.4		11.4
D1I	30.50	31.27	32.05	32.44	32.82	33.21	33.60
D2I	27.88	28.58	29.29	29.64	29.99	30.34	30.69
A Vertical							
U sigma	14.6		12.6		11.6		10.6
A1U	26.45	27.49	28.52	29.04	29.56	30.08	30.60
A2U	30.12	30.93	31.73	32.14	32.54	32.94	33.35
A1D	30.97	32.01	33.04	33.56	34.08	34.60	35.11
A2D	32.22	33.03	33.83	34.23	34.64	35.04	35.44
D sigma	14.2		12.2		11.2		10.2
A Horizontal							
I sigma	15.9		13.9		12.9		11.9
A1I	11.14	12.97	14.81	15.72	16.64	17.56	18.48
A2I	14.74	16.28	17.83	18.60	19.37	20.14	20.91
A1O	16.09	17.92	19.75	20.67	21.59	22.50	23.42
A2O	21.82	23.36	24.90	25.67	26.44	27.21	27.98
O sigma	16.0		14.0		13.0		12.0
P Vertical							
U sigma	12.8		10.8		9.8		8.8
P1U	20.66	22.52	24.37	25.30	26.23	27.15	28.08
P2U	23.87	25.42	26.97	27.74	28.52	29.29	30.07
P1D	18.54	20.39	22.25	23.18	24.10	25.03	25.96
P2D	21.22	22.77	24.33	25.10	25.88	26.65	27.43
D sigma	12.9		10.9		9.9		8.9
P Horizontal							
I sigma	17.3		15.3		14.3		13.3
P1I	26.48	27.50	28.53	29.04	29.55	30.06	30.57
P2I	29.31	30.11	30.92	31.32	31.72	32.12	32.52
P1O	24.32	25.34	26.36	26.87	27.38	27.90	28.41
P2O	30.48	31.29	32.09	32.49	32.89	33.29	33.69
O sigma	17.5		15.5		14.5		13.5

REFERENCES

[1] S. Narison, *QCD as a Theory of Hadrons: From Partons to Confinement*, 2nd ed. (Cambridge University Press, Cambridge, MA, 2004).

[2] P. D. B. Collins, *An Introduction to Regge Theory and High-Energy Physics* (Cambridge University Press, Cambridge, MA, 1977).

[3] DØ, B. Abbott *et al.*, Phys. Lett. **B531**, 52 (2002), hep-ex/9912061.

[4] J. H. Jackson, *Classical Electrodynamics*, 2nd ed. (Wiley, New York, NY, 1975).

[5] S. Mandelstam, Phys. Rev. **112**, 1344 (1958).

[6] M. Froissart, Phys. Rev. **123**, 1053 (1961).

[7] A. Martin, Nuovo Cim. **A42**, 930 (1965).

[8] K. Goulianos, Phys. Rept. **101**, 169 (1983).

[9] A. G. Brandt, *Jet Measurements at the CERN Collider and the Pomeron Structure*, PhD thesis, University of California, Los Angeles, 1992, (Unpublished).

[10] K. M. Mauritz, *Hard single diffraction in $p\overline{p}$ collisions at 1800 and 630 GeV center of mass energies*, PhD thesis, Iowa State University, 1999, (Unpublished).

[11] L. R. Coney, *Diffractive W and Z Boson Production in $p\overline{p}$ Collisions at $\sqrt{s} =$ 1800 GeV*, PhD thesis, Notre Dame University, 2000, (Unpublished).

[12] T. Edwards, PhD thesis, University of Manchester, (In Preparation).

[13] G. F. Chew and S. C. Frautschi, Phys. Rev. Lett. **7**, 394 (1961).

[14] F. Bigiel, *Search for Exclusive Photoproduction of $\omega - \phi$ Vector Meson Pairs at HERA*, PhD thesis, University of Heidelberg, 2004, (Unpublished).

[15] I. Pomeranchuk, Sov. Phys. JETP **7**, 499 (1958).

[16] A. Donnachie and P. V. Landshoff, Phys. Lett. **B296**, 227 (1992), hep-ph/9209205.

[17] A. Donnachie and P. V. Landshoff, Nucl. Phys. **B231**, 189 (1984).

[18] P. Desgrolard, M. Giffon, E. Martynov, and E. Predazzi, Eur. Phys. J. **C16**, 499 (2000), hep-ph/0001149.

[19] A. Donnachie, CERN Courier **39**, 499 (April 1999).

[20] E710, N. Amos *et al.*, Phys. Rev. Lett. **68**, 2433 (1992).

[21] CDF, F. Abe *et al.*, Phys. Rev. **D50**, 5550 (1994).

[22] D. H. Perkins, *Introduction to High Energy Physics*, 3rd ed. (Addison-Wesley, Reading, MA, 1987).

[23] I. Aitchison and A. Hey, *Gauge Theories in Particle Physics*, 2nd ed. (Institute of Physics, Philadelphia, PA, 1996).

[24] Particle Data Group, S. Eidelman *et al.*, Phys. Lett. **B592**, 1 (2004).

[25] V. N. Gribov and L. N. Lipatov, Sov. J. Nucl. Phys. **15**, 438 (1972).

[26] L. N. Lipatov, Sov. J. Nucl. Phys. **20**, 94 (1975).

[27] G. Altarelli and G. Parisi, Nucl. Phys. **B126**, 298 (1977).

[28] Y. L. Dokshitzer, Sov. Phys. JETP **46**, 641 (1977).

[29] E. A. Kuraev, L. N. Lipatov, and V. S. Fadin, Sov. Phys. JETP **44**, 443 (1976).

[30] E. A. Kuraev, L. N. Lipatov, and V. S. Fadin, Sov. Phys. JETP **45**, 199 (1977).

[31] I. I. Balitsky and L. N. Lipatov, Sov. J. Nucl. Phys. **28**, 822 (1978).

[32] M. Ciafaloni, Nucl. Phys. **B296**, 49 (1988).

[33] S. Catani, F. Fiorani, and G. Marchesini, Phys. Lett. **B234**, 339 (1990).

[34] S. Catani, F. Fiorani, and G. Marchesini, Nucl. Phys. **B336**, 18 (1990).

[35] G. Marchesini, Nucl. Phys. **B445**, 49 (1995), hep-ph/9412327.

[36] B. Andersson, G. Gustafson, and J. Samuelsson, Nucl. Phys. **B467**, 443 (1996).

[37] B. Andersson, G. Gustafson, H. Kharraziha, and J. Samuelsson, Z. Phys. **C71**, 613 (1996).

[38] G. Ingelman and P. E. Schlein, Phys. Lett. **B152**, 256 (1985).

[39] A. Donnachie and P. V. Landshoff, Phys. Lett. **B191**, 309 (1987), [Erratum-ibid. **B198** 590 (1987)].

[40] F. E. Low, Phys. Rev. **D12**, 163 (1975).

[41] S. Nussinov, Phys. Rev. Lett. **34**, 1286 (1975).

[42] A. Donnachie and P. V. Landshoff, Nucl. Phys. **B303**, 634 (1988).

[43] A. Brandt *et al.*, Nucl. Instrum. Meth. **A327**, 412 (1993).

[44] UA8, R. Bonino *et al.*, Phys. Lett. **B211**, 239 (1988).

[45] UA8, A. Brandt *et al.*, Phys. Lett. **B297**, 417 (1992).

[46] http://www-zeus.desy.de/.

[47] http://www-h1.desy.de/.

[48] ZEUS, M. Derrick *et al.*, Phys. Lett. **B356**, 129 (1995), hep-ex/9506009.

[49] H1, T. Ahmed *et al.*, Nucl. Phys. **B435**, 3 (1995).

[50] P. Bruni and G. Ingelman, Phys. Lett. **B311**, 317 (1993).

[51] http://www-cdf.fnal.gov.

[52] CDF, F. Abe *et al.*, Phys. Rev. Lett. **78**, 2698 (1997), hep-ex/9703010.

[53] CDF, T. Affolder *et al.*, Phys. Rev. Lett. **84**, 5043 (2000).

[54] http://www-d0.fnal.gov.

[55] DØ, V. M. Abazov *et al.*, Phys. Lett. **B574**, 169 (2003), hep-ex/0308032.

[56] H1, T. Ahmed *et al.*, Nucl. Phys. **B429**, 477 (1994).

[57] D0, S. Abachi *et al.*, Phys. Rev. Lett. **72**, 2332 (1994).

[58] K. Goulianos and J. Montanha, Phys. Rev. **D59**, 114017 (1999), hep-ph/9805496.

[59] L. P. A. Haakman, O. V. Kancheli, and J. H. Koch, Phys. Lett. **B391**, 157 (1997), hep-ph/9610528.

[60] A. Donnachie and P. V. Landshoff, Phys. Lett. **B437**, 408 (1998), hep-ph/9806344.

[61] A. Edin, G. Ingelman, and J. Rathsman, Phys. Lett. **B366**, 371 (1996), hep-ph/9508386.

[62] A. Edin, G. Ingelman, and J. Rathsman, Z. Phys. **C75**, 57 (1997), hep-ph/9605281.

[63] J. Rathsman, Phys. Lett. **B452**, 364 (1999), hep-ph/9812423.

[64] http://www.fnal.gov/pub/about/whatis/history.html.

[65] http://www.fnal.gov/pub/inquiring/physics/index.html.

[66] http://www-numi.fnal.gov.

[67] http://www-boone.fnal.gov.

[68] W. R. Innes *et al.*, Phys. Rev. Lett. **39**, 1240 (1977), [Erratum-ibid. **39**, 1640 (1977)].

[69] DØ, S. Abachi *et al.*, Phys. Rev. Lett. **74**, 2632 (1995), hep-ex/9503003.

[70] CDF, F. Abe *et al.*, Phys. Rev. Lett. **74**, 2626 (1995), hep-ex/9503002.

[71] KTeV, A. Alavi-Harati *et al.*, Phys. Rev. Lett. **83**, 22 (1999), hep-ex/9905060.

[72] DONUT, J. Sielaff *et al.*, (2001), hep-ex/0105042.

[73] http://www.fnal.gov/pub/about/whatis/timeline.html.

[74] http://www-bd.fnal.gov/public/chain.html.

[75] A. Melnitchouk, *Search for non-SM Light Higgs Boson in the $h \to \gamma\gamma$ channel*, PhD thesis, Brown University, 2004, (Unpublished).

[76] S. Fatakia, *A Measurement of the Mass of the Top Quark in the Di-lepton Channels Using the DØ Detector at Fermilab*, PhD thesis, Boston University, 2005, (Unpublished).

[77] J. D. Cockroft and E. T. S. Walton, Nature **129**, 242 (1932).

[78] D. Mohl, G. Petrucci, L. Thorndahl, and S. Van Der Meer, Phys. Rept. **58**, 73 (1980).

[79] F. Blekman, *Top quark pair production in proton antiproton collisions*, PhD thesis, University of Amsterdam, 2005, (Unpublished).

[80] http://www-d0.fnal.gov/collaboration/Map/D0_Map.gif.

[81] DØ, S. Abachi *et al.*, Nucl. Instrum. Meth. **A338**, 185 (1994).

[82] DØ, V. M. Abazov *et al.*, (In Preparation).

[83] *The DØ Upgrade. The Detector and Its Physics*, Fermilab Pub 96/357-E.

[84] A. Kupco, *Measurement and QCD analysis of inclusive dijet mass cross section in $p\bar{p}$ collisions at $\sqrt{s}$ = 1.96 TeV*, PhD thesis, Charles University, 2003, (Unpublished).

[85] G. Davis, *First Measurement of the Differential Inclusive Cross Section for Jet Production at DØ RunII*, PhD thesis, University of Rochester, 2004, (Unpublished).

[86] *DØ Silicon Tracker Technical Design Report*, DØ Note 2169.

[87] http://d0server1.fnal.gov/users/qianj/CPS/doc/dn3104.pdf.

[88] DØ, B. Abbott *et al.*, Nucl. Instrum. Meth. **A424**, 352 (1999), hep-ex/9805009.

[89] Heidi Schellman for the NuTeV Collaboration, private communication.

[90] http://www-e815.fnal.gov/NuTeV.html.

[91] A. Brandt *et al.*, 1997, Fermilab Pub 97/377.

[92] http://www.omega.com/literature/transactions/volume3/high3.html.

[93] http://www.rdpe.com/displacement/lvdt/lvdt-principles.htm.

[94] A. Frank *et al.*, *The DØ Rack Monitor Module*, 1990, DØ Note 1051.

[95] http://adwww.fnal.gov/controls/networks/vaxnetusr.txt.

[96] J. E. Huth *et al.*, Presented at Summer Study on High Energy Physics, Research Directions for the Decade, Snowmass, CO, Jun 25 - Jul 13, 1990.

[97] S. D. Ellis, Z. Kunszt, and D. E. Soper, Phys. Rev. Lett. **69**, 3615 (1992), hep-ph/9208249.

[98] S. Catani, Y. L. Dokshitzer, and B. R. Webber, Phys. Lett. **B285**, 291 (1992).

[99] S. Catani, Y. L. Dokshitzer, M. H. Seymour, and B. R. Webber, Nucl. Phys. **B406**, 187 (1993).

[100] S. D. Ellis and D. E. Soper, Phys. Rev. **D48**, 3160 (1993), hep-ph/9305266.

[101] G. C. Blazey *et al.*, (2000), hep-ex/0005012.

[102] S. Catani *et al.*, (2000), hep-ph/0005114.

[103] W. Giele *et al.*, (2002), hep-ph/0204316.

[104] J. Vlimant, U. Bassler, G. Bernardi, and S. Trincaz-Duvoi, *Technical description of the T42 algorithm for the calorimeter noise suppression*, 2003, DØ Note 4146.

[105] G. Bernardi, E. Busato, and J. Vlimant, *Improvements from the T42 Algorithm on Calorimeter Objects Reconstruction*, 2004, DØ Note 4335.

[106] G. Bernardi, B. Olivier, B. Knuteson, and M. Strovink, *NADA: A New Event by Event Hot Cell Killer*, 1999, DØ Note 3687.

[107] G. Bernardi and S. Trincaz-Duvoid, *Improvement of the NADA Algorithm: Hot Cell Killing in DØ Run II Data*, 2002, DØ Note 4057.

[108] J. Agram *et al.*, *Jet Energy Scale at DØ Run II*, 2005, DØ Note 4720.

[109] J. Barreto and A. Drozhdin, *Reconstructing Track Trajectories for the FPD*, 2000, DØ Note 3788.

[110] G. A. Alves *et al.*, *Forward Proton ID Certification I: Elastic Process and and Standalone DAQ*, 2002, DØ Note 4054.

[111] D. Goulianos, *Diffraction in CDF: Run I results and plans for Run II*, http://dis2001.bo.infn.it/wg/overhead/D/k-goulianos.ps.gz.

[112] H. Nakada, *Kinematic Study of Diffractive Dijet Events at 1.8 TeV*, 1998, CDF Note 4403.

[113] http://d0server1.fnal.gov/projects/FPD/web/fpd/documents/run_checklist.html.

BIOGRAPHICAL STATEMENT

Michael Allen Strang was born in Salt Lake City, Utah in 1971. He received his B.Sc. degrees in Physics and Mathematics from the University of Utah in 1994 and 1996 respectively and his M.Sc. in Physics from the University of Texas at Arlington in 2000.